The Republic of Iraq
Ministry of Higher Education and Scientific Research
University of Misan
College of Basic Education

Biosensor Detection Based on Photonic Crystal Fiber and Surface Plasmon Resonance

A Thesis

Submitted to the Council of the College of Basic Education, University of Misan, In partial fulfillment of the Requirements for the Degree of Master in General Sciences (Specialized General Sciences)

By:

Ruqayyah Raad Awald

Supervisor by :

Prof.Dr. Younis Mohamed Atiah Al-Zahy

2025 **A.H.** 1447 **A.D.**

﴿يَرْفَعِ اللَّهُ الَّذِينَ آمَنُوا مِنْكُمْ وَالَّذِينَ أُوتُوا الْعِلْمَ دَرَجَاتٍ وَاللَّهُ بِمَا تَعْمَلُونَ خَبِيرٌ﴾

صدق الله العلي العظيم

سورة المجادلة: الآية ١١ .

الإهداء

إلى خالق الكون . . إلى الذي نستعين به ونتوكل عليه

إلى من بيده كل شي . . إلى ربي وخالقي

إلى سيد الكائنات . . . محمد صلى الله عليه وآله الطيبين الطاهرين

عليهم افضل الصلاة والسلام

إلى والدي العزيز . . . رحمه الله

إلى والدتي . . . أطال الله في عمرها

الى اخوتي واخواتي ....حبا واعتزازا

إلى أصحاب الفضل الدائم . . . أساتذتي الكرام

إلى بلدي العزيز . . . العراق العظيم مدينتي الغالية . . . حفظها الله ميسان

الشكر والتقدير

الحمد لله والشكر على فضله وعلى توفيقه لنا في إنجاز هذه الرسالة كما نتقدم

بخالص الشكر والامتنان إلى الأستاذ المشرف ((ا.د. يونس محمد عطية))

والآنسة (زينب صباح بدن) على كل ما قدموه من نصائح وتوجيهات حرصاً

منهم على انجاز هذا الرسالة وتقديمها بالصورة المطلوبة

كما أتقدم بالشكر الى رئاسة قسم العلوم ولجميع أساتذتي الكرام وجميع كادر القسم

الذين كانوا معي على مدار سنوات الدراسة

Table of Contents

List of Figures

List of Tables

List of Abbreviations

Table	Full Term
AIDS	Acquired Immunodeficiency Syndrome
CFU	Forming Unit-Colony
CL	Confinement Loss
DL	Detection Limit
FEM	Finite Element Method
FOM	Figure of Merit
FWHM	Full Width at Half Maximum
HIV	Human Immunodeficiency Virus
LSPR	urface Plasmon ResonanceLocalized S
NIR	Infrared-Near
OSA	Optical Spectrum Analyzer

PBG	Photonic Band Gap
PCF	Photonic Crystal Fiber
PDE	Partial Differential Equation
PML	Perfectly Matched Layer
RI	Refractive Index
RIU	Refractive Index Unit
S_A	itivityAmplitude Sens
SMF	Single Mode Fiber
SNR	Noise Ratio-to-Signal
SPP	Surface Plasmon Polariton
SPR	Surface Plasmon Resonance
S_λ	Wavelength Sensitivity
TE	Transverse Electric
TIN	Titanium Nitride
TM	Transverse Magnetic
TO	Transformation Optics

Abstract

This thesis presents design of a biosensor based on a surface plasmon resonance (SPR) photonic crystal fiber (PCF) for sensitive detection. light is confine in a single mode within the core by a lattice of air holes, the fiber is covered by circular gold film. The performance of the sensor evaluated using numerical simulations by COMSOL 6.3. The proposed design was enhanced by optimizing measurements such as air hole diameter (d), lattice pitch (Λ), and gold layer thickness (tg) to increase the confine loss of light. The optimized device proved good ampltude sensitivity(S_λ) around a spectrum of biological analytes: 7,333 Mm/RIU for HeLa (cervical cancer), 5,500 nm/RIU for Jurkat (T lymphocyte cancer), 5,000 nm/RIU for PC12 (adrenal tumor), 6,250 nm/RIU for the HIV virus, 8,571 nm/RIU for MDA-MB-231 (breast cancer), 7,692 nm/RIU for MCF-7 (breast cancer), 3,857 nm/RIU (HIV infection) and 4,000 nm/RIU for Glucose solution. Subsequently, this PCF-SPR presents a hopeful and cost-efficient alternative to conventional diagnostic techniques such as surgical biopsy, medical imaging, and chemical assays, with the ability to easier disease detection.

Chapter one

Introduction

1-Introduction:

Surface Plasmon Resonance (SPR) biosensing is one of the influential methods for detecting biomolecular interactions. Essentially, this technique is built upon an attractive phenomenon: stimulating surface plasmons, which are basically collective oscillations of electrons, at the surface of a very metal layer, typically gold or silver, gold deposited on a dielectric substrate silicon dioxide. The incident light interacts with this electron at the resonance condition, Changes in the refractive index (RI) adjacent to the metal surface have a significant impact on this resonance condition [1]. The resonance condition is influenced by a measurable shift in the index due to molecule binding events, which leads to highly sensitive detection [2]. For clinicians, the influence of this technology lies in its sensitivity. It allows the detection of crucial disease markers at minute levels; it's this sensitivity to refractive index shifts making it a cornerstone in diverse medical areas from diagnostic analysis and pathogen discovering to the critical search for biomarkers that can guide treatments [3-5]. SPR's remarkable optical properties have led to wide-ranging applications beyond medicine in fields like biochemistry, optoelectronics, and nanophotonics.

The SPR sensor's performance depends on the choice of plasmonic metal. Silver, aluminum, and copper are metals that can support surface plasmons, but their practical application is often hindered by rapid oxidation in aqueous environments, which can lead to performance degradation [4-8]. Despite the ability of graphene or titanium dioxide coatings to passivate these metals, they can still complicate and cost the fabrication process [6-10]. Gold has become the most important material in the field due to its exceptional chemical inertness and stability, ensuring consistent performance even though it has a slightly lower resonance Sharpness compared to silver [8-11].

Thin layers of gold or silver are often deposited onto optical surfaces for SPR implementations fibers [12]. The effectiveness of the surface is determined by the thickness of the metal layer, the propagation of Plasmon waves at dielectric-metal interfaces has a significant effect on it. performance of these sensors, when a light undergoes complete internal reflection with the material, these waves are excited [12]. Recent investigations into surface plasmon resonance (SPR) sensors utilizing photonic crystal fibers (PCFs) have concentrated on enhancing sensitivity and expanding the detection range. For instance, a D-shaped PCF configuration achieved an impressive sensitivity of 22,400 nm/RIU for analytes with a low refractive index (1.27–1.37) [13].

Furthermore, a hybrid sensor that combines both intrinsic and extrinsic techniques showed a scalability that was wide (RI: 1.33–1.40) [14], with reported sensitivity levels of 10,000 and 12,000 nm/RIU, respectively. Many studies have been concentrated on particular ranges of refractive indices with designs. A two-channel open-loop photonic crystal fiber (PCF) sensor achieved a sensitivity of 11,055 nm/RIU [15], whereas another design functioning in the mid-infrared reported a sensitivity of 11,000 nm/RIU [16]. Within the biological buffer range (RI: 1.33–1.39), various geometric configurations have shown effectiveness: concave sensors reached a sensitivity of 9,314 nm/RIU [17], while D-shaped configurations attained a sensitivity of 8,920 nm/RIU [18], moreover, designs have been employing square lattices [19] and multi-cavity structures [20] have been exhibited exceptional sensitivities exceeding 140,000 nm/RIU, thus pushing the boundaries of performance across broader refractive index ranges.

In recent years, fiber-optic sensing (FOS) has concerned major interest for biosensing applications, primarily determined by its promise of high sensitivity,

fast detection times, and non-destructive testing [21]. A standout type within this field is plasmonic fiber optic sensors. These devices not only capture the core strengths of FOS but also combine the remarkable sensitivity of plasmonics and incorporated multiplexing, achieving this without the need for complex and expensive add-ons. Consequently, biosensors that employ Surface Plasmon Resonance (SPR) on a fiber-optic platform are seen as especially attractive, demonstrating significant commercial promise for use in chemistry and the life sciences [22, 23].

1-1 Literature Review

To explain the evolution of the Photonic Crystal Fiber (PCF) biosensors in terms of how the technology has evolved, this review provides a summary of the development of the biosensors with the year of research simplified and structured to explain how the technology has evolved.

Akowuah et al. (2012) gave a critical theoretical basis of multi-analyte detection. Their suggested PCF structure was probably to have several sensing channels or one channel with the ability to support several resonant channels. They showed (via intense numerical simulations (usually with the Finite Element Method)) that various resonant peaks in the transmission spectrum could independently and simultaneously respond to a change in the refractive index of two different analytes in separate channels or be bound to two different biomolecules[24].

Wong et al. (2013) succeeded in bridging the gap between a generic refractive index sensor and a real biosensor. In this case they employed a PCF that had thin coating of gold film (the plasmonic material) on a substrate and then functionalized the gold surface with a special protein, which is most likely a special antibody or

detector protein. It is such a functionalization layer that makes the sensor specific. A localized increase in the refractive index at the gold surface is produced when the target analyte (e.g., a complementary antibody or antigen) of a solution binds to this receptor protein. Such variation is observed as a change in SPR resonance condition. Their research showed that PCF-SPR platforms could be adapted to highly selective biological sensing, the requirement to apply PCF-SPR in clinical and research settings, by proving that such platforms could detect these particular molecular interactions with high accuracy[25].

Sharma and Sharan (2014) oriented their sensor design to a more direct and realistic medical use, namely non-invasive glucose monitoring in urine. The sensor is designed and optimized to work in the distinct range of the refractive index of physiologically important glucose levels in urine. This was a milestone as a general-purpose sensor was no longer used but rather an application-specific device was used. It reflected a directional trend towards the practical diagnostics of the medical world using the PCF-SPR technology, as it is no longer the laboratory parlor curiosity, a device with a prospect of controlling a disease such as diabetes [26].

Rifat et al. (2016) proposed a D-shaped PCF design was suggested by Rifat et al., where the fiber was flattened on one of the sides, and directly put on this flat outer surface it was deposited with gold. The analyte was then merely applied on the surface of the fiber. This external sensing or open-loop system made the sensor operation extremely simple, reusable and greatly reduced the fabrication process. This philosophy of design has been extended to various studies since its inception because it possesses feasible merits. The critical parameter optimization was considered [27].

In 2017 by Hasan et al. The thickness of the layer of metal (in this case, gold) is a major parameter that determines the coupling efficiency between the light propagated in the fiber and the surface plasmids in an SPR sensor. In case the layer is excessively thin, the plasmonic field is weak; in case it is excessively thick, the light cannot couple through the layer effectively. The effect of gold layer thickness on sensitivity was modeled and analyzed in detail by Hasan et al. They could produce a high level of sensitivity of 2,200 nm/RIU [28].

In 2018, Chakma et al. reporting the design (hexagonal lattice PCF with a large central air hole) and numerical analysis of a highly sensitive surface plasmon resonance (SPR) biosensor based on a simple photonic crystal fiber (PCF) structure, authors reported a maximum sensitivity of 9000 nm/RIU for an analyte refractive index (RI) range of 1.33 to 1.37 [29].

In 2019, Hossain et al. developed a biosensor to track the level of glucose in the blood. The sensor design was a hexagonal lattice PCF that had a gold coating layer on the outer surface in the shape of the D. These findings showed that the sensor proposed in the study had a high wavelength sensitivity of 4000 nm/RIU within the biological range of refractive index at which glucose can be detected (1.33 to 1.39) [30].

Arunya Revathi and Rajeswari (2020) have designed and numerically analyzed a dual-core Photonic Crystal Fiber (PCF) sensor optimized to be used as a chemical sensor. The sensor structure proposed had a two-core structure, which was achieved by not allowing air holes in the pattern of a hexagonal lattice, the outermost coating of the fiber was covered with a thin gold film to produce Surface Plasmon Resonance (SPR). They declared that they could detect the analytes with

the refractive indices between 1.33 and 1.37 with a maximum sensitivity of 10,000 nm/RIU [31].

In 2021, Esfahani Monfared and Qasymeh proposed a novel, label-free biosensor, which is a graphene-coated photonic crystal fiber (PCF) that is designed to detect the components of blood. The sensor proposed was made in the shape of D with the flat surface covered by the silver layer, covered by a graphene layer. They found that the sensitivity of this hybrid material structure was high with a wavelength sensitivity of up to 5000 nm/RIU to detect plasma and red blood cells with a refractive index range of 1.35 to 1.40 [32].

Rahman, Rana, and Anower (2022) paid attention to the creation of a Photonic Crystal Fiber (PCF) biosensor that is straightforward and inexpensive. The design proposed made use of a hexagonal lattice design using a single and selectively gold-coated microchannel, their findings showed that their relatively simple design could be used to achieve a high wavelength sensitivity of 6000 nm/RIU over a range of refractive index of 1.32 to 1.37 [33].

In 2023, Fakhri et al. proposed a photonic crystal fiber (PCF) sensor with a particular medical goal the early diagnosis of cancer. A square-lattice PCF structure was used to design the sensor. Its main innovation was the inclusion of gold nanoparticles (AuNPs) in the channels of the fiber, that is, they were able to detect the cancer cells with a maximum sensitivity of 5500 nm/RIU and a high amplitude sensitivity of 480 RIU^{-1} [34].

The sensor design discussed **in 2024 by Chaity** had a hexagonal lattice design with a layer of gold placed on the outer to support surface plasmon resonance (SPR). The size and pitch of the air holes were made optimal and were designed in such a way that they maximized the performance. The sensor had a sensitivity of

24, 285 nm/RIU with Breast Cancer Type 2, with high sensitivities in other cancers, such as Skin Cancer (20,000 nm/RIU) and Blood Cancer (17,000 nm/RIU) [35].

In 2025, Rizk, El-Gohary, presented a new design of sensors with a special cavity, which had an ovoidal (egg-like) shape and was located inside the center of the fiber core and was covered with a stack of silver-graphene that excited surface plasmon resonance (SPR) to detect cancer cells.They found that the unique ovoidal (egg-shaped) cavity design was able to detect all types of cancer cells with a high wavelength sensitivity of up to 6000 nm/RIU [36].

In 2025, Hasanein, El-Gohary, and Obayya presented the sensor design featured a dual-core PCF structure, The sensing mechanism utilized a gold film to generate surface plasmon resonance (SPR). Using the Finite Element Method (FEM) for numerical analysis, the researchers demonstrated that their design could achieve ultra-high sensitivity for both hormones concurrently. They reported a maximum wavelength sensitivity of 12,400 nm/RIU for progesterone and 11,800 nm/RIU for estradiol within a physiologically relevant refractive index range [37].

In 2025, Gupta, Kumar, and Srivastava considered the use of photonic crystal fiber (PCF) sensors in other areas than the biomedical one, the paper proposed and analyzed numerically a simple metal-coated PCF sensor that would detect different chemicals and gases used during industrial processes in real-time. Their findings indicated that the sensor recorded a high sensitivity of the wavelength of up to 8,500 nm/RIU [38].

Shukla, Kumar, and Tripathi (2025) have performed a comparative analysis of performance of two dissimilar plasmonic materials in Surface Plasmon Resonance Photonic crystal Fiber (SPR-PCF) based biosensors to detect cancer cells. Two

different sensor designs were proposed and numerically assessed in the study: one with a traditional silver coating and the other with a coating of tin-based. Their findings showed that although the silver-coated sensor had high sensitivity of 8,200 nm/RIU[39].

1-2 Photonic crystal fibers

The advent of step-index fiber made significant changes by increasing the speed and ease of communication in our life [40]. Since then, various PCF structures have been demonstrated and investigated in different fields of research [41]. Fibers with an internal periodic structure made of capillaries occupied by air are the Photonic crystal fibers (PCFs). The defects in fibers crystal structure gives light a clear passage to propagate through. A number of unique features that are impossible to get in the regular fibers can be obtained from the new type of optical fibers PCFs by mixing the properties of optical fibers and photonic crystals [42]. The Internal structure of a PCF is illustrated in the Fig. (1.1).

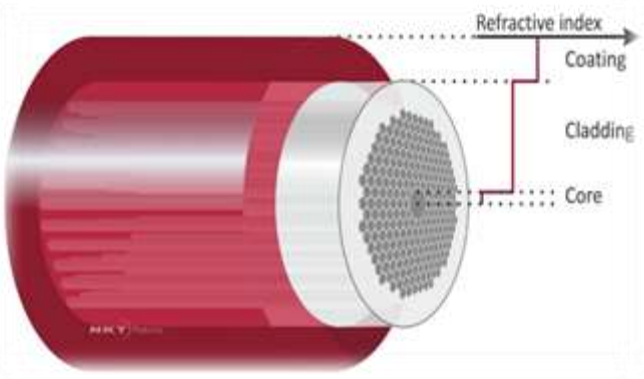

Figure (1.1): Internal structure of photonic crystal fiber[42].

The waveguide is capable of confining electromagnetic waves in two literal dimensions, and on the other hand allowing the wave to propagate in an axial direction [43]. A typical feature of all index-guiding PCFs is the core comprised of solid silica and surrounded by micro structured cladding. The efficacy index

refractive of the cladding is lower than the core due to the occurrence of air-holes and light is being directed on the basis of the property of total internal reflection. PCF can be fabricated with fusing silica or undoped silica (SiO_2) and the active devices can be fabricated by adding dopants in a similar fashion as the conventional fiber. Multi Materials have been filled either a single air hole or a number of air holes at various points. This results in interesting plasmonic behavior of so-called plasmonic PCF.

1.2.1 Types of Photonic crystal fibers

Photonic crystal fibers are classified into three main categories: one-dimensional, two-dimensional and three-dimensional photonic crystal fibers.

1.2.1.1 One-Dimensional (1D) PCF

In 1DPCFs, the periodic modulation of the refractive index occurs in one direction only, while the refractive index variations are uniform for other two directions of the structure. A case of one-dimensional photonic crystal fiber application is the Bragg mirror, which is usually used in dielectric mirrors and optical switch, etc. [44]. The PBG appears in the direction of periodicity for any value of refractive index contrast i.e., difference between the dielectric constant of the materials. In other words, there is no threshold for dielectric contrast for the appearance of a PBG. For smaller values of index contrast, the width of the PBG appears very small and vice versa. However, the PBGs open up as soon as the refractive index contrast is greater than one ($n_1 / n_2 > 1$), where n_1 and n_2 are the refractive index of the dielectric materials. A defect can be introduced in a 1DPCs, by making one of the layers to have a slightly different refractive index or width than the rest. The defect mode is then localized in one direction however it is extended into other two directions. An example for such a 1DPCF is the well-

known dielectric Bragg mirror consisting of alternating layers with low and high refractive indices, as shown in Figure (1.2) [45].

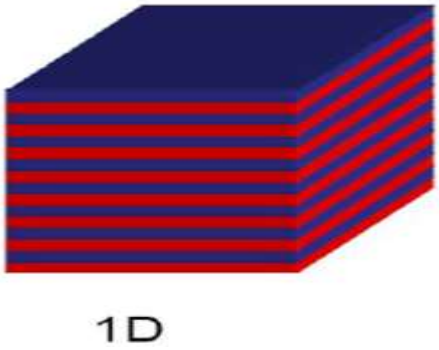

Figure (1.2): Example of 1D PCF [45]

1.2.1.2 Two-Dimensional (2D) PCF

Structure(s) that are periodic in two different directions and homogeneous in third direction are called 2DPCF, which is shown in Figure (1.3a). In most of the 2DPCFs, the PBG occurs when the lattice has sufficiently larger index contrast. If the refractive index contrast between the cylinders (rods) and the background (air) is sufficiently large, 2D PBG can occur for propagation in the plane of periodicity perpendicular to the rod axis. Generally, 2DPCFs consist of dielectric rods in air host (high dielectric pillars embedded in a low dielectric medium) or air holes in a dielectric region (low dielectric rods in a connected higher dielectric lattice) as shown in Figures (1.3b). PBG is provided by the dielectric rods in air host on the Transverse Magnetic (TM) mode wherein E field is polarized perpendicular to the plane of periodicity. In one plane of periodicity, the air holes of a dielectric region provide (Transverse Electric) TE mode in which H field is polarized perpendicular to the plane of periodicity [46].

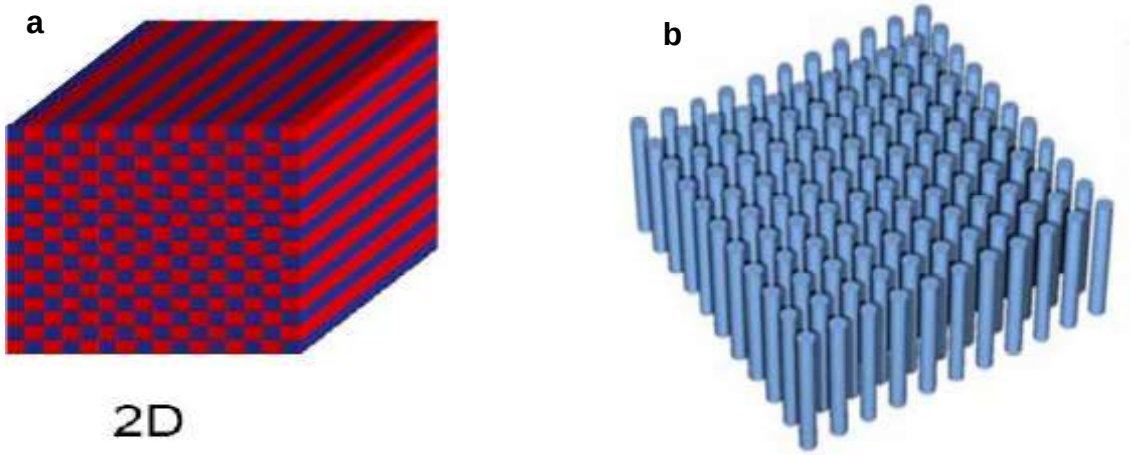

Figure (1.3): Example of 2D PCF[46]

1.2.1.3 Three-Dimensional (3D) PCF

A 3D PCF is a dielectric structure which has periodic permittivity modulation along three different axes, provided that the conditions of sufficiently high dielectric contrast and suitable periodicity are met, a PBG appears in all directions which is shown in Figure (1.4a) and (1.4b). Such 3D PBGs, unlike the 1D and 2D ones, can reflect light incident from any direction. In other words, a 3D PBG material behaves as an omnidirectional high reflector. Due to the challenges involved in fabricating high-quality structures for the scale of optical wavelengths, early PCs are performed at microwave and mid-infrared frequencies [47, 48]. With the improvement of fabrication and materials processing methods, smaller structures have become feasible, and in 1999 the first 3DPC with a PBG at telecommunications frequencies is reported [49, 50]. Since then, various lattice geometries have been reported for operation at similar frequencies [51].

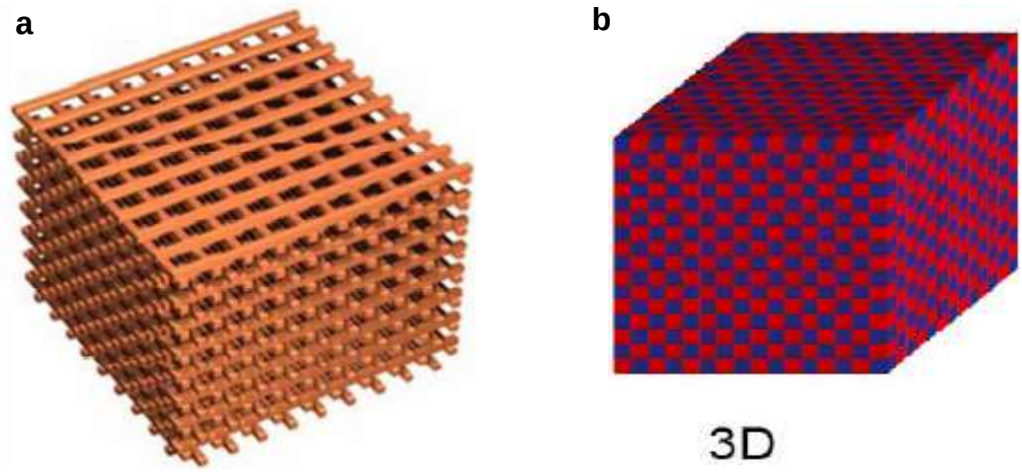

Figure (1.4): Example of 3D PCF [51]

1-3 Applications of the photonic crystal fiber

This section describes numerous approaches for improving SP RI biosensors in biosensing applications. In recent years, SP-based sensors have stood out from these devices because they can detect minor changes in the refractive index (RI) of the sensing material in an environment. They have also received a lot of attention in biosensing applications because various biomaterials, liquid analytes, and gases (i.e., different cancerous cells, blood components) have specific RI values.

1.3.1 Photonic-crystal fibers sensor D-shaped

The sensor is shown in Figure (1.5) where the analyte is placed in the center core of the fiber and is surrounded by air holes in the backdrop of Silica under the SP resonant conditions. PCF D-shaped that has been coated with Titanium Nitride (TiN) in place of the conventional gold and silver metallic layers. This can be attributed to a high melting point, chemical stability and conductivity of TiN. This

sensor had a maximum spectral sensitivity of -16275 nm/RIU numerically, an amplitude sensitivity of 206.25 RIU^{-1}, and a maximum FOM of 147.9 RIU^{-1}, and operated in the RI range of 1.44-1.52 [52].

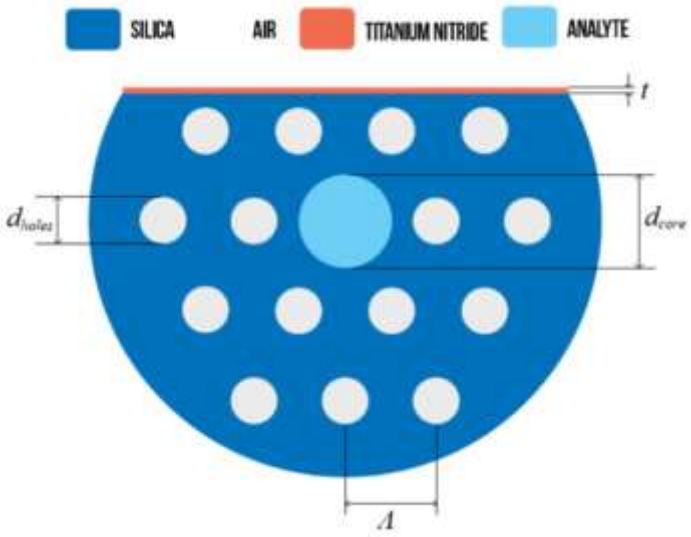

Figure (1.5) PCF D-shaped for the detection of cancer cells [52]

1.3.2 Single mode fiber sensor with 7 cores

The sensor is shown in Figure (1.6) where design consists of single mode fiber (SMF) that is spliced with seven cores of MCF that are hexagonally arranged as illustrated in Fig. **1.6**. In the design, LSPR excitation was done using gold and MoS2 NPs and these were also used to enhance the performance of the sensor. The sensor was created and experimented to identify germs in a liquid. These findings indicate that the sensor was able to detect the presence of Shigella bacteria in linear proportions 1:109 Colony-Forming Unit/mL (CFU/mL) in the 5 minutes with a detection limit of 1.56 CFU/mL [53].

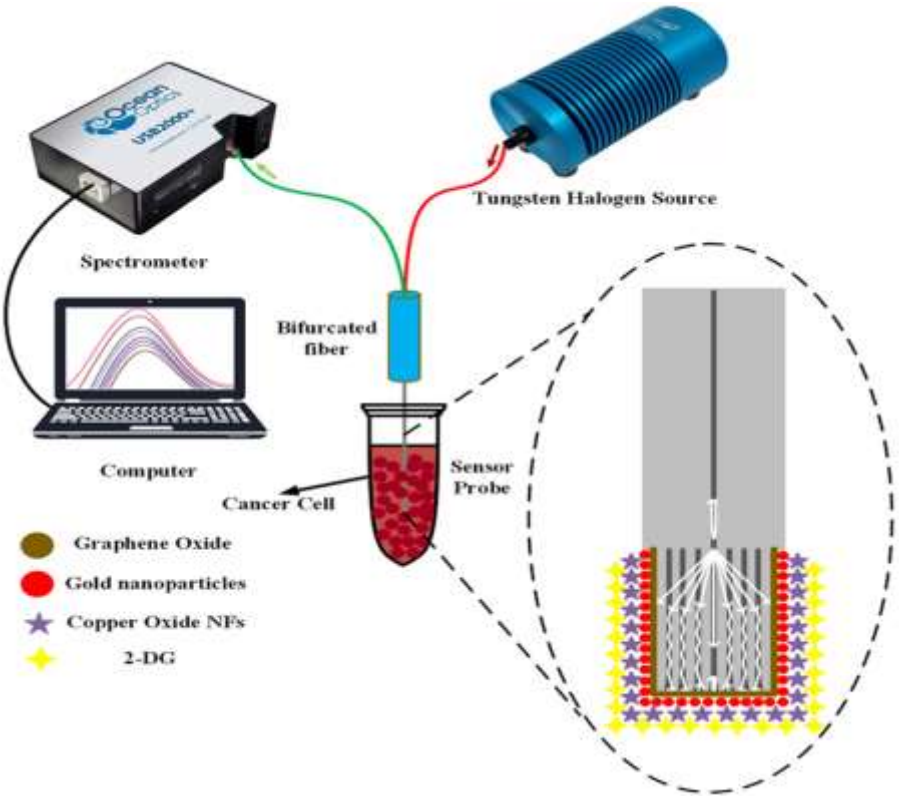

Figure (1.6) single mode fiber (SMF) for the detection of Shigella bacteria[53].

1.3.3 Single mode fiber sensor with 1 core

Figure (1.7) illustrate optical fibers used as SP RI sensors. The biological specimen is detected by using the optical fiber's evanescent waves, which are then exposed to the metal-dielectric contact to stimulate SPP. This is achieved by replacing a section of the cladding material with a metallic layer or metallic nanostructure. The sensing material layer is often the dielectric layer that comes after the metal layer [54].

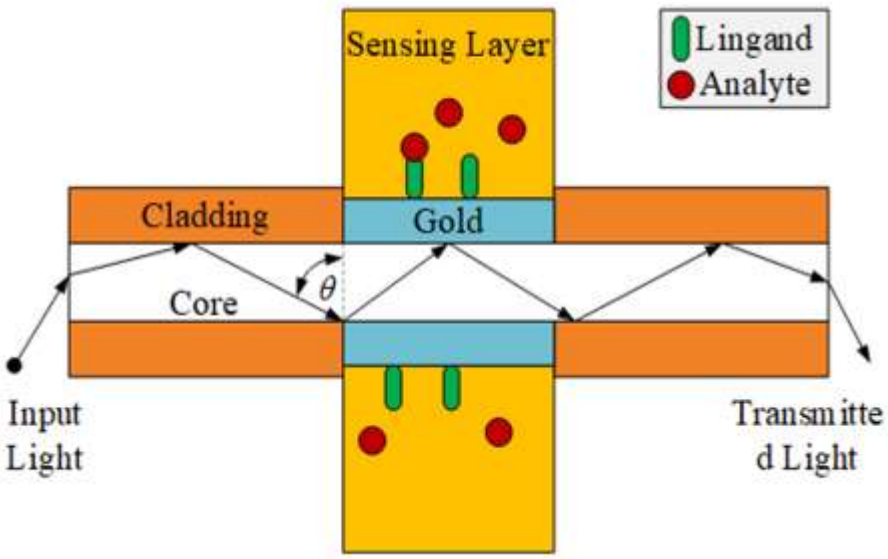

Figure (1.7) optical fiber for the detection of biological specimen[54]

1.3.4 Optical fiber sensor U shape

Figure (1.8) employe U shape with MoS_2 and gold film in order to detect human IgG protein, a modified optical fiber biosensor. To prepare the sensor, the coatings of the fiber were taken off to reveal the core after which they were bent into a U shape. The authors tested the performance of two versions, that is, fiber-MoS2-Gold film and fiber-gold film MoS_2. The sensitivity of the former sensor setup (6184.4 nm/RIU) was found to be 25% higher than the latter (6184.4 nm/RIU) with a DL of 19.7 ng/mL when the assay was used to detect human IgG. To begin with, experimental apparatus was employed in the production and identification of the alcohol solutions with different refractive indices of 1.3314, 1.3423, 1.3537, 1.3593, and 1.3623. After the preparation and testing of a human IgG solution [55].

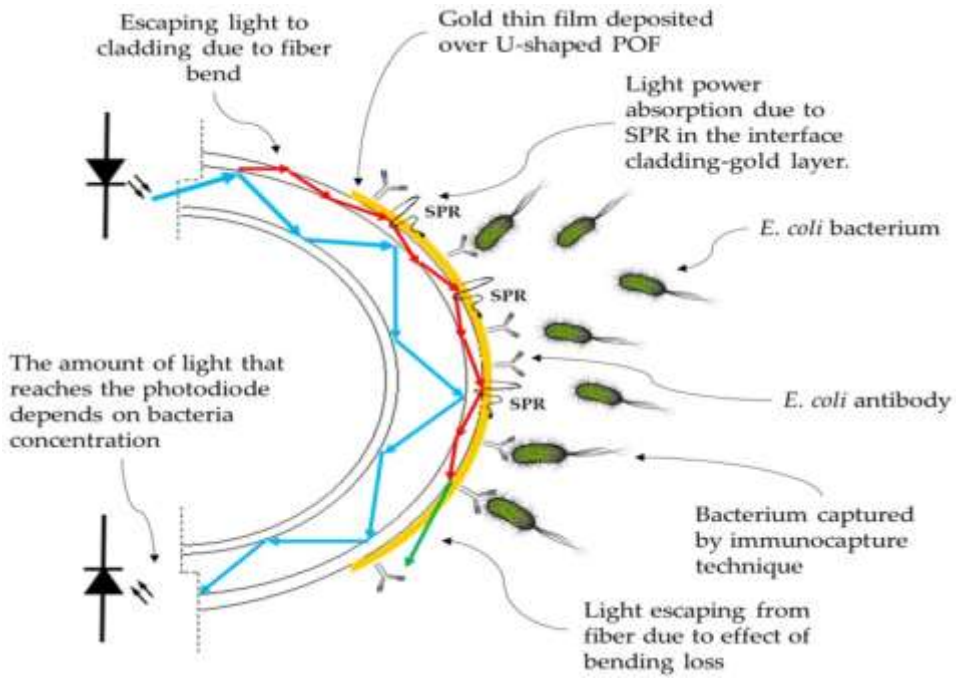

Figure (1.8) U shape with MoS_2 and gold film for the detection of IgG protein [55]

1.3.5. A prism photonic sensor

A simple biosensor is composed of a prism with a thin coating of gold film as shown in Fig. (1.9). It works on the principle of the prism-coupled attenuated total reflection technique that drives a surface plasmon resonance (SPR) by coupling a field of electromagnetic radiation to surface plasmon waves. The sensor is able to reach a range of sensitivity of 2056-5893 nm/RIU which is similar to other wavelength-modulated SPR sensors [56].

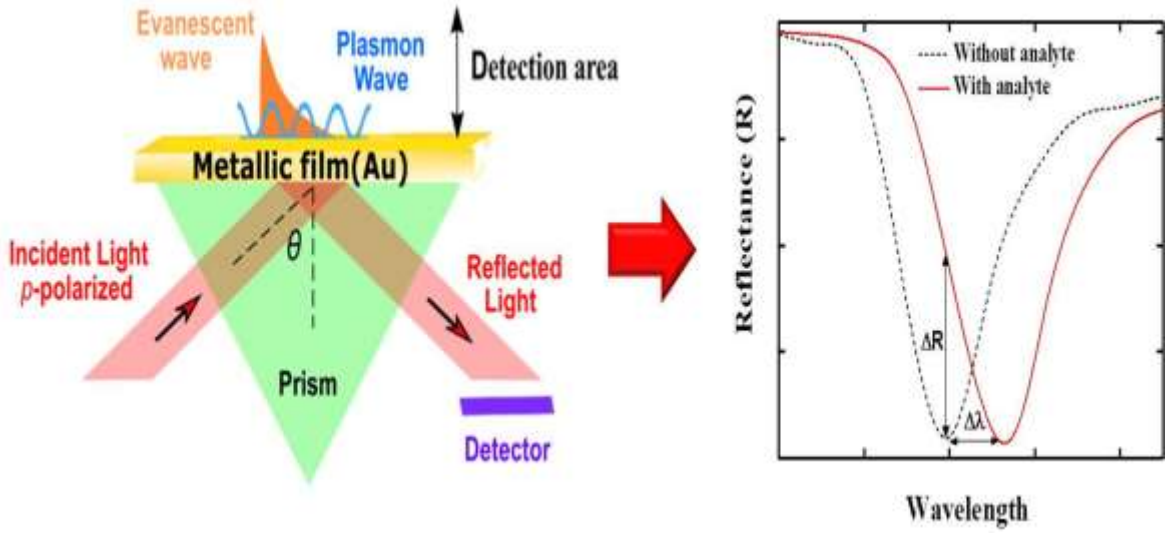

Figure (1.9) biosensor is composed of a prism and gold film[56]

1.3.6. A grating photonic sensor

Figure **(1.10)** shows a 1-D barium flint glass grating pattern on a thin layer of gold on a silicon nitride substrate is used in the design of the sensor. Because of the connection between the incident plane wave and the surface plasmon wave, this design's reflection spectrum shows a strong, narrow rejection band at normal incidence. the design used to detect blood glucose based on the influence of change refractive index, the sensor achieved a sensitivity of ~2600 nm/RIU and a quality factor of ~1500 [57].

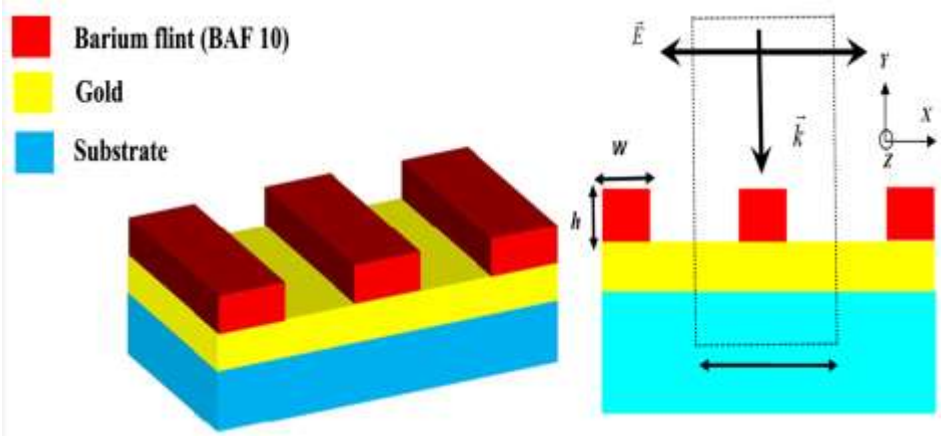

Figure (1.10): PCF sensors with glass grating [57]

1.4 Types of Samples

1.4.1. Breast cancer (MDA-MB-231)

Breast cancer is a condition in which a number of cells in the breast start to proliferate in an unexpected and unregulated manner. These cells may develop into a tumor or lump. Although both genders are susceptible to it, it is prevalent among women. The positive aspect is that, there are a lot of breast cancers which can be treated successfully, particularly when it is detected at an early stage through such means as self-exams or mammogram (a special type of x-ray). The methods of treatment may involve surgery, radiation or medication. It is quite significant to know the symptoms and consult a physician concerning screening.

MDA-MB-231 is the name of an exceptionally significant cell line of human breast cancer that scientists use. These were cells derived out of the tumor of a patient and can be allowed to grow indefinitely in a laboratory as shown in Fig. (1.11). They are said to be extremely aggressive and the ability to spread and they are the main device used to study a form of breast cancer that is hard to cure. Due to the unresponsiveness of such cancer to typical hormone treatment, scientists rely on MDA-MB-231 cells to test novel medicines and learn how cancer cells invade other systems of the body. To put it in brief, they are a critical model of seeking superior treatment of aggressive breast cancer [58].

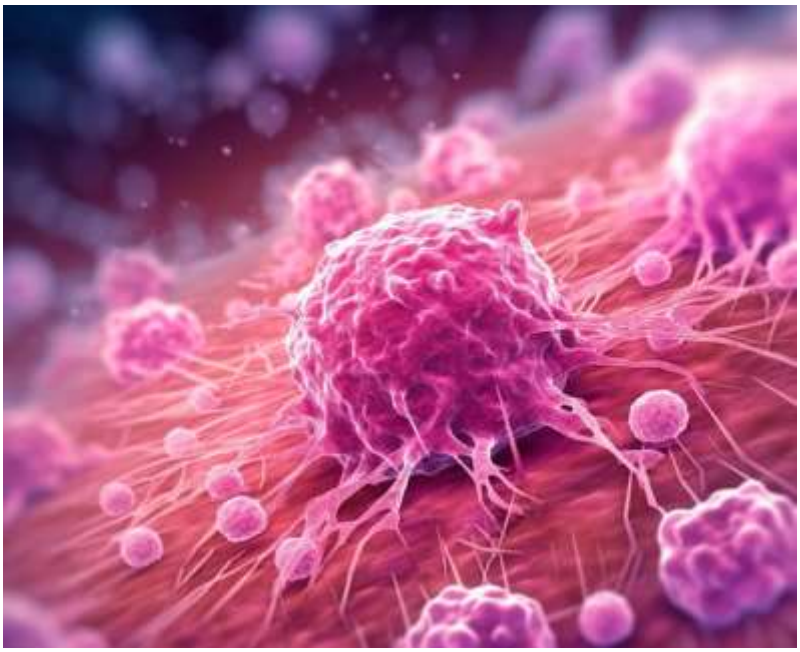

Figure (1.11): Breast cancer cell[58]

1.4.2 Blood cancer (JURKAT cells)

Blood cancer is an illness, which begins in your blood or bone marrow cells, which is the spongy inner of your bones where blood is produced. In normal body, the blood cells multiply and perish in a moderated manner. However, in the case of blood cancer this process is interfered with. The body produces massive numbers of defective blood cells which are not functional as shown in Fig. (1.12). These unhealthy cells fill space occupied by the healthy blood cells and the body struggles to fight off infections, supply oxygen to the body and stop bleeding. Blood cancer is of various types such as leukemia and lymphoma. The therapies are meant to kill the cancerous cells and may involve chemotherapy, radiations or a transplant of the stem cells.

JURKAT cells are a well-known and significant device used by the scientists. These are a series of human blood cells that were cloned off a leukemia patient. Such cells are immortal i.e. they can develop and multiply in an artificial laboratory indefinitely. The JURKAT cells are used in the world by scientists who

study the immune system and test new medications on cancer, as well as learn how illnesses behave [59].

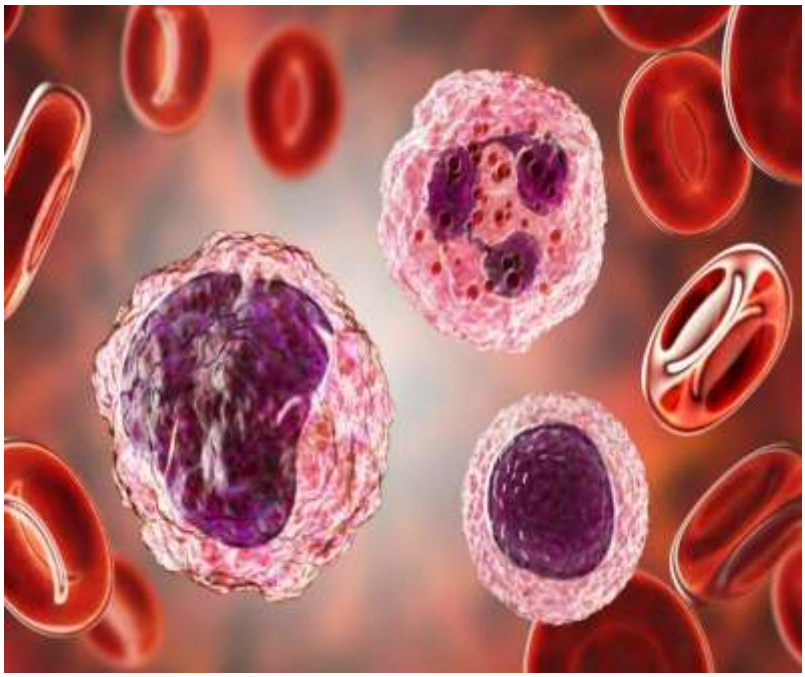

Figure (1.12): Blood cancer cell[59]

1.4.3 Adrenal glands (PC12)

Adrenal glands are a pair of small glands, which are located on the top of the kidneys. They are meant to produce significant hormones that aid your body to cope with stress, high blood pressure, and salt levels. Adrenal cancer is extremely rare and, in this case, the cells within one of these glands begin to grow out of control and create a tumor as shown in Fig. (1.13). In some cases, this tumor may lead to the gland producing an excess of hormones that may have such symptoms as high blood pressure, weight gain, or feeling very weak. It is so rare that this will make doctors carry out a number of tests in order to diagnose it. Surgery may be done to extract tumor and, in some cases, additional treatment is required.

PC12 is a cell line that is widely applied in the laboratory research by scientists. These cells were initially cloned out of a tumor of the adrenal gland of a rat. The greatest aspect of PC12 cells is that under the appropriate conditions, they can behave like nerve cells (neurons). PC12 cells cease to divide and extend into long and branching extensions when scientists place in them a particular growth factor, the manner in which neurons grow. Due to this fact, they are highly convenient and more easily studied model of the processes of growth of nerve cells, their communication and survival. PC12 cells have been of particular use in the study of the nervous system such as in Parkinson disease and nerve regeneration studies [60].

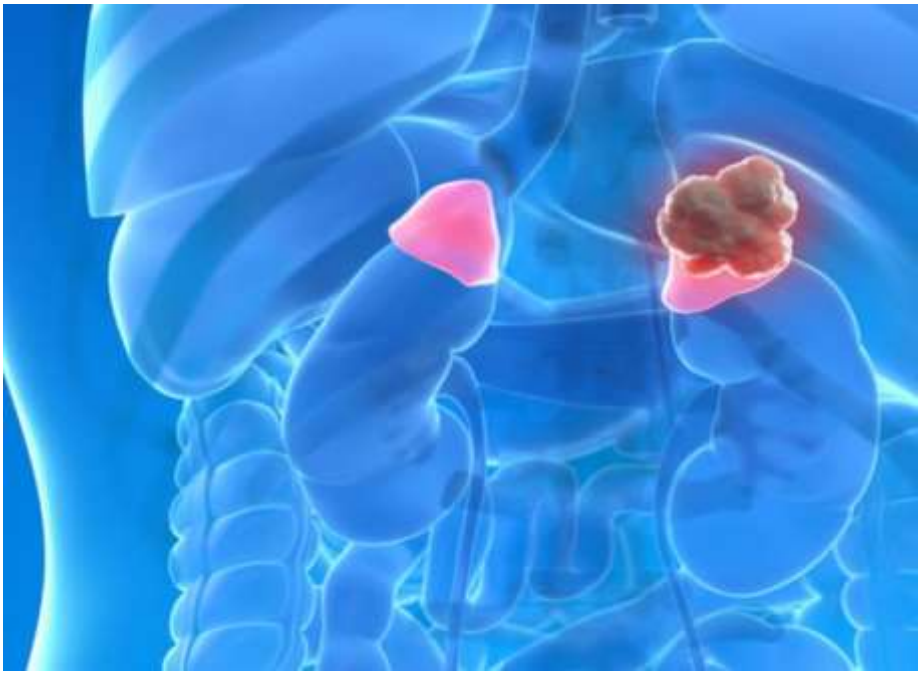

Figure (1.13): Adrenal glands tumor[60].

1.4.4. HIV virus

HIV Once an individual has been infected with the HIV, it implies that the virus has found its way in his or her blood. The primary victim of HIV is a particular form of white blood cell, known as a CD4 cell, that is a key commander in the immune system of the body against infection as shown in Fig. (1.13). The virus enters these cells and replicates itself into millions of copies with the help of these cells. In the process, it kills the CD4 cells. In a span of years, when the infection is left untreated by means of medication, the virus over time destroys so many of these cells, to the point that the immune system becomes extremely weak. By that time the body will not be able to resist the widespread diseases and the infection develops a stage known as the AIDS. Nowadays, HIV-positive people are able to lead a long and healthy life with appropriate treatment keeping the virus in control **[**61**].**

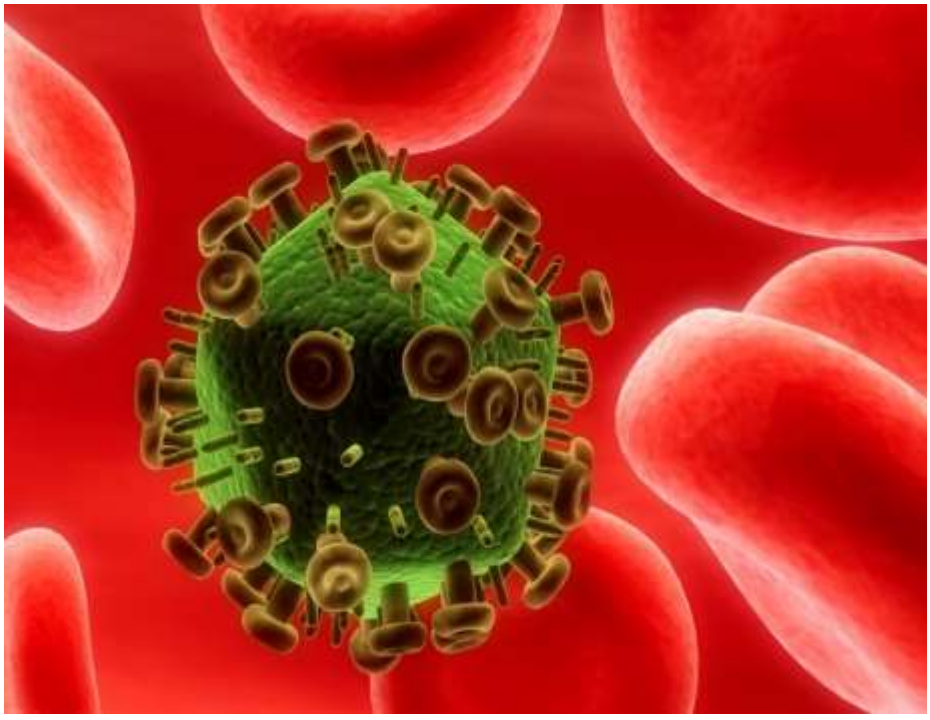

Figure (1.14): HIV virus**[**61**]**

1.4.5. Biochemical materials

Biochemical materials the natural chemical components of living organisms are known as biochemical materials. These are the substances and molecules that are necessary for life. Consider them the components and mechanics of each and every cell in your body. the formula of Glucose is $C_6H_{12}O_6$.as shown in Fig. (1.15). It is made from water and carbon dioxide during photosynthesis by plants It is used by plants to make cellulose, in energy metabolism, glucose is the most important source of energy in all organisms. Glucose circulates in the blood of animals as blood sugar[62].

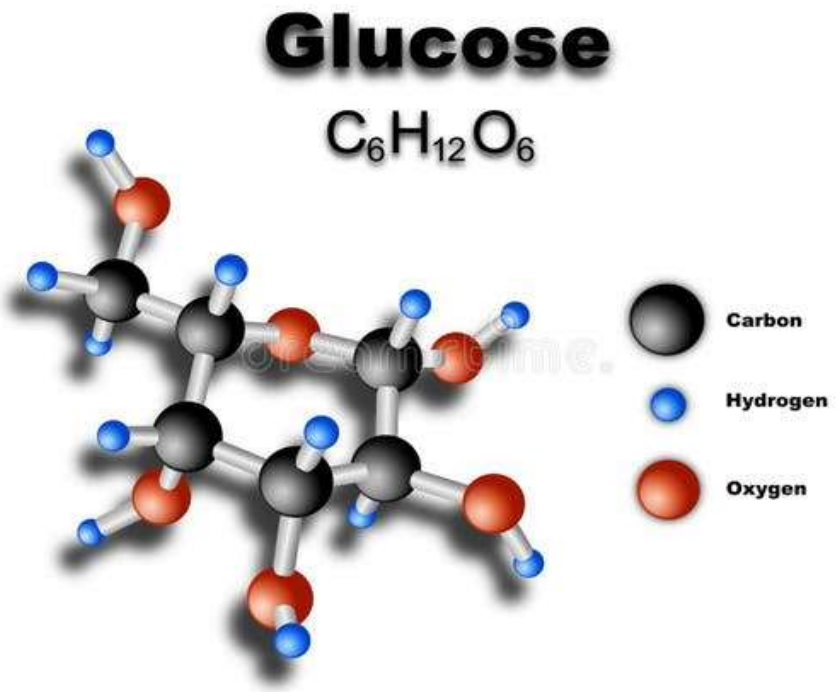

Figure (1.15): Glucose structure [62].

1-5 Aim of the Research

The main objective of the study is to design, numerically model, and characterize a highly sensitive biosensor using a Photonic Crystal Fiber (PCF) platform in combination with Surface Plasmon Resonance (SPR), to detect and differentiate between various biological analytes with particular emphasis made on different

types of cancer cells and viruses. This objective is further subdivided into some main goals:

To Propose a Novel Sensor Design: To prepare a special circular PCF design with an optimized air-hole lattice and a circumferential gold film being strategically located in order to excite plasmids on the surface efficiently.

To Compare Plasmonic Metal Performance: To compare and defend the choice of gold over silver as the plasmonic material on the basis of chemical stability, sharpness of resonance, one needs to note that silver may be sharper than gold as a resonant material, but poorer as an oxidizer because of its chemical activity.

To Optimize Structural Parameters: To probe the essential design parameters systematically and find optimal values of the key parameters in the design, such as air hole diameter (d), lattice pitch (Λ), and gold layer thickness (t_g), to find Maximum sensor performance measures such as sensitivity and resolution.

To Test Performance with Specific Analytes: To critically assess the performance of the sensor by in vitro simulation of sensor response to various clinically relevant targets, such as cancer cells (HeLa, Jurkat, PC12, MDA-MB-231, MCF-7), HIV virus and general biochemical molecules. **To measure the key performance indicators**, such as wavelength sensitivity (S_λ), amplitude sensitivity (S_A) and resolution (R_λ) and Figure of Merit (FOM) to prove that the sensor is better than the existing designs.

Chapter Two

Physical phenomena

2.1 Introduction

The interaction of light and matter in nanostructured metallics gave rise to the emergence of plasmonics, a fresh and creative area of photonics. Thin plasmonic circuits made of the same metal can transport optical signals and electric currents, enabling the combination of the advantages of electronics and the greater technological advantages of photonics on the same chipset [63]. Many studies have concentrated on studying Surface Plasmon Polaritons (SPPs) in recent years [64]. The SPPs exhibit remarkable optical characteristics of metallic nanostructures, allowing for manipulation of light beyond the diffraction limit, which presents exciting possibilities for the use of optical interconnections at the nanoscale. Nevertheless, the SPPs often experience significant losses due to the internala bsorption inveterate in the metal. Low losses photonic devices can be obtained from common dielectric materials. Hence, combining plasmonic technology along with common photonic devices on similar chips is considered the best choice to take the advantages of each technology [64].

2.2 Plasmonic

An electromagnetic transverse mode wave called a surface plasmon wave travels along the boundary between metal and dielectric. As a result of free charge oscillation in metal, plasmonic waves are light waves that are trapped at the conductor's surface. The electromagnetic fields and charges of plasmonic waves scattered on the metal's surface and in its dielectric are shown in Figure (2.1), where x denotes the direction of propagation [65].

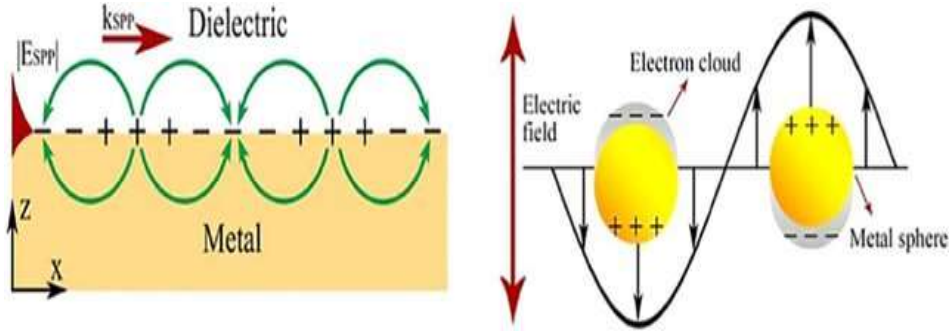

Figure (2.1): Plasmonic wave at the surface of metal and dielectric [65].

At the same frequency, the surface plasmon wave number is greater than the light wave number. The SP wave's restriction to the surface is to blame for this [65]. It

is necessary to correct this mismatch in order to couple light into the SP mode. The most popular method sends the light wave into the prism using prism coupling. Due to the greater refractive index of the prism, the light wave vector is higher in the prism and can match the SP wave vector. In the second technique, an SP wave is locally excited using a topological defect, such as a hole in the surface. Grating coupling is a different technique for energizing the SP wave [66]. Diffracted incident light's wave vector can match the SP wave vector.A binding between the SP wave and the dielectric metal surface is resulted that leads to an exponential decay of the electric field. The plasmonic wave will propagate down the surface once it has been stimulated, but due to metal absorption loss, its intensity will rapidly diminish [66].

2.3 Maxwell's Equations and Wave Equation

The Maxwell's equations define the electric (E) and magnetic (H) fields characteristics in the media. They are represented by four partially differentiated equations. The E and H may be expressed in the frequency domain by substituting $\frac{\partial}{\partial t} = -i\omega$, as

$$\nabla \times \mathrm{E} = -j\omega\mu H \quad (1)$$

$$\nabla \times \mathrm{H} = j\omega\varepsilon E \quad (1)$$

$$\nabla . (\varepsilon \mathrm{E}) = \rho \quad (1)$$

$$\nabla . (\mu H) = 0 \quad (1)$$

When the vector values E and H resemble, respectively, $\varepsilon = \varepsilon_0\varepsilon_r$, and $\mu = \mu_0\ \mu_r$ the vectors of the magnetic and electric fields. The medium electromagnetic charactristics are determined by the tensor of permittivity, and the permeability of the waveguide material. The open space permeability and permittivity are ε_0 =8.854×10^{-12} F/m and μ_0 = 4π×10^{-7}H/m, respectively. ε_r is the relative permittivity, while μ_r is the permeability of the waveguide material. During this study, μ_r is treated as one [67].

To obtain the wave equations, it is assumed that an optical waveguide is taken which is only capable of supporting electric or magnetic part only. The curl of the magnetic field may be taken in this study to remove the electric field in derivation

and replace it with the use of Eq. (1a). Therefore, the vector of magnetic field can be modeled by a vector wave equation, as:

$$\nabla \times (\varepsilon_r^{-1} \nabla \times H) - k_0^2 H = 0 \qquad (2)$$

Where k_0 represents the free space wave number which can be found from ($k_0^2 = \omega^2 \varepsilon_0 \mu_0$). If one of the material axes is in the direction of the waveguide, the concept of anisotropic material is introduced where its permittivity tensor can be revealed as [68]:

$$(\boldsymbol{\nabla} \times \left(\boldsymbol{AB}\right) = \boldsymbol{\nabla A} \times \boldsymbol{B} + \boldsymbol{\nabla A} \times \boldsymbol{B} \qquad (3)$$

For isotropic materials ($\varepsilon_{xx}, \varepsilon_{yy}, \varepsilon_{zz}$) are equals, also ($\varepsilon_{xy}$and ε_{yx})are equals to 0. During the current study, all waveguide materials is treated as isotropic. By using the following identity of vectors), the wave Eq. (2) may rephrase as:

$$\nabla^2 H + k_0^2 \varepsilon_r H = -\varepsilon_r^{-1} \nabla \varepsilon_r \times (\nabla \times H) \qquad (4)$$

In the transversal plane, the vector wave Eq. (4) may express as:

$$\nabla^2 H_t + k_0^2 \varepsilon_{rt} H_t = -\varepsilon_{rt}^{-1} \nabla_t \varepsilon_{rt} \times (\nabla_t \times H_t) \qquad (5)$$

Where, t denotes transversal components. ε_{rt} represents the transversal components of relative dielectric tensor, which can be defined by

$$\varepsilon_{rt} = \begin{bmatrix} \varepsilon_{xx} & \varepsilon_{xy} \\ \varepsilon_{yx} & \varepsilon_{yy} \end{bmatrix} \qquad (6)$$

When the divergence equation ($\nabla . H = 0$) is applied, it is possible to get the longitudinal magnetic component (H_z) from the transversal two components (H_x and H_y), where the z-dependence is presented by $e^{-j\beta z}$ for all field vectors.

$$H_z = \frac{1}{j\beta}\left(\frac{\partial H_x}{\partial x} + \frac{\partial H_y}{\partial y}\right) \qquad (7)$$

β is the propagation constant. Using the Eqs. (5) and (6), with divergence relation $\nabla . H = 0$, the full vector eigenvalue equation can be obtained, after some algebraic manipulations, as follows

$$\begin{bmatrix} A_{xx} & A_{xy} \\ A_{yx} & A_{yy} \end{bmatrix} \begin{bmatrix} H_x \\ H_y \end{bmatrix} = \beta^2 \begin{bmatrix} H_x \\ H_y \end{bmatrix} \qquad (8)$$

where A_{xx}, A_{xy}, A_{yx} and A_{yy} are the differential operators that could be identified through the following equations [68]

$$A_{xx}H_x = \frac{\partial^2 H_x}{\partial x^2} + \frac{\varepsilon_{yy}}{\varepsilon_{zz}}\frac{\partial^2 H_x}{\partial y^2} + \frac{\varepsilon_{yx}}{\varepsilon_{zz}}\frac{\partial^2 H_x}{\partial y \partial x} + k^2\varepsilon_{yy}H_x \quad (9)$$

$$A_{xy}H_y = \left(1 - \frac{\varepsilon_{yy}}{\varepsilon_{zz}}\right)\frac{\partial^2 H_y}{\partial x \partial y} - \frac{\varepsilon_{yx}}{\varepsilon_{zz}}\frac{\partial^2 H_y}{\partial x^2} - k^2\varepsilon_{yx}H_y \quad (9)$$

$$A_{yx}H_x = \left(1 - \frac{\varepsilon_{xx}}{\varepsilon_{zz}}\right)\frac{\partial^2 H_x}{\partial x \partial y} - \frac{\varepsilon_{xy}}{\varepsilon_{zz}}\frac{\partial^2 H_x}{\partial y^2} - k^2\varepsilon_{xy}H_x \quad (9)$$

$$A_{yy}H_y = \frac{\partial^2 H_y}{\partial y^2} + \frac{\varepsilon_{xx}}{\varepsilon_{zz}}\frac{\partial^2 H_y}{\partial x^2} + \frac{\varepsilon_{xy}}{\varepsilon_{zz}}\frac{\partial^2 H_y}{\partial x \partial y} + k^2\varepsilon_{xx}H_y \quad (9)$$

When all three components of the magnetic field (*H*) are defined, the electric flux density (*D*) can be calculated from ($\nabla \times H = j\omega D$), which gives:

$$D_x = \frac{-1}{\omega\beta}\left(\frac{\partial^2 H_x}{\partial y \partial x} + \frac{\partial^2 H_y}{\partial y^2}\right) + \frac{\beta}{\omega}H_y \quad (10)$$

$$D_y = \frac{1}{\omega\beta}\left(\frac{\partial^2 H_y}{\partial x \partial y} + \frac{\partial^2 H_x}{\partial x^2}\right) - \frac{\beta}{\omega}H_x \quad (10)$$

$$D_z = \frac{j}{\omega}\left(\frac{\partial H_x}{\partial y} - \frac{\partial H_y}{\partial x}\right) \quad (10)$$

The electric field is calculated from D by applying (E = ε^{-1} D) as follows:

$$\begin{bmatrix} E_x \\ E_y \end{bmatrix} = \frac{1}{\varepsilon_0(\varepsilon_{xx}\varepsilon_{yy} - \varepsilon_{xy}\varepsilon_{yx})}\begin{bmatrix} \varepsilon_{yy} & -\varepsilon_{xy} \\ -\varepsilon_{yx} & \varepsilon_{xx} \end{bmatrix}\begin{bmatrix} D_x \\ D_y \end{bmatrix} \quad (11)$$

$$E_z = \frac{1}{\varepsilon_0\varepsilon_{zz}}D_z = \frac{j}{\omega\varepsilon_0\varepsilon_{zz}}\left(\frac{\partial H_x}{\partial y} - \frac{\partial H_y}{\partial x}\right) \quad (12)$$

2.4 Surface Plasmon Polaritons (SPP)

The surface plasmon polaritons are excited electromagnetic waves that travel along the interface plane between metals and a dielectric media. Such a vacuum is known as the surface plasmon polariton (SPP). The amplitude of this electromagnetic pulse exponentially decays in every medium with distance of the interface. The SPP wave electromagnetic field is restricted to the surrounding area near the interface between the metal and the dielectric medium. Thus, this captivity develops an improvement to the electromagnetic wave which results in an astonishing sensitive surface property of the SPPs. This property is widely used in examining adsorbates on a surface roughness while it is used in several chemo- and bio-sensor applications [69].

2.4.1 Planar SPPs

When a surface-plasmon polariton (SPP) propagates in a metal dielectric interface, the electromagnetic field is not simply the wiggle of the vacuum; it is the special mode of Maxwell equations that is required to obey the physics both within the metal and the dielectric surrounding of the metal. These fields are extinct infinitely far from the interface [70]. An SPP wave induced by a TM wave is shown in Figure (2.2) at the metal-dielectric interface. Figure (2.2) shows a planar metal-dielectric configuration.

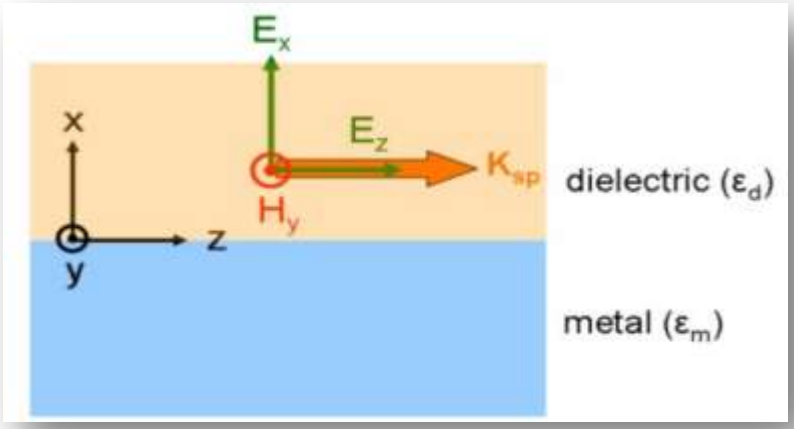

Figure (2.2): Geometric illustration of a surface plasmon polariton (SPP) propagating at the - dielectric medium interface when stimulated by a transverse magnetic (TM) wave. [69,70].

Taking into account the (TM) wave, in which the SSP propagates in the direction of z-axis- while the magnetic field exists outside the plane. The electric and magnetic fields in the dielectric medium (for$(x > 0)$,) can be given by:

$$\overrightarrow{E_d} = \begin{pmatrix} E_{xd} \\ 0 \\ E_{zd} \end{pmatrix} e^{i(k_{xd}x + k_{zd}z - \omega t)} \quad (13)$$

$$\overrightarrow{H_d} = \begin{pmatrix} 0 \\ H_{yd} \\ 0 \end{pmatrix} e^{i(k_{xd}x + k_{zd}z - \omega t)} \quad (14)$$

When $(x < 0)$, i.e in metals, the electric and magnetic fields can be expressed by:

$$\overrightarrow{E_m} = \begin{pmatrix} E_{xm} \\ 0 \\ E_{zm} \end{pmatrix} e^{i(k_{xm}x + k_{zm}z - \omega t)} \quad (15)$$

$$\overrightarrow{H_m} = \begin{pmatrix} 0 \\ H_{ym} \\ 0 \end{pmatrix} e^{i(E_{xm}x + E_{zm}z - \omega t)} \quad (16)$$

From Maxwell's equation we have

$$\nabla \times \overrightarrow{H_\iota} = \epsilon_i \frac{\partial \vec{E}}{\partial t} \quad (17)$$

Where the subscript i denotes the materials, $\vec{E}$ and $\vec{H}$ are the electric [V/m], magnetic [A/m] fields, respectively. ϵ represents the dielectric permittivity. It can be expanded as:

$$L.H.S = \left(\frac{\partial H_{zi}}{\partial y} - \frac{\partial H_{yi}}{\partial z}\vec{x}\right) + \left(\frac{\partial H_{yi}}{\partial x} - \frac{\partial H_{xi}}{\partial y}\vec{z}\right)$$

$$= ik_{zi}H_{yi}e^{i(k_{xi}x + k_{zi}z - \omega t)}\vec{x} + ik_{xi}H_{yi}e^{i(k_{xi}x + k_{zi}z - \omega t)}\vec{z} \quad (18)$$

$$R.H.S = \begin{pmatrix} E_{xi} \\ 0 \\ E_{zi} \end{pmatrix} (-i\omega\epsilon_i)e^{i(k_{xd}x + k_{zd}z - \omega t)} \quad (19)$$

applying equations 18 and 19 to the metal structure, we have

$$\frac{k_{xm}}{\epsilon_m}\frac{H_{ym}}{H_{yd}} = \frac{k_{xd}}{\epsilon_d}\frac{E_{zm}}{E_{zd}} \quad (20)$$

the applied of the boundary condition at the interface, where $E_{zm}=E_{zd}$ and $H_{ym}=H_{yd}$, provides

$$\frac{k_{xm}}{k_{xd}} = \frac{\epsilon_m}{\epsilon_d} \quad (21)$$

The wavevectors are associated with:

$$k_i = k_x^2 + k_z^2 = \epsilon_i(\frac{\omega}{c})^2 \quad (22)$$

From eq. (2.21) and (2.22), we find

$$k_z^2 = \epsilon_m(\frac{\omega}{c})^2 - k_{xm}^2 \qquad (metal, x < 0) \quad (23)$$

$$k_z^2 = \epsilon_d(\frac{\omega}{c})^2 - k_{xd}^2 \qquad (dielectric, x > 0) \quad (24)$$

Substituting Eq. (21) and (23) into Eq. (24) yields

$$k_z^2 = (\frac{\omega}{c})^2(\frac{2\epsilon_d\epsilon_m}{\epsilon_d+\epsilon_m}) \quad (25)$$

$\epsilon_m = \epsilon'_m + i\epsilon''_m$ and $\epsilon''_m < |\epsilon'_m|$, The dielectric-metal interface's SPP dispersion relation can be found by:

$$Re(k_z) = (\frac{\omega}{c})\sqrt{\frac{\epsilon_d\epsilon'_m}{\epsilon_d+\epsilon'_m}} \quad (26)$$

$$Im(k_z) = (\frac{\omega}{c})(\frac{\epsilon_d\epsilon'_m}{\epsilon_d+\epsilon'_m})^{\frac{3}{2}}\frac{\epsilon''_m}{2\epsilon'^2_m} \quad (27)$$

The previous equations produce the dispersion features of the SPPs in a planar interface the standard Sellmeier expansion may evaluate the frequency-dependent dielectric function of the dielectric medium ϵ_d. On the otherside, the Drude model can obtain the complex frequency dependent dielectric function of metal ϵ_m[70].

The Drude model gave a convenient description of the dispersion relation of metal over a wide range of frequencies [71, 72]. The complex dielectric function may be represented as

$$\epsilon_c = \epsilon_1 + i\epsilon_2 \quad (28)$$

with:

$$\epsilon_c = \epsilon_\infty \frac{\omega_p^2}{\omega^2+i\omega\omega_\tau} \quad (29)$$

$\omega_p = \sqrt{\frac{n_e e^2}{\epsilon_0 m}}$ is the frequency of plasma, n_e represents the electron density, e is the electron charge, m is the electron mass, and ϵ_0 is the permittivity of free space. The electrons restore around their equilibrium positions due to a typical

electrostatic oscillation. $\omega_\tau = \frac{1}{2\pi c\tau}$ is the damping frequency where τ is the electron lifetime in seconds [70]. The permittivity of high frequency limit is ϵ_∞. By separating the real from the imaginary part.

$$\epsilon_1(\omega) = \epsilon_\infty - \frac{\omega_p^2}{\omega^2+\omega_\tau^2} \quad (30)$$

$$\epsilon_2(\omega) = \frac{\omega_p^2\omega_r^2}{\omega^3+\omega\omega_\tau^2} \quad (31)$$

2.5 Plasmonic Materials

Silver (Ag) and gold (Au) are the elements most frequently used as plasmonic materials. The advantage of using Ag is that it has little loss in the visible and near infrared (NIR) bands. Though, when it is related to nanoscaled-fabrication, dispite the degradation of Ag is relatively high, the threshold thickness for its homogenous continuous films is about (12-13 nm), which is considered as main barriers for transformation optics (TO), and for the other micro and nano-based devices. The substitute plasmonic materials such as Aluminum (Al) and Copper (Cu) appears promise because of its low cost and abundance. Furthermore, these two-materials exhibit surface plasmon resonance in the UV and visible frequencies, respectively. Though, these two elements have high optical and plasmonic losses compared to Ag and Au hence, confining their usage in several applications. Alternatively, due to their plasmonic potential, other nanometals, such as potassium, sodium and lithium, have revealed a high absorption efficiency along with very low losses of the inter-band transition at optical wavelengths [73].

Silver Nano rods have sparked a lot of scientific attention because of their exceptional optical qualities. These Nano rods have the advantage of being able to fine-tune their optical absorption properties by changing their aspect ratios [74].

2.6 Photonic crystal

Photonic crystal fibers (PCFs)also known as holey, microstructure, or micro-structured fibers are not guided by a graded glass composition; rather a lattice of microscopic air hole is carefully engineered that extends the full length of the fiber (see Figure 2.3). The initial stage in fabrication is usually the so-called stacked - tube technique: a preform is built by assembling a bundle of solid silica rods and hollow capillaries. This preform is initially fed through a fine cane (approximately 1mm diameter) and pulled once more to the ultimate standard optical-fiber size

(typically 125mm diameter). PCFs can be prepaed to control an extensive range of optical behavior as tuned dispersion or a highly nonlinear behavior [75, 76]

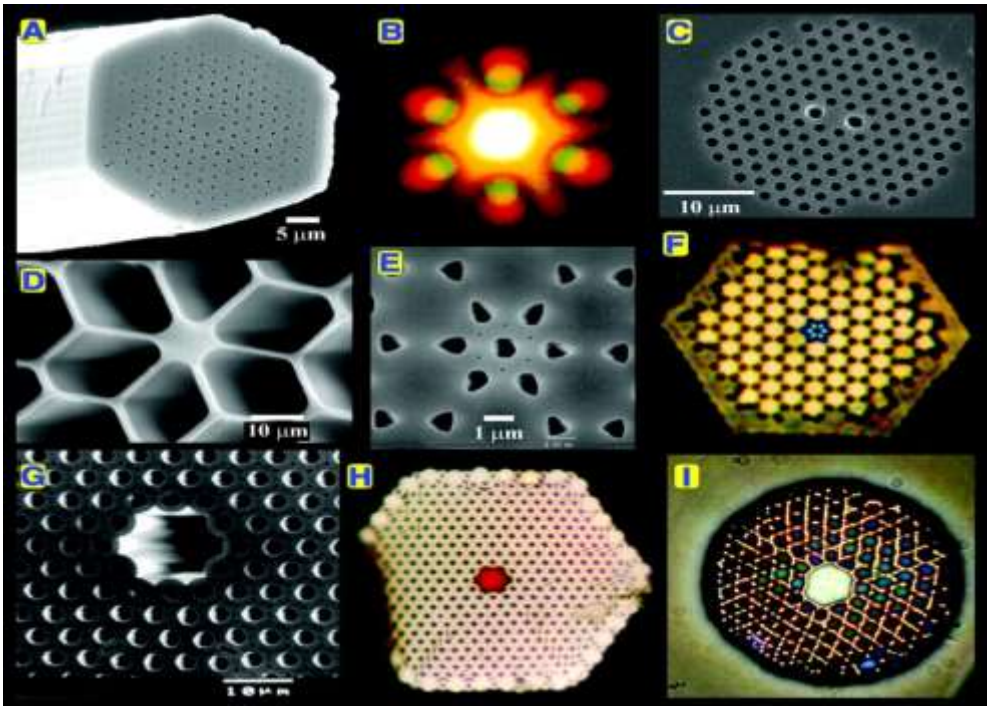

Figure (2.3): solid-core photonic crystal fiber for melty designs(A-I) [75]

2.7 Numerical Simulation in Photonic Crystal Fiber

A number of methods can be used to model the behavior of photonic crystal fibers. There are numerous approaches for simulating the behavior of photonic crystal fibers.

2.7.1 The Finite Element Method (FEM)

Partial differential equations (PDEs) can be numerically solved using a different method called the finite-element method (FEM). The main usage of the (FEM) is to simulate the characteristics of optical effects and device in the context of Nano-optical devices. The main benefits of finite-element methods include the accurate representation of complex geometric properties in real-world complications, the provision of highly precise results in comparatively short computation times due to superior convergence features, and the high stability with widespread applications of this method by using various settings of simulation [77].

2.7.1.1 Characteristics of FEM

The widespread adoption of finite element methods was linked to a number of significant traits and advantageous qualities, which are summarized as follows:

• The FEM is more flexible and can represent any arbitrary cross-section with greater accuracy.

• The FEM methodology is very adaptable, and one of its key strengths is the simplicity with which the location and size of any air hole may be changed to meet specific requirements.

• The cross-section of the structure and waveguide is splitted into a finite number of components throughout the FEM.

• Transfer of constructions made up of various material forms is possible since the material qualities of adjacent elements need not be equivalent.

• It is possible to successfully meet boundary needs including discontinuous surface loads and mixed boundary circumstances.

• Various shapes, sizes, and types of elements can be used in the same space, allowing the system to make the best use of the finite elements that are available.

2.7.1.2 Types of Elements

Finite elements can be categorized into (1D, 2D, or 3D). Selection of element is based on the dimensionality of the problem 1D elements in 1D problems and 2D elements in 2D problems. An important illustration of a two-dimensional element is the three-node triangle. In 3D problems, the basic component is the tetrahedron, which consists of four nodes; one node per corner of the tetrahedron (Figure 2.4(c) [78]. The values in any other point within the element are then estimated with functions of these nodal values. Nodes can be divided into external and internal. The external nodes are those that are found at the edges of an element whereas the internal nodes are those found in the interior of the element. Another difference is drawn between a primary and secondary node. Primary nodes are where the 1D elements end or where the corner of the 2D and 3D elements are. Secondary nodes refer to the nodes that are mounted on the element sides, i.e. not on its corners [78].

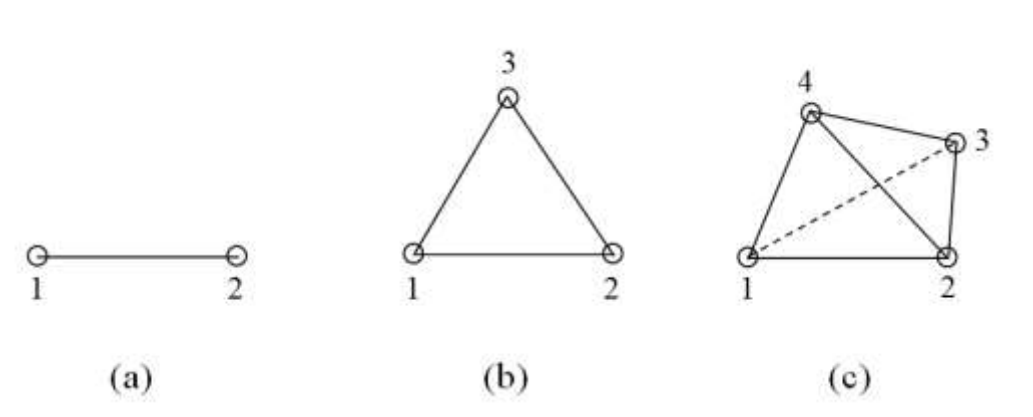

Figure (2.4): (a) 1D; (b) 2D; and (c) 3D elements [78].

2.7.1.3 Mathematical Formulation

The discretization of partial differential equations (PDE) using the finite element approach is both mathematically accurate and elegant [78]. Its basic idea is that the FEM is used to approximate the PDE rather that to create a sub-space with finite dimension of the original solution that has infinite dimension space with appropriate accuracy. The issue is resolved on this sub-space, which is space with finite-elements. The infirm PDE formulation is another concept of significance in FEM.

Typically, physical principles are expressed in what is known as a "strong form," such as frequency domain of Maxwell's equations Eq (1). The equations in eq. (1) are not closed. Although the electric and magnetic fields are related to the electric displacement (D = εE). and the magnetic flux density (B = μH), it is possible to derive only one equation concerning the electric field:

$$\nabla \times \mu^{-1} \nabla \times \mathbf{E} - \omega^2 \varepsilon \mathbf{E} = i\omega \mathbf{J} \qquad (32)$$

the electromagnetic field is generated by electric current J,Using FEM, the electric field equation must be placed in infirm formulation. Firstly, it is tested on a vectorial function Ø and integrated on $\mathbb{R}^3$:

$$\int_{R^3} \emptyset \nabla \times \mu^{-1} \nabla \times \mathbf{E} - \omega^2 \emptyset \varepsilon \mathbf{E} = i\omega \int_{R^3} \emptyset \mathbf{J} \tag{33}$$

The evaluation based on integration by parts, and a supposition of disappearance of the electric field at infinity, yields:

$$\int_{R^3} \nabla \times \emptyset \mu^{-1} \nabla \times \mathbf{E} - \omega^2 \emptyset \varepsilon \mathbf{E} = i\omega \int_{R^3} \emptyset \mathbf{J} \tag{34}$$

To have a compact expression of the Maxwell's equations weak form, the linear and bilinear forms are introduced:

$$a(\emptyset, \mathbf{E}) = \int_{R^3} \nabla \times \emptyset \mu^{-1} \nabla \times \mathbf{E} - \omega^2 \emptyset \varepsilon \mathbf{E}, \quad f(\emptyset) = i\omega \int_{R^3} \emptyset \mathbf{J} \tag{35}$$

The Maxwell's equations weak form is shown as:

Find $\mathbf{E}$ ε $\mathbf{H}$ $(\nabla \times)$ such that

$$a(\emptyset, \mathbf{E}) = f(\emptyset), \quad \forall \emptyset \, \epsilon \, \nabla \times \mathbf{H} \tag{36}$$

Given that field $\mathbf{E}$ is a solution to Maxwell Eq. (1), then it also represents a solution for the infinite-dimensional of the variational formulation [79].

2.7.1.4 Finite-Element Discretization

The variational formulation of Maxwell equations can only be defined on a finite element subspace of finite dimension. V_h, V_h = N <∞.

Find $\mathbf{E}_h$ ε V_h such that:

$$a(\emptyset_h, \mathbf{E}_h) = f(\emptyset_h), \quad \forall \emptyset_h \, \epsilon \, V_h \tag{37}$$

where $\mathbf{E}_h = \sum_{i=1}^{N} e_i \, \varphi_i$. The investigation of the variational problem with all of the basis elements provides a linear system of equations:

$$\sum_{i=1}^{N} a(\varphi_j, \varphi_i) e_i = f(\varphi_j), \quad \forall j = 1, \ldots, N \tag{38}$$

e_i is expansion coefficients of the electric field, and $a(\varphi_j, \varphi_i)$ is scattered matrix can be determine using effective scattered LU solvers. The creation of the fundamental functions i is a crucial component of FEM. A triangulator divides the realm of interest into a number of little patches for their definition. The ability to breakdown essentially arbitrary geometries using unstructured meshes and various patches, such as the 2D shapes of triangles and quadrilaterals and 3D shapes of prisms, tetrahedrons, pyramids, and bricks, is a key advantage of FEM. It is acceptable to employ even curved that called isoparametric elements. The process of developing Maxwell's equations is difficult. In order to reach to well-constructed problems without creating false solutions, the characteristics of the two differential operators (∇.) and (∇×) that exist in Maxwell's relations is identified [80].

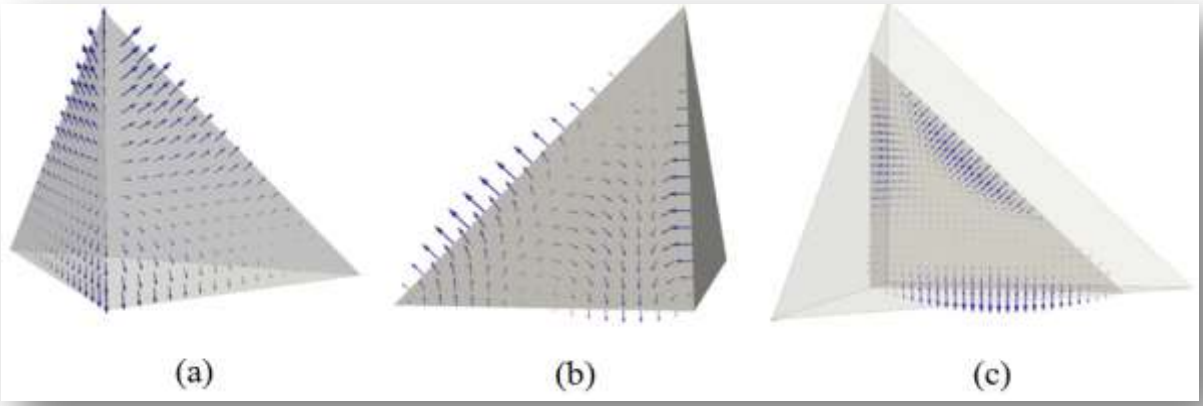

Figure (2.5): Higher-order finite-element functions that conform to H (∇×) on a tetrahedron [80]

Chapter three

COMSOL Simulation

3.1 COMSOL Simulation

COMSOL Multiphysics® version 6.3 was used to build the simulation. A photonic crystal fiber (PCF) is made up of microstructured optical fibers that guide light, whereas a step index fiber directs light through the high refractive index of the core.

3.1.1 Dimension of Space

The model was constructed using a 2D axisymmetric space dimension, which we can select when opening a new file in the COMSOL Multiphysics program. The 2D axisymmetric icon looks like this in Fig. (3.1).

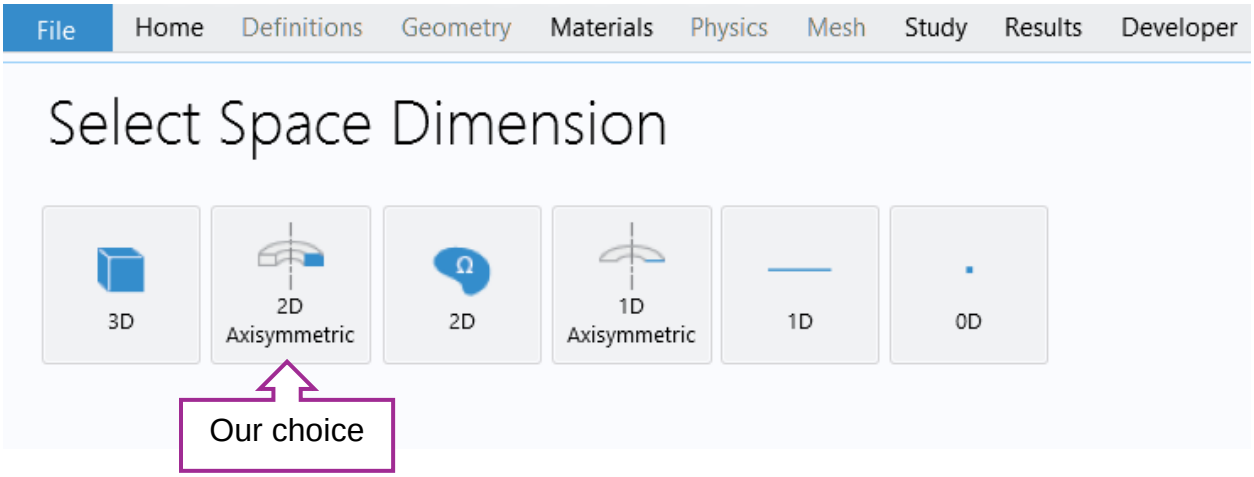

Figure (3.1): select space Dimension

3.1.2 Defining Physics and Study

The next step is to choose which kind of physics will be used in the simulation after the spatial dimension has been defined. In the "Select Physics" window are optics, wave optics, electromagnetic waves, Frequency Domain (emfd) as shown in Fig. (3.2).

Figure (3.2): Select Physics window in COMSOL

Selecting the kind of study was the next step after defining physics. Figure (3.3) shows the "Select Study" window

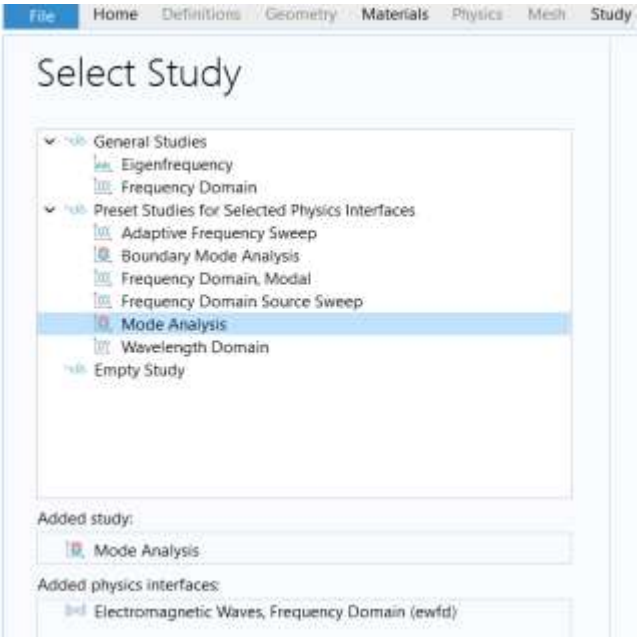

Figure (3.3): Select Mode Analysis

3.1.3 Structural design

The two-dimensional cross-sectional shape of our single-core (PCF) sensor concept is depicted in Fig. **(3.4)**. There are two separate circulars of the air hole in the microstructure. The core-cladding boundary is defined by an inner ring of eight circular holes, while the evanescent field is improved and its overlap with the surface plasmonic layer is improved by an outer rectangle arrangement of six holes. In this schematic, parameter (d) represents larger air hole diameter, and (Λ) signifies pitch, or center-to-center distance from the fiber's core to neighboring holes. Figure (3.5) shows the mesh diagram of proposed design model. As Fig. **(3.6)** shows, broadband light (500–1100 nm) polarizes and couples via a single-mode fiber (SMF) into the photonic crystal fiber (PCF). An analyte inlet directs samples to the gold-coated sensing region for interaction. Resonance shifts in transmitted spectra are precisely detected utilize an optical spectrum analyzer (OSA) to ensure accurate measurements.

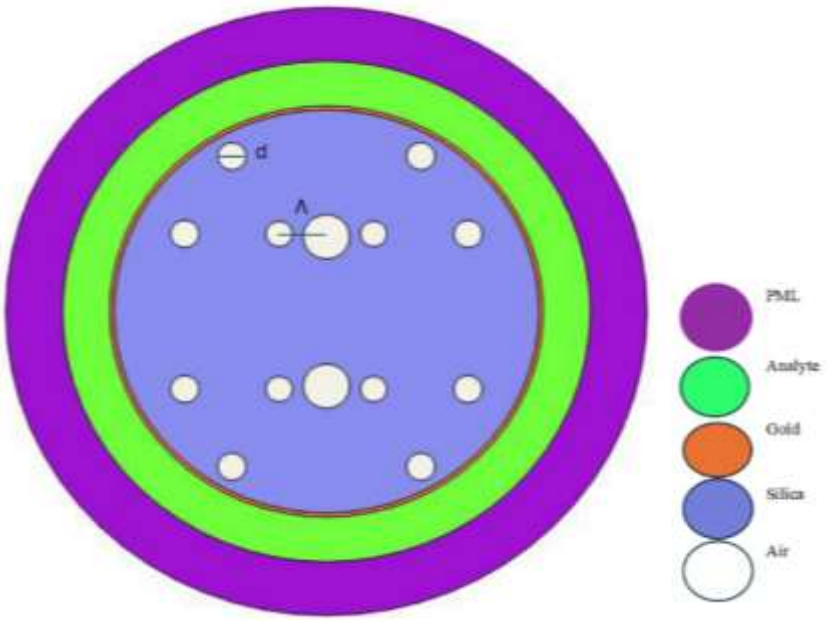

Figure (3.4). Diagram of the proposed PCF sensor design.

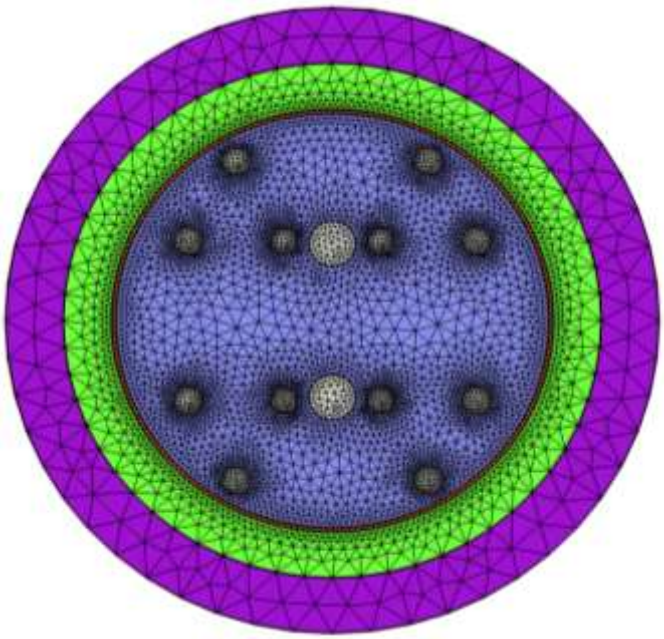

Figure (3.5). Mesh diagram of the proposed PCF sensor design.

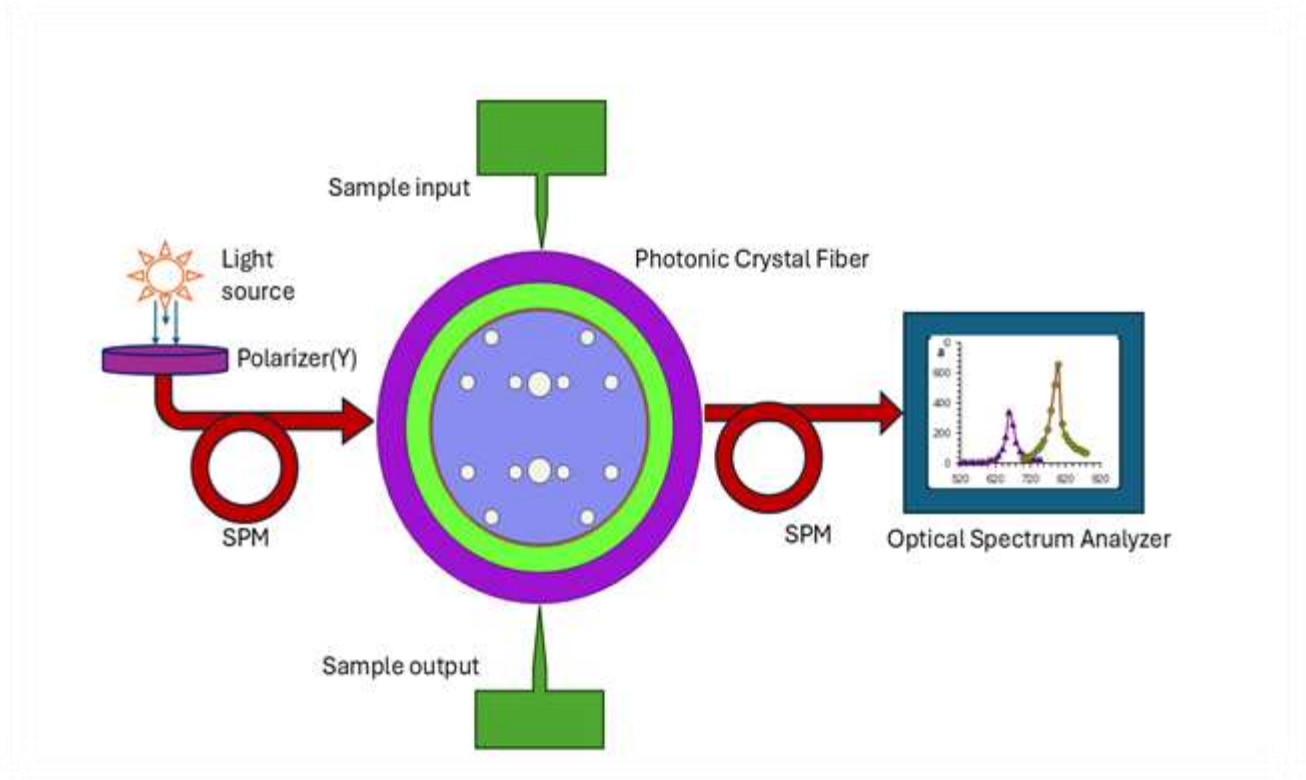

Figure (3.6). An experimental configuration for the proposed PCF sensor design.

It is necessary to compute the dielectric constant ε_G of Au in order to determine its refractive index. The Drude-Lorentz model, which is provided by the following equation, is used for this: [81, 82]

$$n_G = \sqrt{\varepsilon}_{Au} = \sqrt{1 - \frac{\lambda^2\ \lambda_c}{\lambda_p + (\lambda_c + i\lambda)}} \qquad (39)$$

The refractive index (n_{SiO_2}) for fused silica [83] is determined utilizing the Sellmeier equation, which is articulated as follows:

$$n_{SiO_2} = \sqrt{\varepsilon_{SiO_2}} = \sqrt{1 + \sum_{i=1}^{3} \frac{A_i \lambda^2}{\lambda^2 - B_i}} \qquad (40)$$

where the parameters for equations 1 and 2 given in Table1

Table 1. parameters of equations 1 and 2[82, 83]

λ_c(m)	λ_p(m)	A_1	A_2	A_3	B_1(μm^2)	B_2(μm^2)	B_3(μm^2)
8.9342× 10^{-6}	1.6826×10^{-7}	0.6962	0.408	0.89	0.00468	0.0135	97.934

It is important to calculate the amount of confinement loss (dB/cm) by using the imaginary part Im (n_{eff}) of the refractive index (RI) and the unit of λ is (nm), which can be determined by: [84, 85]

$$CL = 8.686 \times 2\pi/\lambda \times \text{Im}\ (n_{eff}) \times 10^4 \qquad (41)$$

The equation that shows how light waves travel and interacts with materials is as follows:

$$\nabla^2 \boldsymbol{E} + k_0^2 n^2(x,y)\boldsymbol{E} = 0 \qquad (42)$$

$\boldsymbol{E}$ the electric field of light waves, k_0 the wave number, n (x, y) the refractive index everywhere in the x–y plane in the region occupied by the core [86]. Figs. (3.7) and (3.8) display the confinement loss spectra for the core mode under x- and y-polarization.

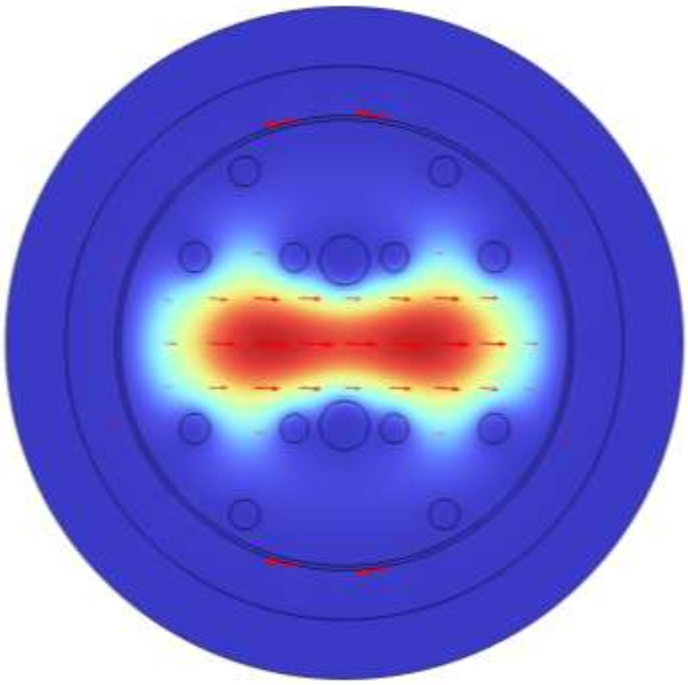

Figure (3.7) Display the field distribution for x -polarization at λ_r = 620 nm.

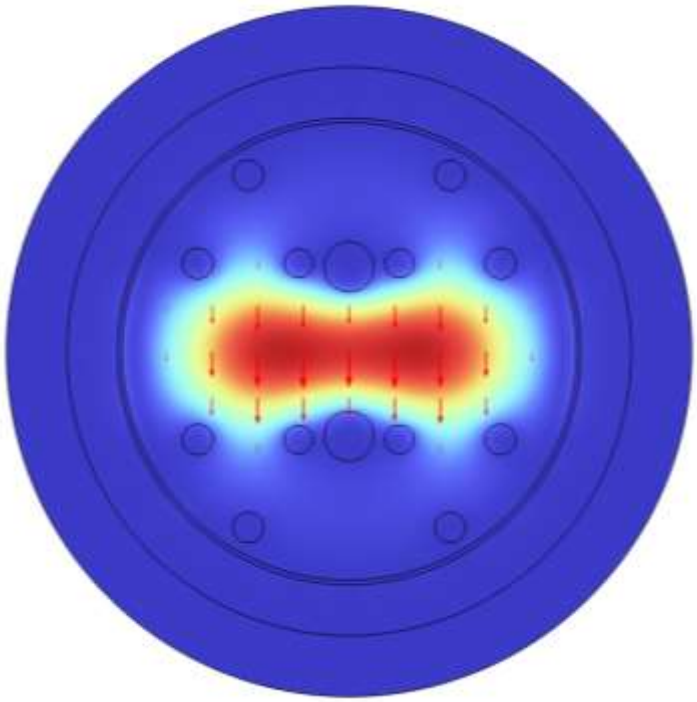

Figure (3.8) Display the field distribution for y-polarization at λ_r = 620 nm.

The corresponding E-field distributions in Figs. (3.9a) and (3.8b) visualize this energy transfer, showing guided light penetrating the cladding to excite SPPs at the resonant wavelength. A resonant loss peak for Y-polarized light at 630 nm signifies the phase-matching condition, where the real effective indices of the core and SPP modes converge as shown in Figs. (3.9c) and (3.9d). Maximum energy transfer from the core mode to the surface plasmon polariton mode on the gold layer is made possible by this convergence.

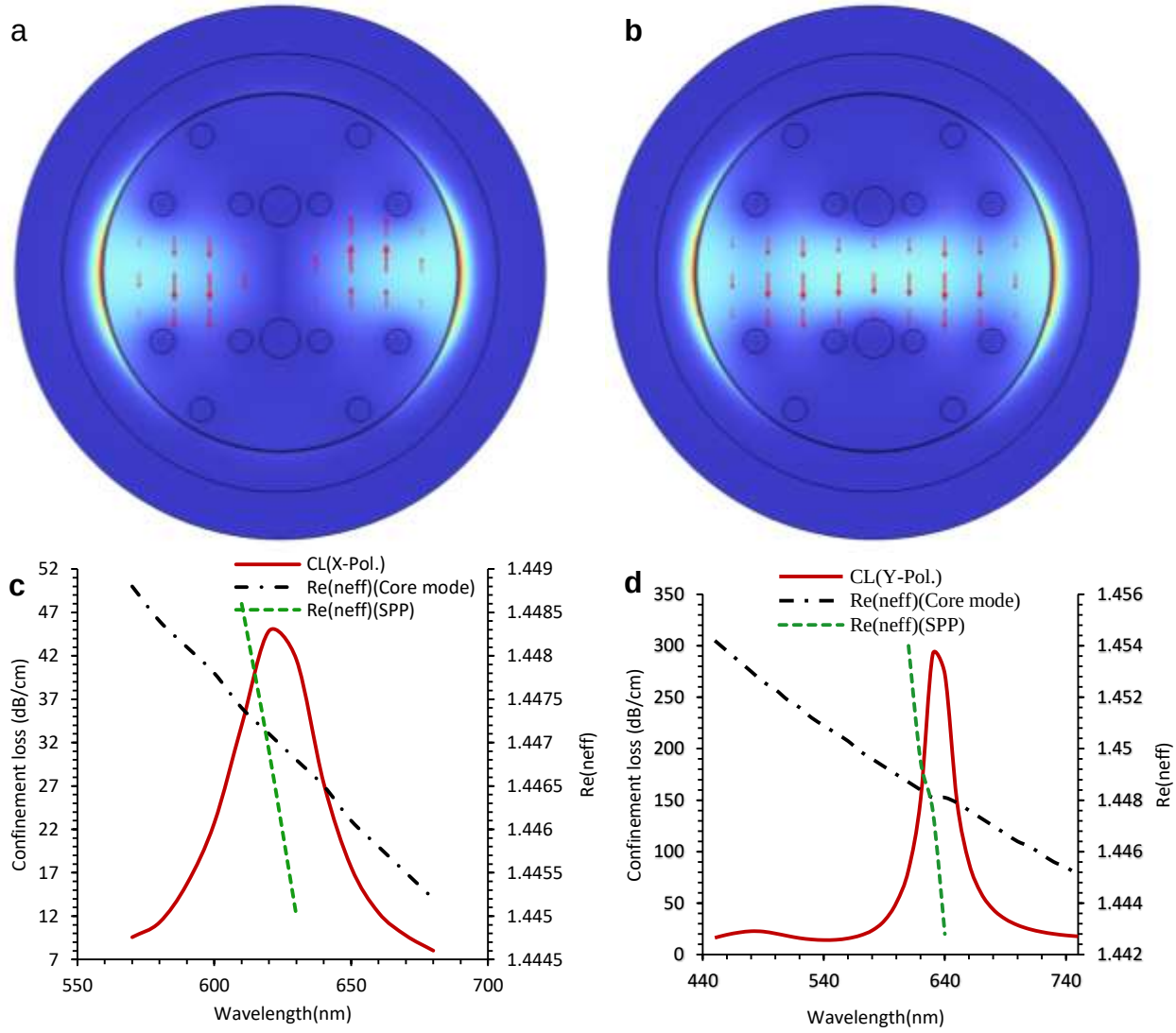

Figure (3.9) Display the field distribution for **a, b** SPP mode for Y-polarization. **c, d** phase matching condition and the confinement loss spectra for the core mode under X- and Y-polarization at analyte RI 1.35

A comparison of the confinement loss in Figs. (3.9c) and (3.9d). reveals stronger core-to-SPP coupling for Y-polarized light, as evidenced by its significantly higher loss peak relative to the X-polarized case. This indicates more efficient energy transfer for the Y-polarization. Consequently, all subsequent analyses of sensor performance were conducted using Y-polarized light.

3.2 Optimization of the Biosensor's Structural

3.2.1 Optimization of the pitch parameter (Λ)

The confinement loss is significantly influenced by variations in the pitch parameter (Λ), Figures **(3.10a), (3.11a),** and **(3.12a)** show E-field distributions with varying pitch (Λ). The spectral loss exhibits an inverse correlation with the pitch; the loss decreases as Λ increases. The calculated peak CL values for pitches of **0.9 µm**, 1.2 µm, and 1.8 µm are **294.8 dB/cm**, 293.9 dB/cm, and 219.2 dB/cm, respectively as shown in Figs. **(3.10b), (3.11b),** and **(3.12b).** Notably, the resonant wavelength remains stable and does not shift with changes in (Λ). Based on the peak confinement loss values, the optimal parameter for the proposed design is **0.9 µm**.

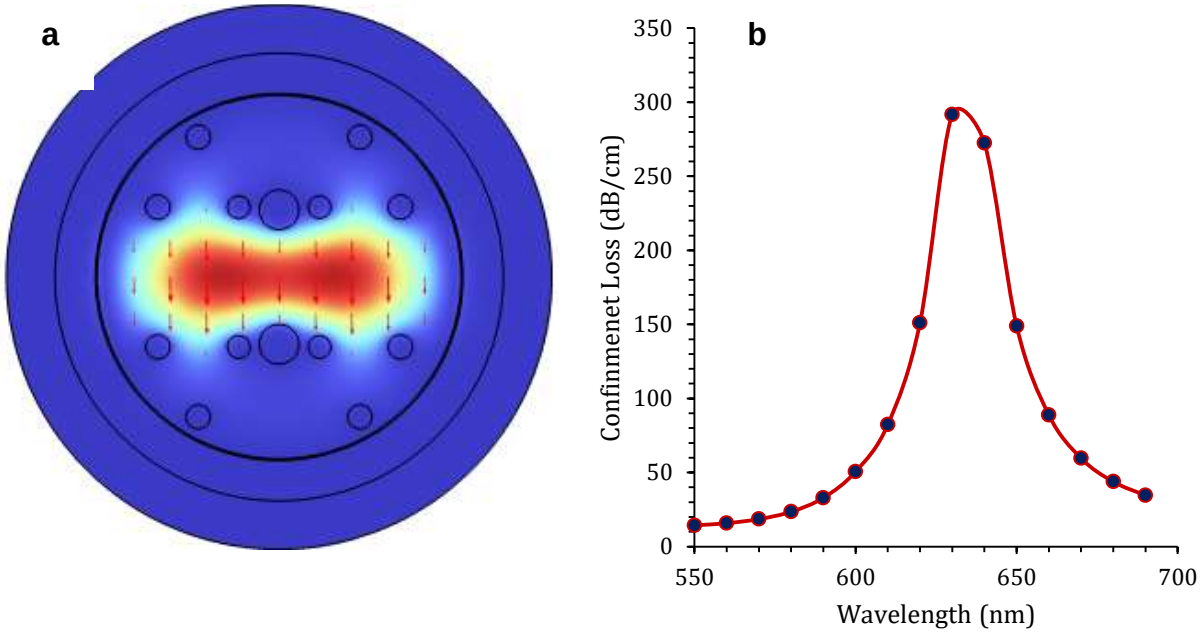

Fig. (3.10 a) Display the field distribution for Y-polarized light (**b)** Confinement loss variation with a refractive index (RI) of 1.35 for; air hole diameter d=0.3 µm, and pitch Λ=0.9 µm.

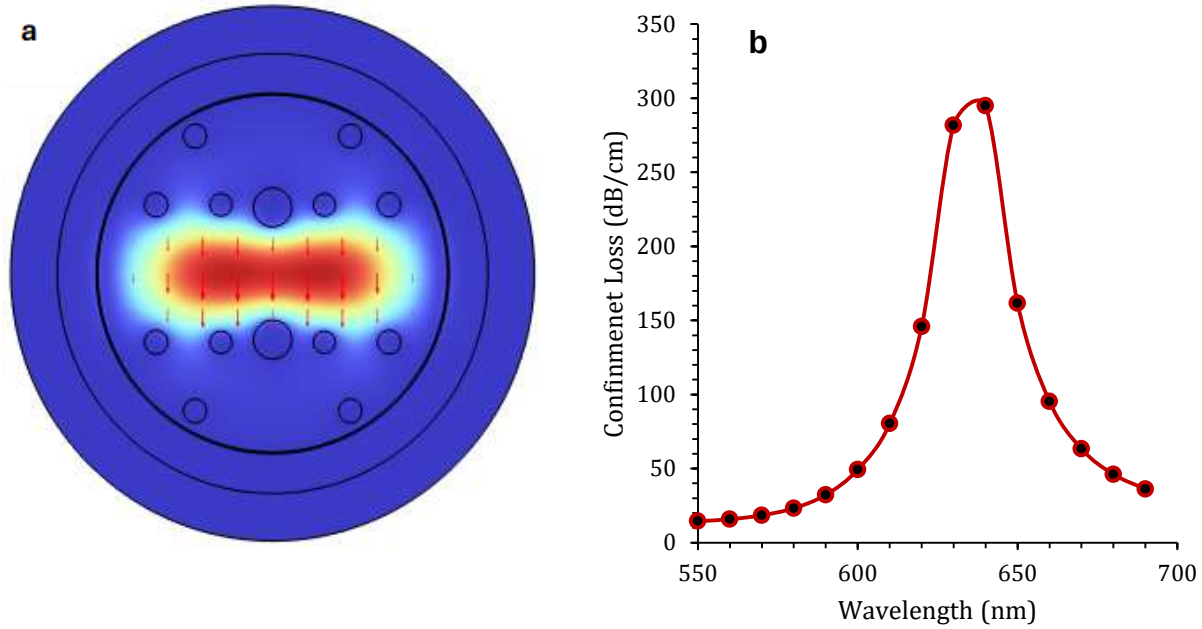

Figure (3.11) a. display the field distribution for Y-polarized light **b** Confinement loss variation with a refractive index (RI) of 1.35 for; air hole diameter d=0.3 μm, and pitch Λ=1.2 μm.

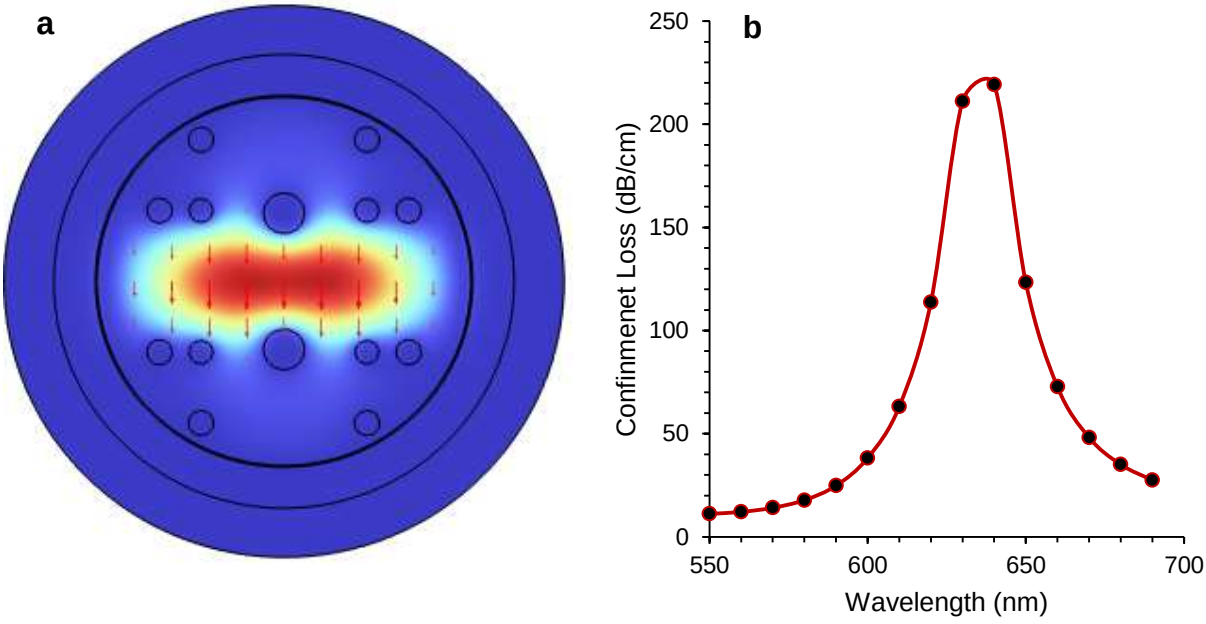

Figure (3.12) a. display the field distribution for Y-polarized light **b** Confinement loss variation with a refractive index (RI) of 1.35 for; air hole diameter d=0.3 μm , and Λ=1.8 μm.

3.2.2 Optimization of the air hole diameter (d)

Confinement loss (CL) was the key metric used to optimize the sensor's structural parameters. Figures **(3.13a), (3.14a),** and **(3.15a)** show E-field distributions with varying air hole diameter (d). The impact of the large air hole diameter (d) on the CL spectrum is shown in Figures (3.13b), (3.14b), and (3.15b). The results show a clear inverse relationship: as the hole diameter increases, the peak confinement loss decreases significantly. The peak CL values for diameters of **0.3 µm**, 0.6 µm, and 0.9 µm are **291.70 dB/cm**, 103.47 dB/cm, and 15.51 dB/cm, respectively. the resonant wavelength remains stable and does not shift with changes in (d). The proposed design's optimum parameter is 0.3 µm, as determined by peak confinement loss values.

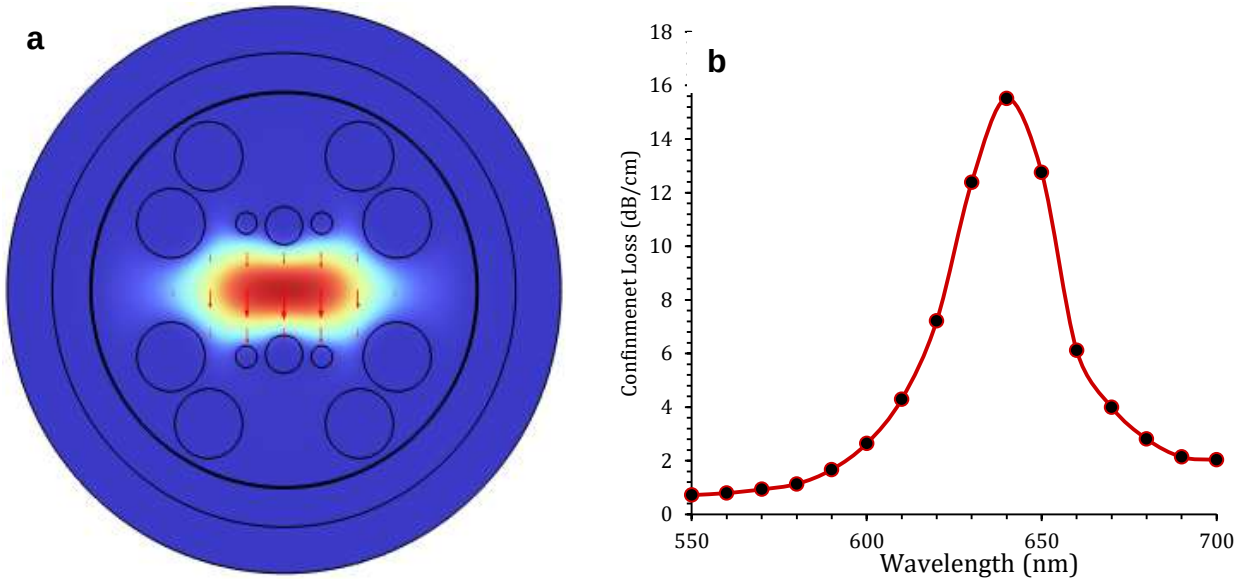

Figure (3.13 a) display the field distribution for Y-polarized light **b** Confinement loss variation with a refractive index (RI) of 1.35 for; air hole diameter d=0.9 µm , and Λ=0.9 µm.

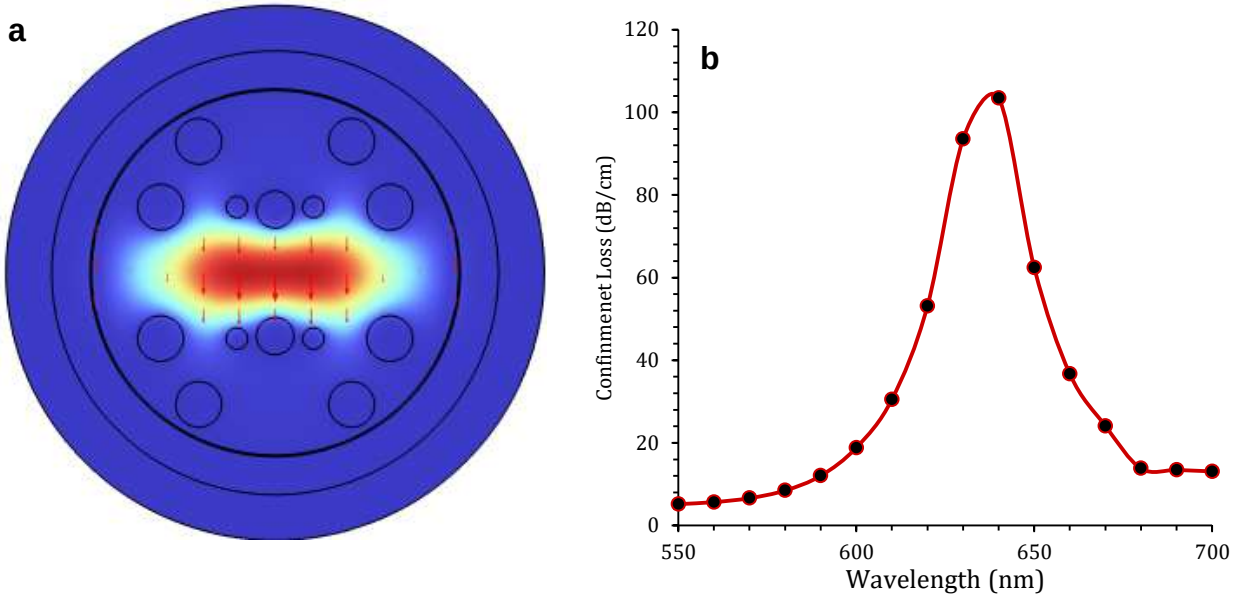

Figure (3.14) a. display the field distribution for Y-polarized light **b** Confinement loss variation with a refractive index (RI) of 1.35 for; air hole diameter d=0.6 µm , and Λ=0.9 µm.

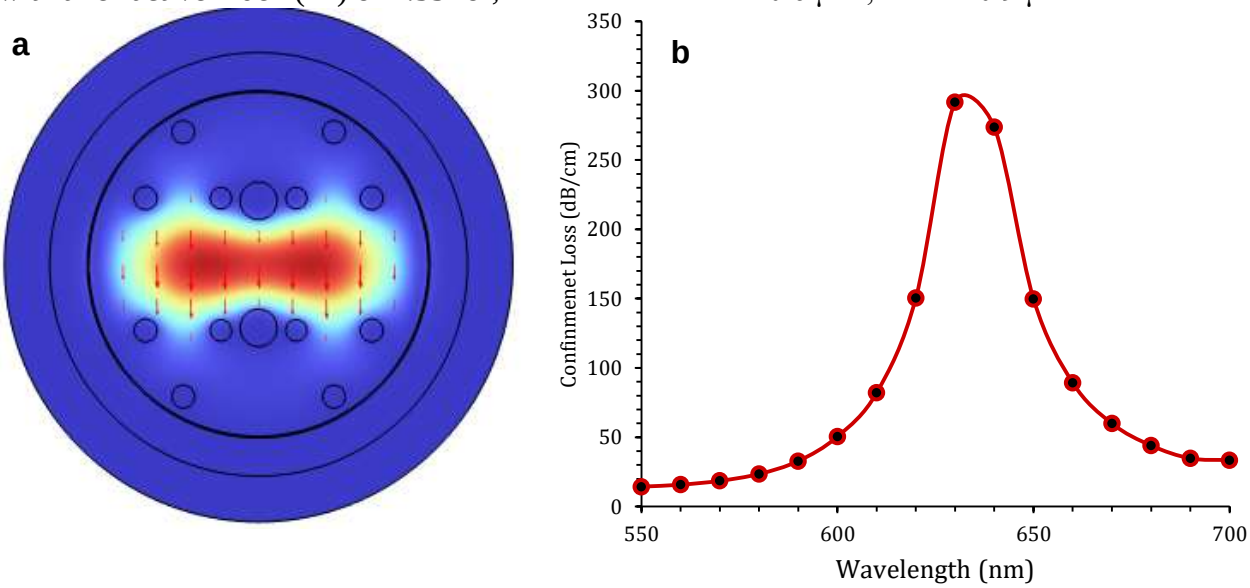

Figure (3.15 a). display the field distribution for Y-polarized light **b** Confinement loss variation with a refractive index (RI) of 1.35 for; air hole diameter d=0.3 µm , and Λ=0.9 µm.

3.2.3 "Optimization the thickness of the gold (tg)"

The thickness of the gold plasmonic layer is a critical parameter for sensor performance, as it directly governs the excitation of the surface plasmon polariton

(SPP) mode. Figures **(3.16a), (3.17a), (3.18a)** and **(3.19a)** show the effectiveness of the thickness of the metal layer to generate surface plasmon resonance effect. **Figures (3.16b), (3.17b), (3.18b) and (3.19b)** show presents the confinement loss (CL) spectra for gold layers of 20, 40, 60, and 80 nm, obtained using a fixed core diameter of 0.3 μm, pitch of 0.9 μm, and analyte refractive index of 1.35. The corresponding resonance peaks exhibit CL values of 227.18 dB/cm (20 nm), **291.7 dB/cm (40 nm)**, 79.9 dB/cm (60 nm), and 26.44 dB/cm (80 nm).

The surface plasmon wave (SPW) propagation constant, which is defined by, quantitatively describes the resonance phenomena. [87]:

$$k_{sp} = \frac{\omega}{c}\sqrt{\frac{\varepsilon_G {n_{SiO_2}}^2}{\varepsilon_G + {n_{SiO_2}}^2}} \tag{43}$$

where ε_G the dielectric constant of gold ($\varepsilon_G = \varepsilon_{G(real)} + i\varepsilon_{G(imag,)}$) and $n_{SiO_2}$the refractive index of SiO_2. Surface plasmon polaritons are excited when the condition $\varepsilon_{G(real)} < -{n_{SiO_2}}^2$ is satisfied, enabling efficient energy transfer to free electrons and generating the observed loss peaks. The sensor operates by detecting shifts in this resonance condition.

Figure 4 analysis reveals non-monotonic confinement loss with gold thickness Initial loss increase from 20 nm to 40 nm follows by significant decrease at 60 nm and 80 nm, we attribute this to increasing metal thickness reducing evanescent field penetration depth, thereby weakening analyte overlap and diminishing confinement loss. Among tested values, we selected 40 nm gold layer as optimum thickness, providing best compromise between sharp resonance peak and high loss sensitivity.

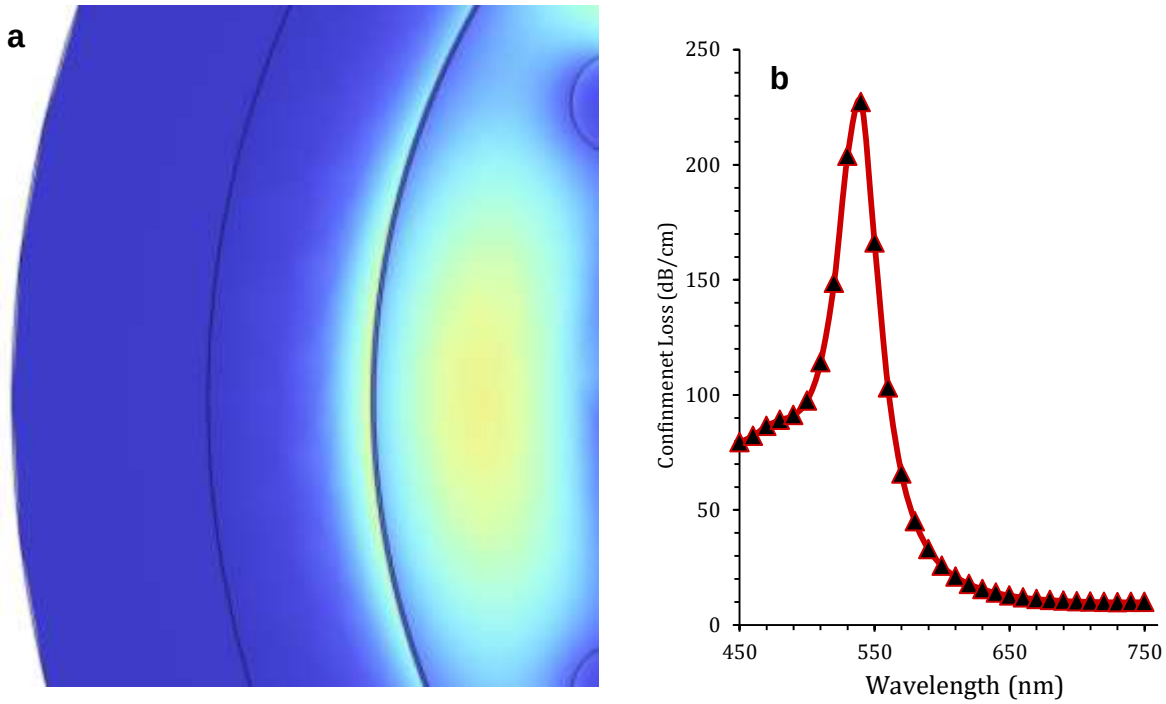

Figure (3.16) Effect of gold layer thickness on **a.** surface plasmon resonance effect **b.** the loss spectra at d =0.3 μm, Λ =0.9 μm, RI = 1.35 and tg=20 nm

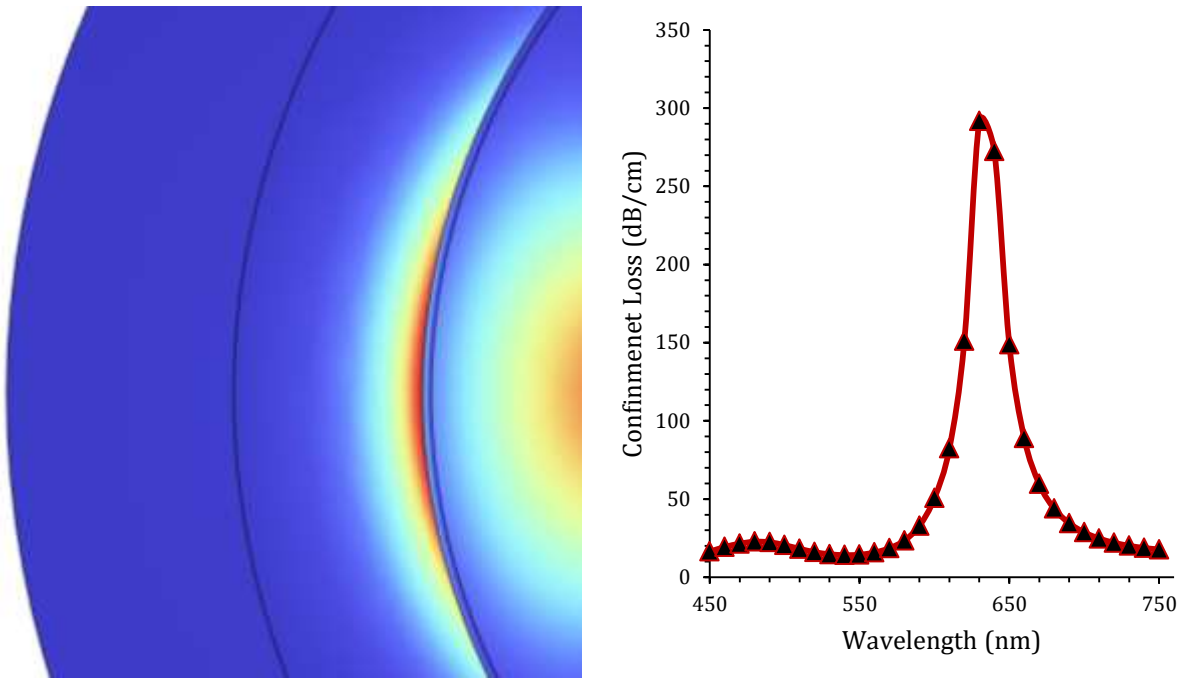

Figure (3.17) Effect of gold layer thickness on **a.** surface plasmon resonance effect **b.** the loss spectra at d =0.3 μm, Λ =0.9 μm, RI = 1.35 and tg=40 nm

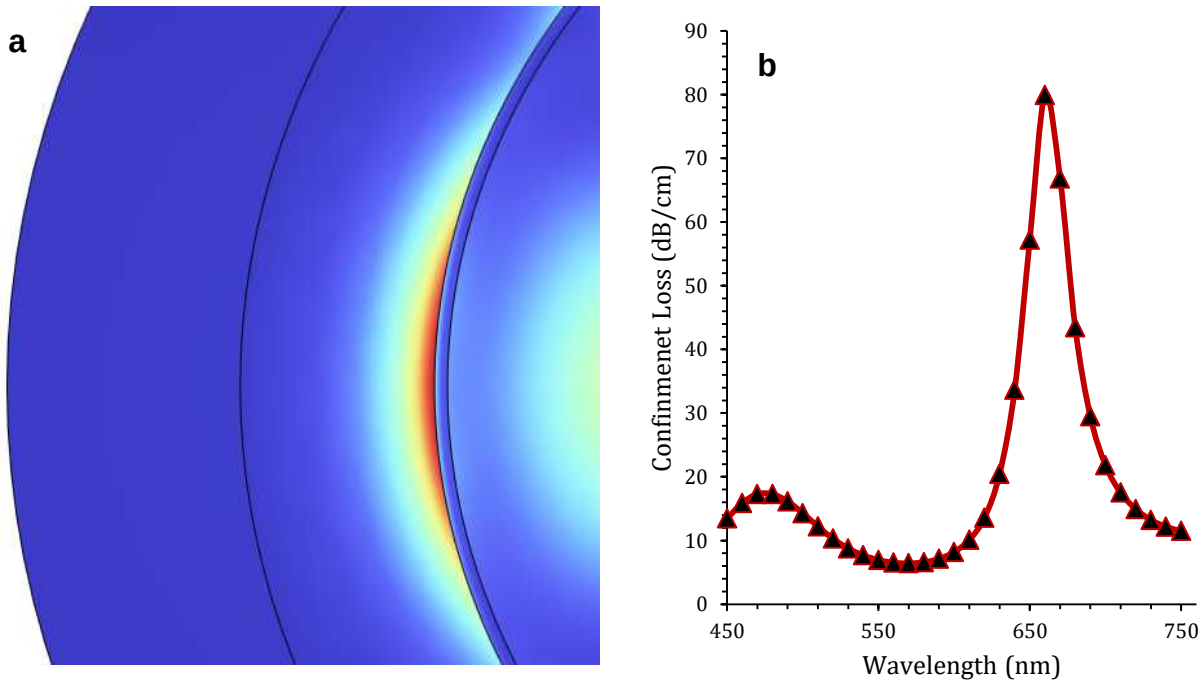

Figure (3.18) Effect of gold layer thickness on **a.** surface plasmon resonance effect **b.** the loss spectra at d =0.3 μm, Λ =0.9 μm, RI = 1.35 and tg=60 nm

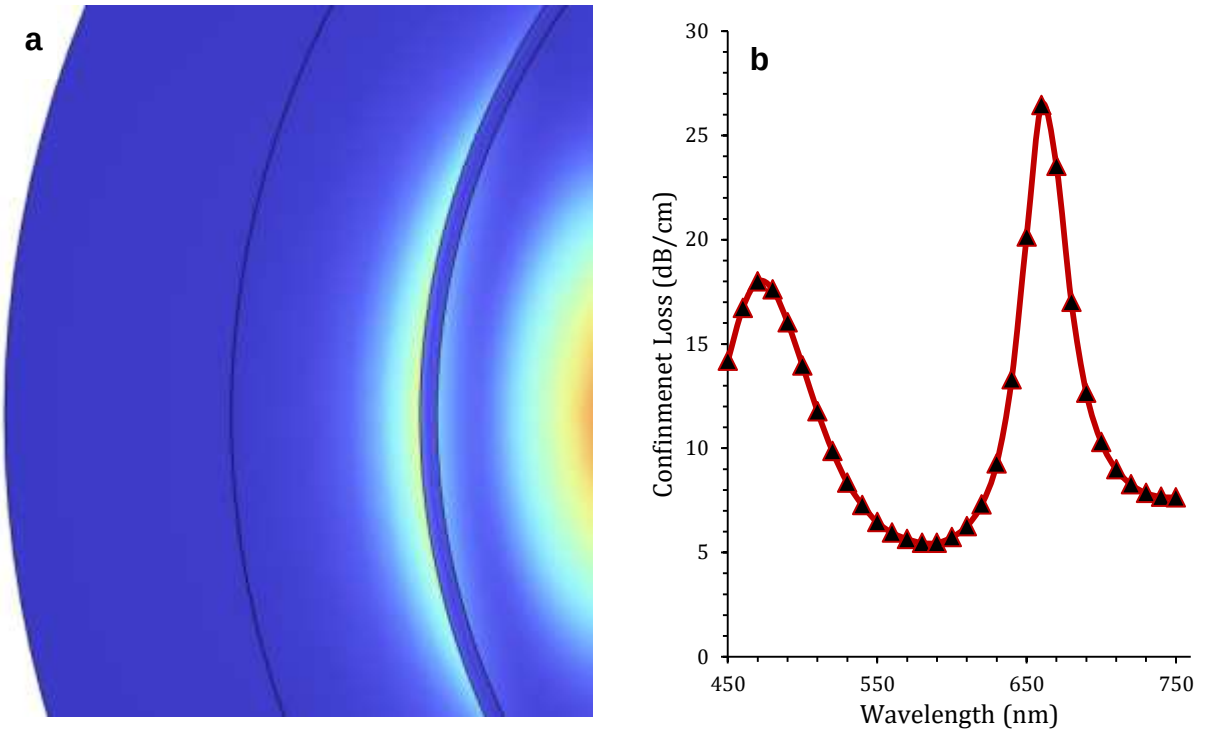

Figure (3.19) Effect of gold layer thickness on **a.** surface plasmon resonance effect **b.** the loss spectra at d =0.3 μm, Λ =0.9 μm, RI = 1.35 and tg=80 nm

3.3 Performance Characteristics of the Biosensor

Amplitude sensitivity is a key performance metric for biosensors. It is derived from the sensor's power loss spectrum at a specific wavelength in relation to the refractive index (RI) of the analyte. The amplitude sensitivity (S_A) is given by the following equation [83]:

$$S_A\left[RIU^{-1}\right] = \frac{1}{\alpha(\lambda, n_a)}\left(\frac{\partial\alpha(\lambda, n_a)}{\partial n_a}\right) \quad (44)$$

Here, $\partial\alpha(\lambda,n_a)$is the change in confinement loss, and $\alpha(\lambda,n_a)$ is the confinement loss at a specific wavelength for an analyte RI of n_a.

Fig. (3.20a) displays the amplitude sensitivity of the proposed sensor for various analyte RIs. The peak S_A increases gradually as the RI rises from 1.32 to 1.39, reaching a maximum value of 96.29 RIU^{-1} for an RI change from 1.37 to 1.38.

Conversely, a further increase in RI from 1.38 to 1.39 causes the peak S_A to decrease to 92.6 RIU^{-1}. The S_A values for other analytes are provided in Table 2. A polynomial fitting of the resonance wavelengths for analyte RIs ranging from 1.32 to 1.4 is presented in Fig. **(3.20b)**.

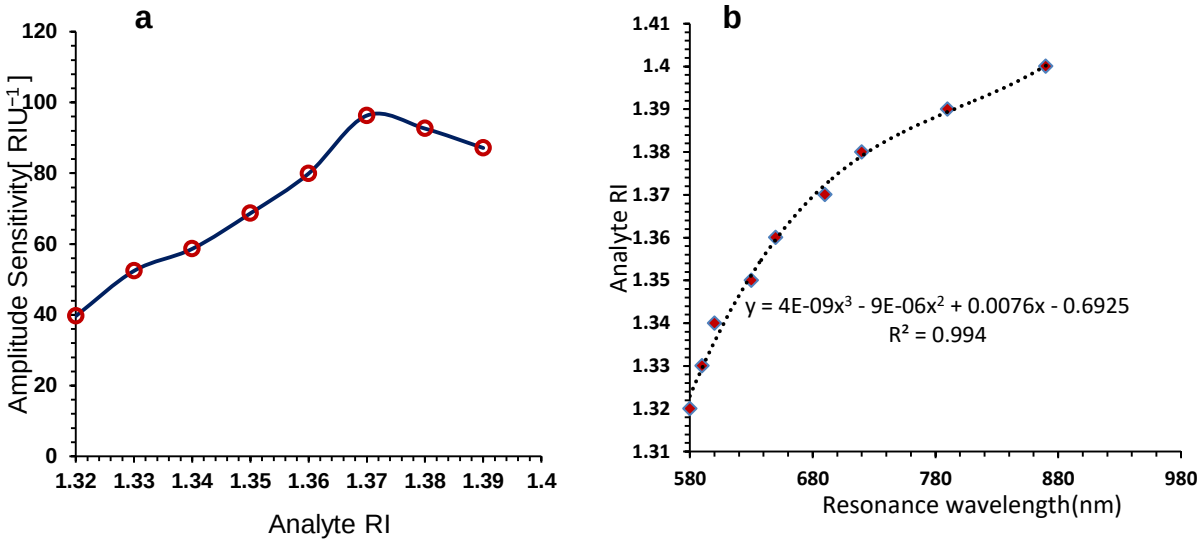

Figure (3.20) a. Amplitude sensitivity for analyte RIs from 1.32 to 1.39. **b.** Polynomial fit of resonance wavelengths versus refractive index change.

The sensor's wavelength sensitivity (S_λ) was calculated using the expression: [83]

$$S_\lambda[nm/RIU] = \frac{\Delta\lambda_{peak}}{\Delta n_a} \quad (45)$$

$\Delta\lambda_{peak}$ is the shift in "resonance wavelength" resulting from a change in (Δn_a).

As depicted in Fig. (3.21a), S_λ exhibits a non-linear relationship with the analyte RI. After an oscillatory trend between RI values of 1.33 and 1.37, the sensitivity increases markedly from approximately 3,000 nm/RIU to 8,000 nm/RIU as the RI rises from 1.37 to 1.40. This great sensitivity shows that the sensor can pick up on even the smallest changes in refractive index.

One of the parameters is the wavelength resolution (R_λ) which is the minimum detectable change in RI. It is calculated as: [88]

$$R_\lambda[RIU] = \frac{n\Delta_a \times \Delta\lambda_{min}}{\Delta\lambda_{peak}} \quad (46)$$

For this calculation, $\Delta n_a = 0.01$ and the minimum spectral resolution $\Delta\lambda_{min}$ is 0.1 nm. The resolution sharpens (decreases) at higher RIs, achieving an optimal value of 1.2×10^{-6} RIU for the change from 1.39 to 1.40, corresponding to the peak wavelength sensitivity of 8,000 nm/RIU as shown in Fig. (3.21a).

The Figure of Merit (FOM), which evaluates the overall sensor performance, It can be expressed as the wavelength sensitivity divided by the resonance peak's full width at half maximum (FWHM): [83]

$$FOM\left[\mathrm{RIU}^{-1}\right] = \frac{S_\lambda}{\mathrm{FWHM}} \quad (47)$$

Figure **(3.21b)** illustrates the relationship between FWHM and FOM across a range of analyte RIs. As summarized in Table 2, the sensor achieves a maximum FOM of 291.6 RIU^{-1} at an RI of 1.38, while the broadest resonance (FWHM = 29 nm) occurs at an RI of 1.39. A narrower (FWHM=24) at an RI of 1.36, signifying superior sensor performance.

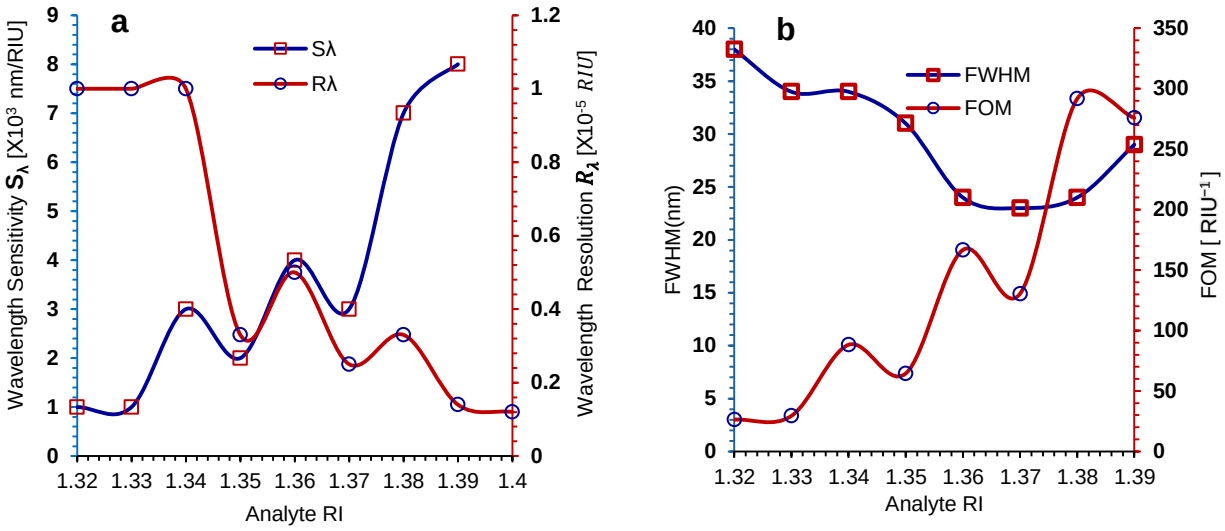

Figure (3.21) a Wavelength sensitivity and resolution for analyte RIs from 1.32 to 1.39. **b** FWHM and FOM as a function of analyte RI.

The sensor's performance is further characterized by its Signal-to-Noise Ratio (SNR) and Detection Limit (DL) are shown in Fig. **(3.22)**. The SNR is defined as [89]:

$$SNR[dB] = \frac{\Delta\lambda_{\text{peak}}}{\text{FWHM}} \tag{48}$$

An inverse correlation exists between FWHM and SNR; a narrow resonance (low FWHM) results in a higher SNR, with a maximum value of 2.75 dB achieved in this design.

The Detection Limit (DL), representing the smallest detectable change in analyte concentration or refractive index, is calculated as [89]:

$$DL[\text{nm}] = \frac{2 \times \text{FWHM}}{3 \times (SNR)^{\frac{1}{4}}} \tag{49}$$

Consequently, the DL varies with the analyte RI. The proposed biosensor has a minimum detection limit of 12.2 at RI of 1.38 and a maximum of 35.4 at RI of 1.32.

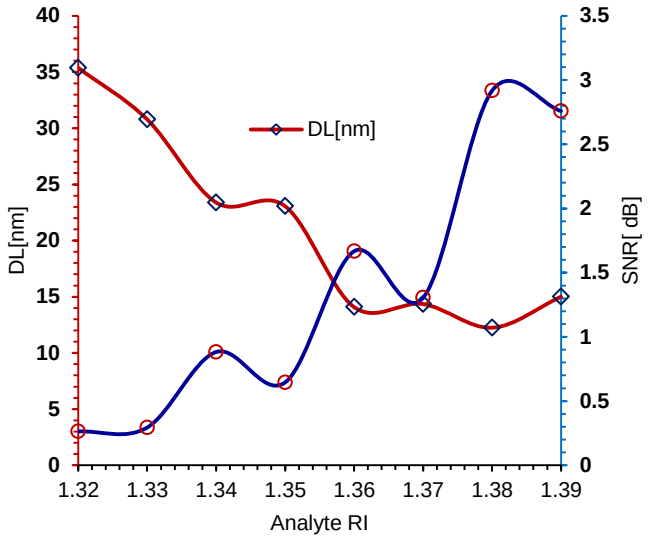

Figure (3.22) Analyte RIs range from 1.32 to 1.39 in terms of signal-to-noise ratio (SNR) and detection limit (DL).

Table 2: Performance parameters of the proposed biosensor for various analyte refractive indices.

RI	λ_r (nm)	S_λ (nm/RIU)	R_λ (RIU)	SA (RIU^{-1})	FWHM (nm)	FOM (RIU^{-1})	SNR (dB)	DL (nm)
1.32	580	1000	1.00×10^{-4}	39.6	38	26.3	0.260	35.4
1.33	590	1000	1.00×10^{-4}	52.4	34	29.4	0.290	30.8
1.34	600	3000	3.33×10^{-5}	58.6	34	88.2	0.880	23.4
1.35	630	2000	5.00×10^{-5}	68.7	31	64.5	0.645	23.1
1.36	650	4000	2.50×10^{-5}	79.9	24	166.7	1.670	14.1
1.37	690	3000	3.33×10^{-5}	96.3	23	130.4	1.300	14.3
1.38	720	7000	1.43×10^{-5}	92.6	24	291.7	2.900	12.2
1.39	790	8000	1.25×10^{-5}	87.1	29	275.9	2.758	15.0
1.40	870	-	-	-	-	-	-	-

3.4 Comparison of silver and gold plasmonic response

3.4 .1.Comparison of silver and gold the confinement loss spectrum

In this section we compare the confinement loss spectrum of sensors with silver and gold coating. Our study is founded on one significant performance parameter; sensor confinement loss spectrum. Such analysis only reveals the extent of loss of

light intensity that occurs as the light crosses through the metallic surface of the sensor. A higher confinement loss and a narrow FWHM would mean a more efficient sensor. Comparing this spectrum of gold and silver in different conditions we are able to determine which material yields a more favorable measurement on high sensitivity. **Figures (3.23 a-b), (3.24 a-b), (3.25 a-b), (3.26a) and (3.27)** reveal that silver has a higher, sharper, narrower and lower wavelength confinement loss peak. Gold on the contrary tends to have a slightly lower and broader peak. This behavior can be explained by considering the complex dielectric function, $\varepsilon(\omega) = \varepsilon_1(\omega) + i\varepsilon_2(\omega)$. **Figure 3.26 (b)** shows a different behavior compares with **Figures (3.23 a-b)- (3.27)** the resonance wavelength does not change. Instead, loss spectra of silver and gold coincide at a refractive index of 1.39. the reason for this behavior is that at Re(neff)=1.39 lead to the phase matching point will be identical for silver and gold. The imaginary part, ε_2, represents optical losses (absorption). A larger ε_2 leads to greater damping of the Surface Plasmon Polariton (SPP). This damping broadens the resonance peak in the spectrum larger the resonance linewidth (FWHM). Gold has a significantly larger ε_2 than silver in the visible and near-infrared regions, primarily due to interband transitions (electrons moving from the filled d-bands to the conduction sp-band). This is the primary reason for gold's broader resonance peak and the secondary reason is the design and distribution of the air holes PCF.

The shift of the confinement loss peak for Silver to short wavelength, this is because the real part, ε_1, determines the plasma frequency and thus the resonant wavelength. The more negative ε_1 is, the shorter the resonant wavelength for a given geometry. Silver has a more negative ε_1 than gold in the visible range, which is why its resonance is typically at a shorter wavelength for an identical structure.

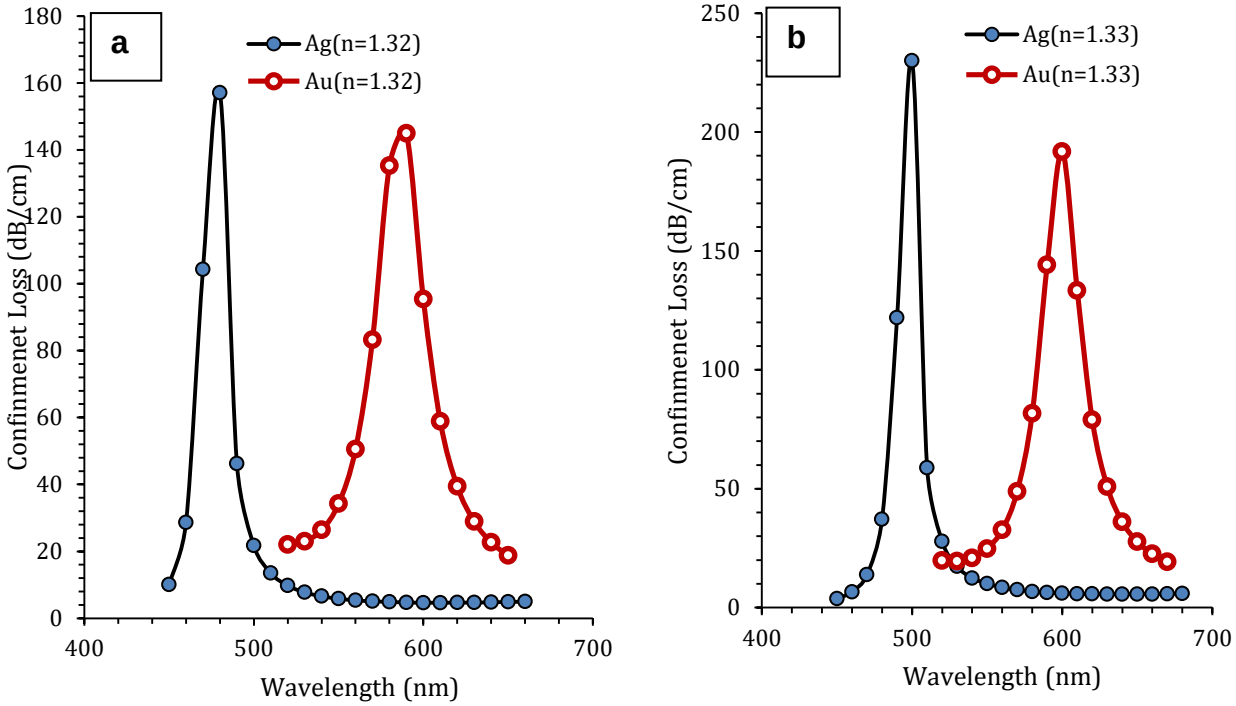

Figure (3.23)1 Comparison of silver and gold Sensor confinement loss spectrum at (**a**)RI=1.32, (**b**)RI=1.33,

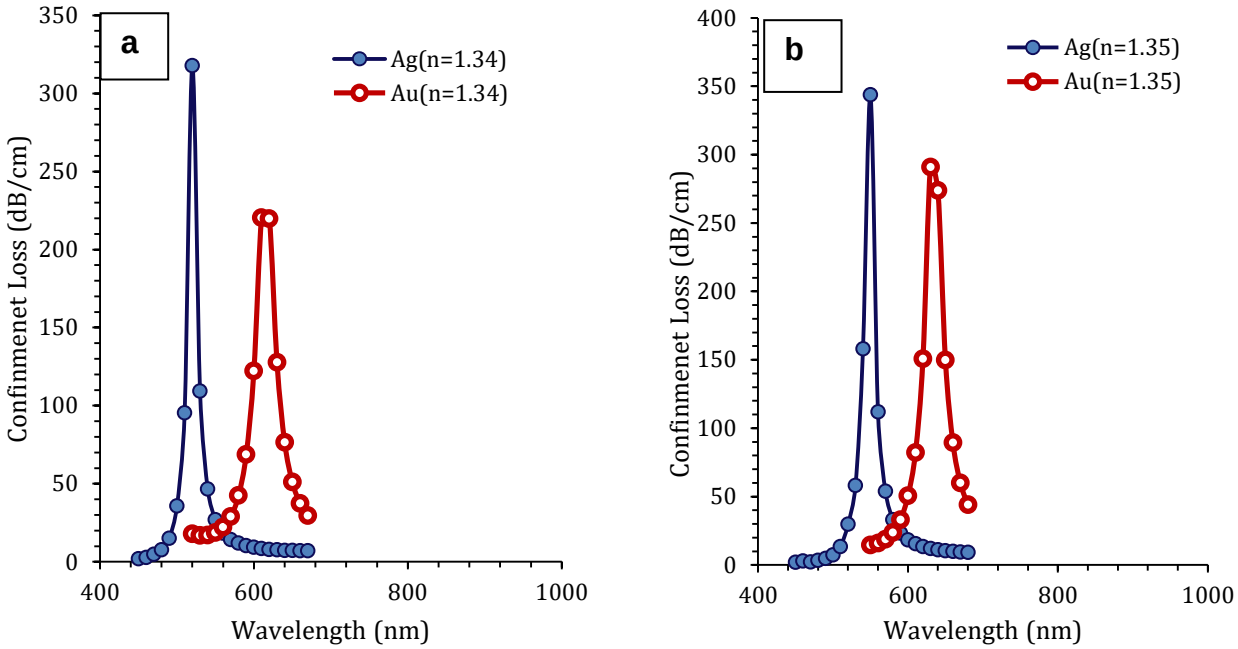

Figure (3.24) Comparison of silver and gold Sensor confinement loss spectrum at (**a**)RI=1.34, (**b**)RI=1.35

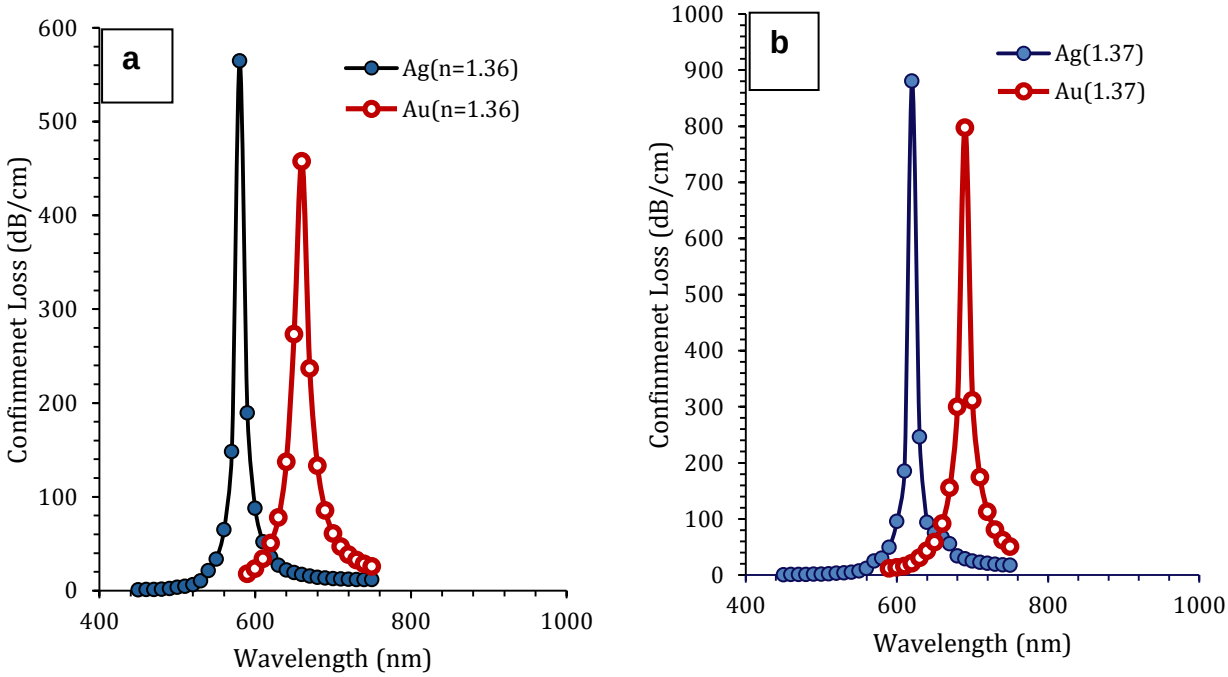

Figure (3.25) Comparison of silver and gold Sensor confinement loss spectrum at (**a**) RI=1.36, (**b**) RI=1.37

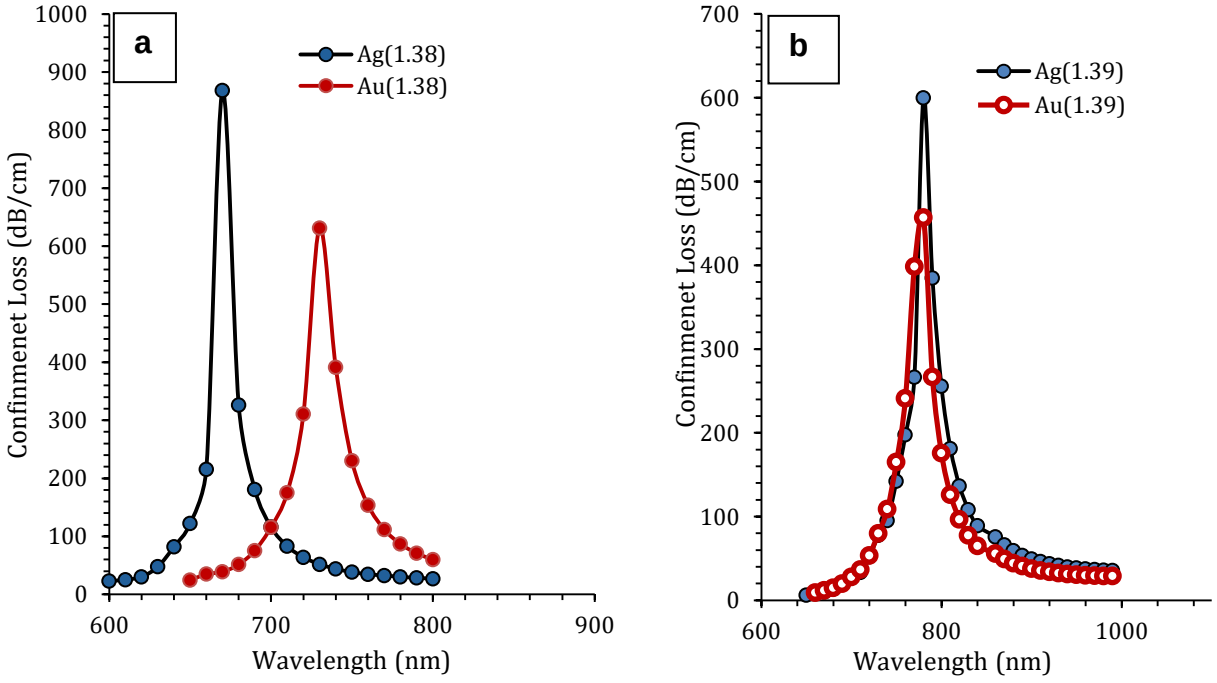

Figure (3.26) Comparison of silver and gold Sensor confinement loss spectrum at (**a**) RI=1.38, (**b**) RI=1.39

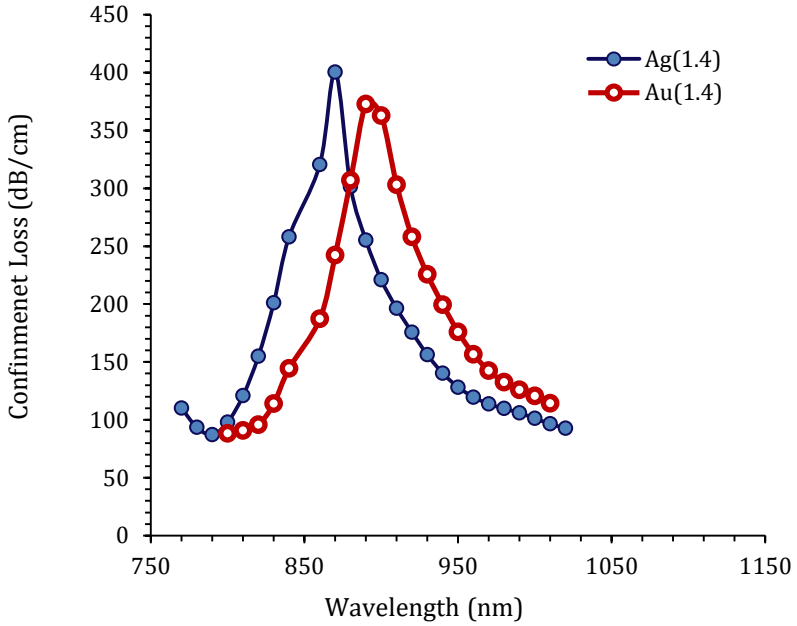

Figure (3.27) Comparison of silver and gold Sensor confinement loss spectrum at RI=1.4

3.4 .2. A comparison of Amplitude Sensitivity in silver and gold

The sharpness of plasmonic sensor resonance peak determines the amplitude sensitivity of the sensor. Silver tends to have better amplitude sensitivity than gold because it has more distinct and sharp resonance behavior.

According to **Equation 44**, the variations on the refractive index of the analyte. that are one minute will make a huge difference in the signal loss $\partial\alpha(\lambda, n_a)$ at a given wavelength. This huge shift in loss is directly proportional to an increased calculated amplitude sensitivity (S_A). While Gold's Performance: The slope of this larger peak is less steep. This therefore means that a shift in the refractive index of the analyte will cause a reduced change in the signal loss $\partial\alpha(\lambda, n_a)$ at a certain

wavelength. This reduced response results to reduced calculated amplitude sensitivity.

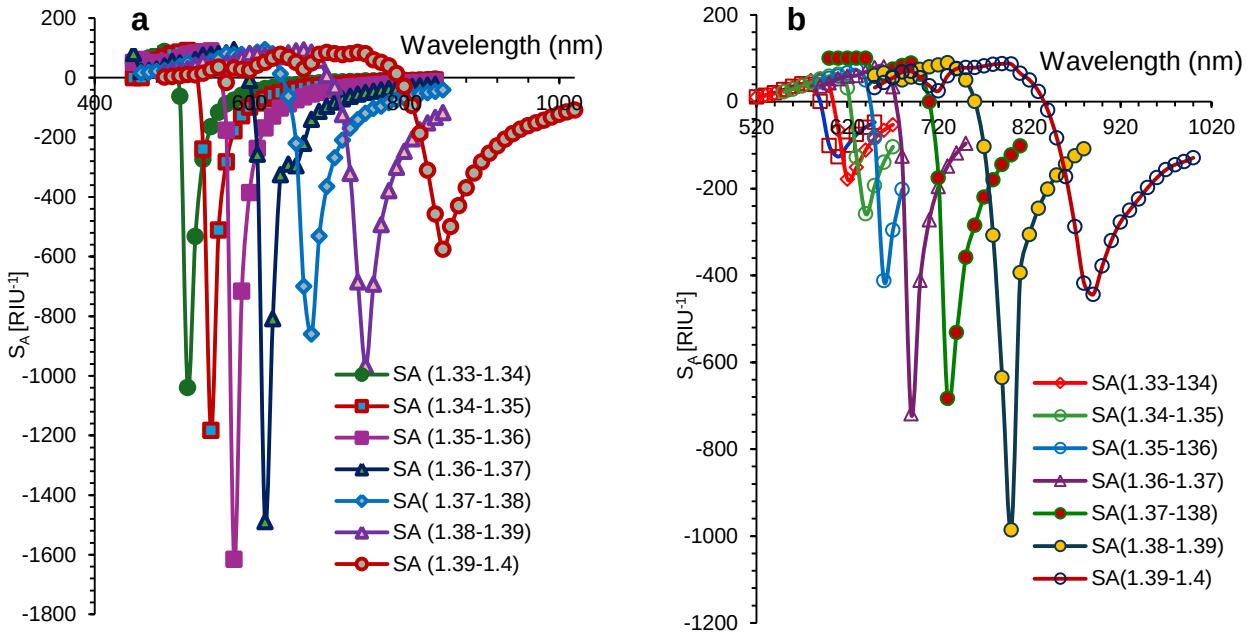

Figure (3.28) Amplitude Sensitivity (S_A)(**a**)Silver plasmonic material (**b**)Gold plasmonic material.

Chapter Four

Results and Discussions

4.Results and Discussion

The sensor's performance was evaluated by measuring the confinement loss across analyte refractive indices from 1.32 to 1.40, as shown in Fig. **(3.29)** a. The analysis shows a strong positive correlation, with the resonant wavelength changing significantly as the refractive index increases. The resonant peak, a direct indicator of the sensor's high sensitivity to refractive index variations, changes by 310 nm within this range, from 590 nm to 900 nm. The peak amplitude of the containment loss also shows a clear trend, rising monotonously with the refractive index from 1.32 to 1.39. However, at a refractive index of 1.39, the amplitude begins to decrease. As shown in Figure 8a, the refractive index reaches a maximum of 1.40, and a significant drop in peak amplitude occurs, with the full width increasing at half the maximum (FWHM). This suggests a possible decrease in detection accuracy or a deviation from the optimal coupling efficiency at the upper limit of the sensor's dynamic range. As seen in Fig. **(3.29)** b, the amplitude sensitivity (S_A) was determined across this RI spectrum. The sensitivity was evaluated for certain intervals at a resonance wavelength of 800 nm. The sensitivity is 126. 6 RIU^{-1} for a shift in RI from 1. 32 to 1. 33. This value rises significantly to 985. 58 RIU^{-1} for a variation in RI. from 1. 38 to 1.39, Highlighting the sensor's outstanding ability to detect minute changes in the refractive index. The amplitude sensitivity decreases dramatically to 443. 7 RIU^{-1} When the refractive index is increased to 1.40, this indicates a nonlinear response system at a higher refractive index.

The sensor's versatility is demonstrated by its ability to respond to a wide range of important vital signs. For example, the refractive index of normal human serum ranges between 1.38 and 1.41. [89], while malignant cells like MCF-7 have a higher RI. of about 1. 40 [90,91], which suggests a shift in metabolism. The sensor

can successfully identify a wide range of compounds including chemicals like ethanol and acetone (RI ~1. 36 [92]), milk (RI 1. 35–1. 38 [93]) and basic. Its ability to detect a wide range of chemical and biological markers based on RI changes makes this method very promising for use in biomedical diagnostics, food safety, and environmental monitoring.

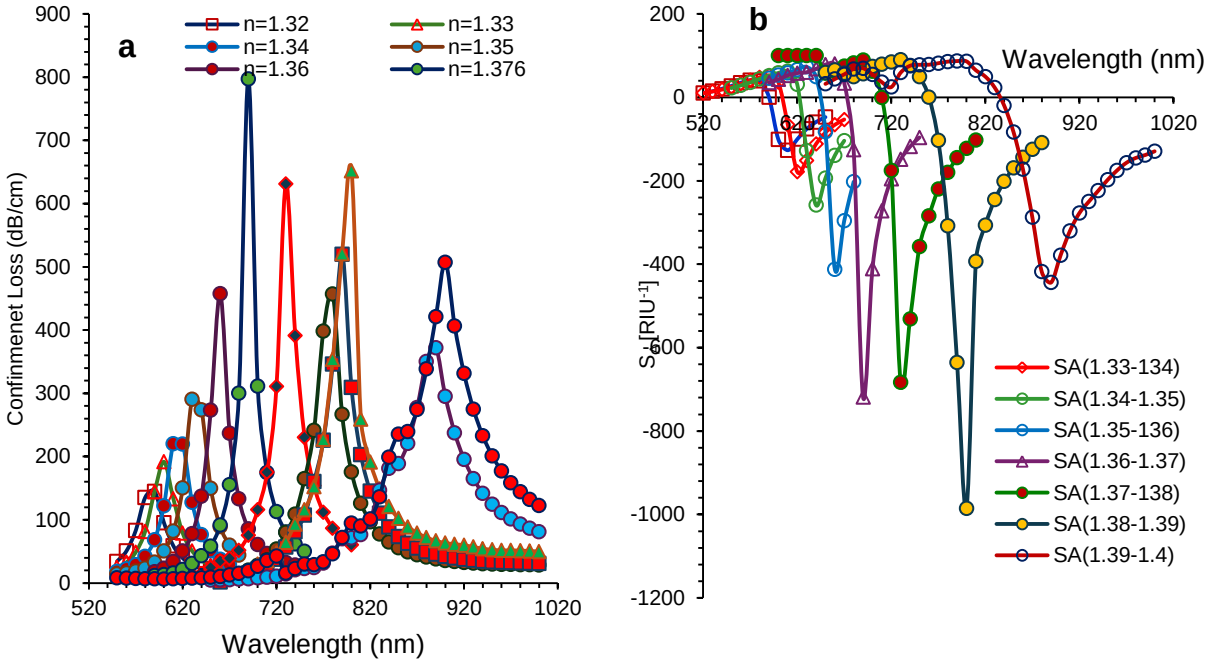

Fig. (3.29) a. an Analyte RIs with Confinement Loss spectra between 1.32 and 1.42; **b.** Amplitude Sensitivity (SA) between 1.32 and 1.4.

Paramount application involves disease detection, where typically stable blood RI becomes altered by pathogen or malignant cell presence. As Table 3 quantifies, this biosensor design effectively discriminates between healthy and diseased cells by exploiting these specific refractive index differences.

Table 3. Refractive index values for normal and malignant cells.

Type	**Normal cells (RI)**	**Malignant cells (RI)**	**Refs**
Hela (cervical cancer)	1.368	1.392	[94]
Jurkat (blood cancer)	1.376	1.39	[95]
PC12 (adrenal glands cancer)	1.381	1.395	[95]
MDA-MB-231 (breast cancer type 1)	1.385	1.399	[95]
MCF-7	1.387	1.401	[91,94]
Type	**Normal Cell**	**HIV infected**	**Ref.**
Human immunodeficiency virus	1.35	1.42	[95]
Type	**Conc. 0%**	**Conce. 40%**	**Ref.**
Glucose solution	1.33	1.4	[96]

We first demonstrated sensor functionality through HeLa cell detection shown in Fig. **(3.30)** a. Clear distinction observes between states: normal HeLa cells (RI = 1.368) and malignant ones (RI = 1.392). This difference manifests optically as redshift in resonance wavelength for maximum loss from 660 nm to 880 nm. This 220 nm shift represents critical high sensitivity indicator, quantified by wavelength sensitivity 7,333 nm/RIU and amplitude sensitivity 1942.79 RIU^{-1} shown in Fig. **(3.30)** b.

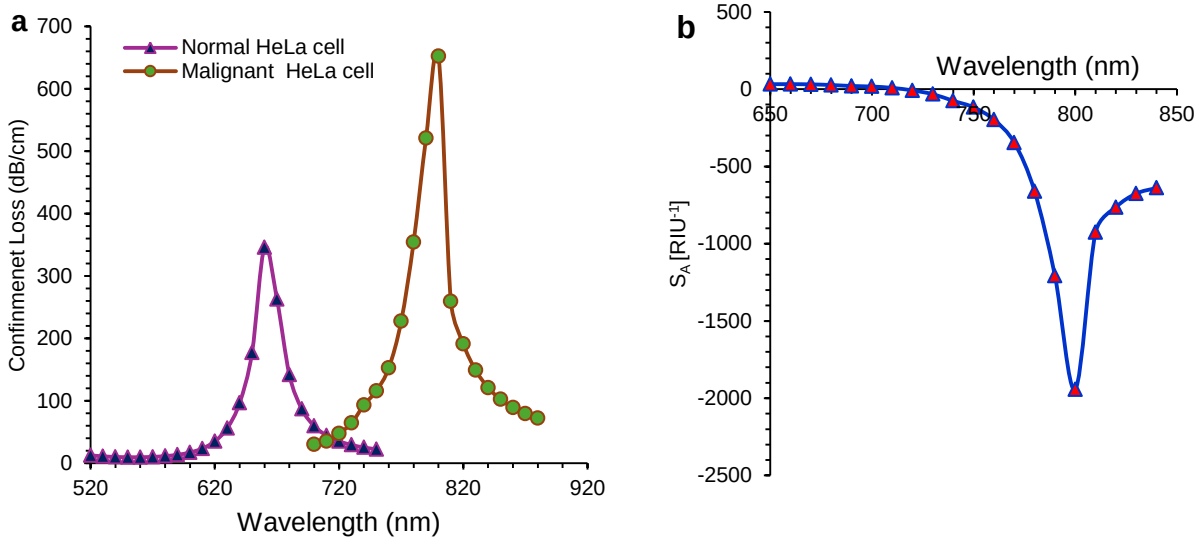

Fig. (3.30) a Sensor confinement loss spectrum for HeLa cells; **b** Amplitude sensitivity for HeLa cells.

We further validated sensor performance with Jurkat cells shown in Fig. **(3.31)** a. Malignant Jurkat cell (RI = 1.39) induces shift to 800 nm from 690 nm resonance of healthy cell (RI = 1.376). This 110 nm shift corresponds to wavelength sensitivity 5500 nm/RIU. We also recorded amplitude sensitivity 1157.63 RIU^{-1} shown in Fig. **(3.31)** b.

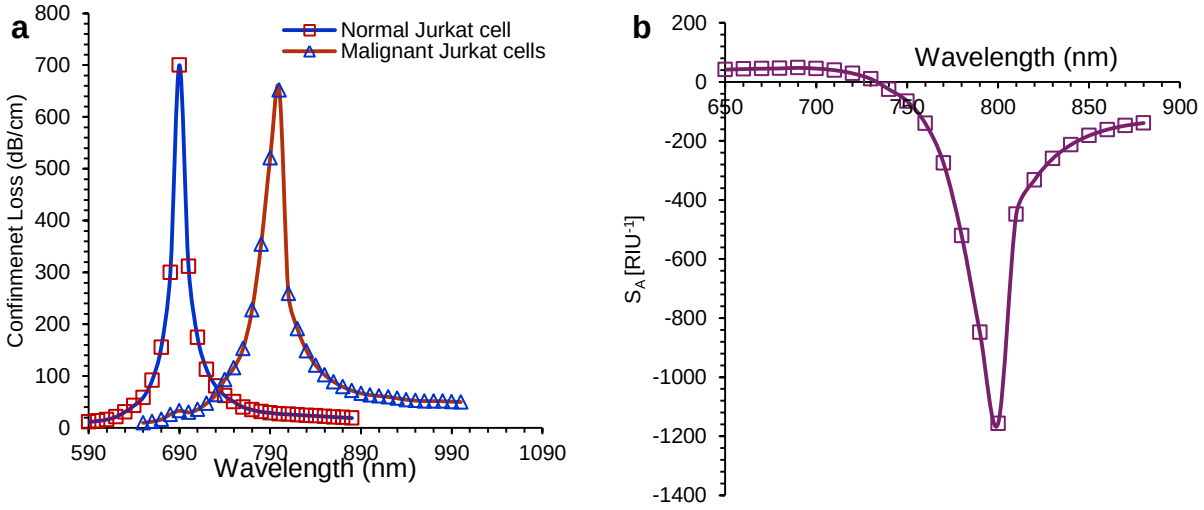

Fig. (3.31) a Sensor confinement loss spectrum for Jurkat cells; **b** Amplitude sensitivity for Jurkat cells.

For PC12 cells, sensor similarly distinguishes between normal (RI = 1.381, λ_r = 730 nm) and malignant (RI = 1.395, λ_r = 800 nm) states shown in Fig. **(3.32)** a. The 70 nm shift corresponds to wavelength sensitivity 5,000 nm/RIU, complemented by amplitude sensitivity 985.58 RIU^{-1} shown in Fig. **(3.32)** b.

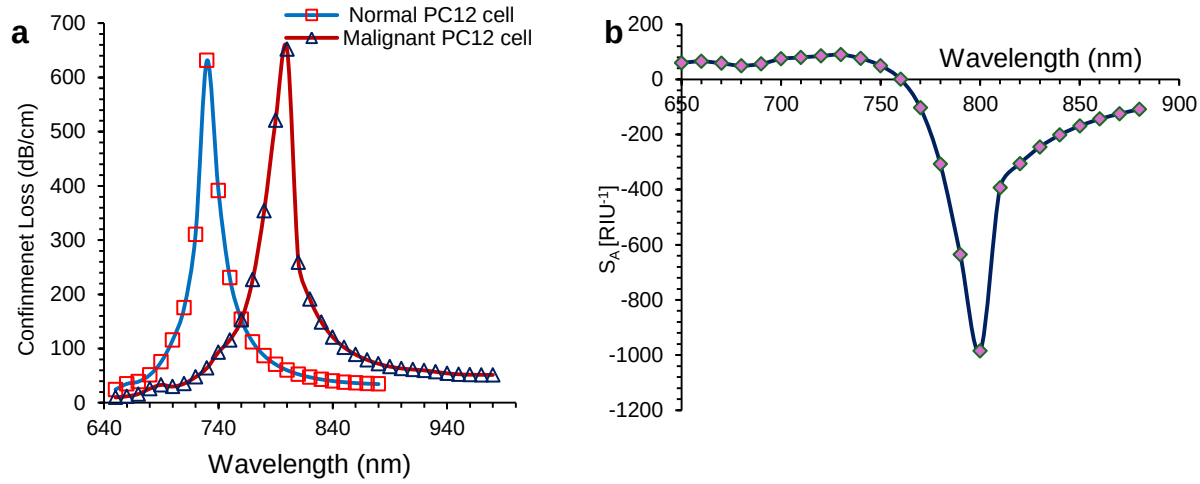

Fig. (3.32) a Sensor confinement loss spectrum for PC12 cells; **b** Amplitude sensitivity for PC12 cells.

MDA-MB-231 cell analysis revealed one of most significant shifts shown in Fig. **(3.33)** a. Resonance shifted from 770 nm (normal, RI=1.385) to 890 nm (malignant, RI=1.399)— 120 nm shift yielding high wavelength sensitivity (S_λ) 8,571 nm/RIU. Amplitude sensitivity (S_A) was 672.63 RIU^{-1} shown in Fig. **(3.33)** b. Furthermore, this configuration achieved optimal resolution 1.16×10^{-5} RIU, highlighting its good precision.

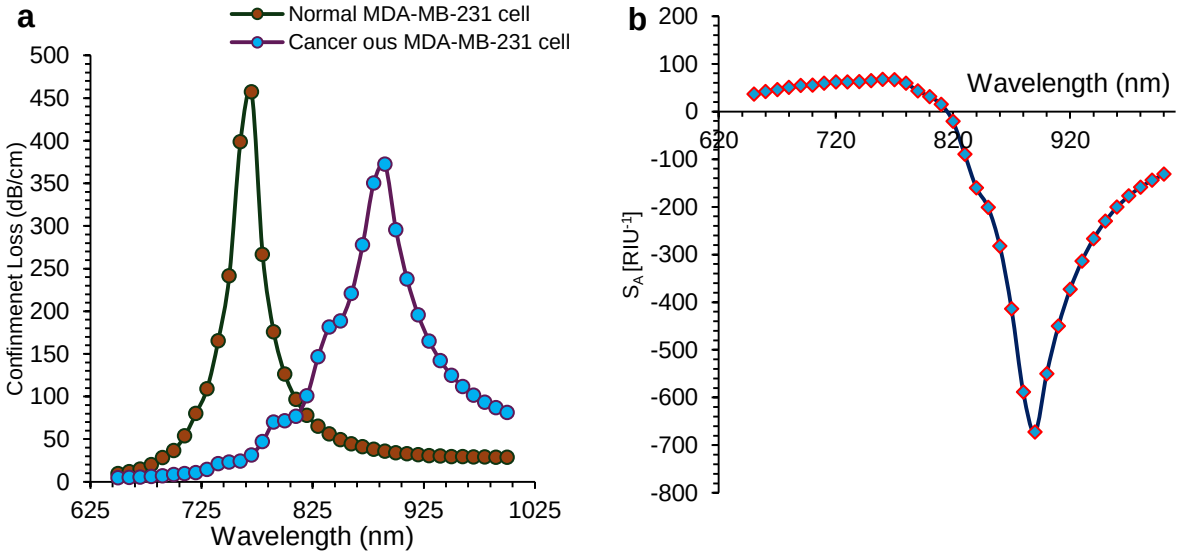

Fig. (3.33) a Sensor confinement loss spectrum for MDA-MB-231 cells; **b** Amplitude sensitivity for MDA-MB-231 cells.

Sensor performance for MCF-7 cells shown in Fig. **(3.34)** a. Resonant wavelength shifted from 780 nm (RI=1.387) to 880 nm (RI=1.401), 100 nm shift corresponding to wavelength sensitivity 7,692 nm/RIU and amplitude sensitivity 586 RIU^{-1} shown in Fig. **(3.34)** b, with resolution 1.4×10^{-5} RIU.

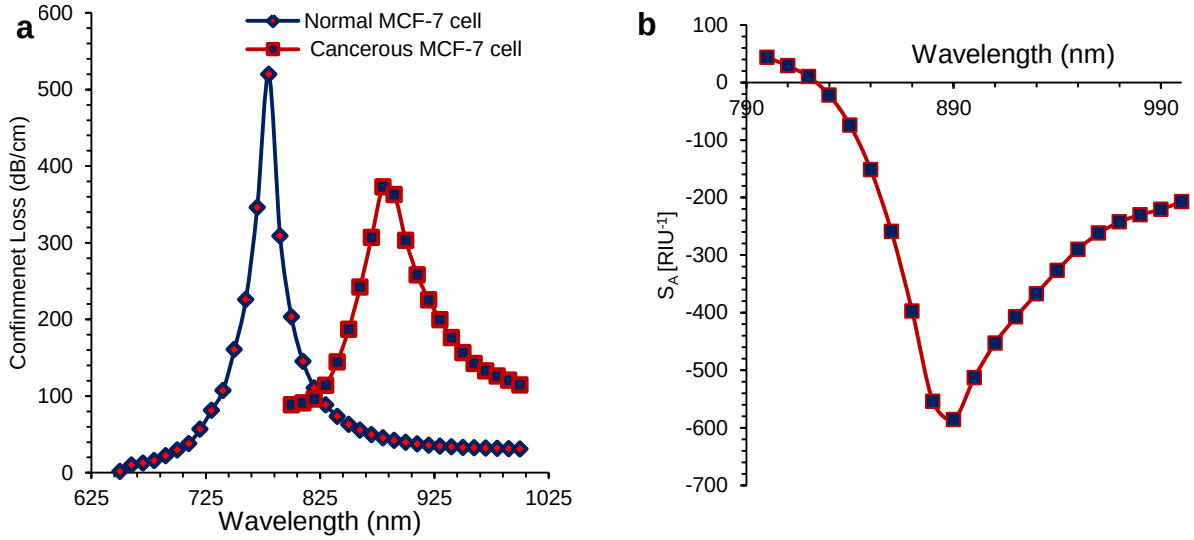

Fig. (3.34) a Sensor confinement loss spectrum for MCF-7 cells; **b** Amplitude sensitivity for MCF-7 cells.

Sensor capability extends to viral detection, as demonstrated with HIV-infected blood samples. We observed significant 270 nm shift, from 630 nm (normal blood, RI=1.35) to 900 nm (infected sample, RI=1.42) shown in Fig. **(3.35)** a. This shift corresponds to high wavelength sensitivity 3,857 nm/RIU and resolution 2.59×10^{-6} RIU. We also achieved amplitude sensitivity 804.9 RIU^{-1} shown in Fig. (3.35) b, enabling highly accurate pathogen detection.

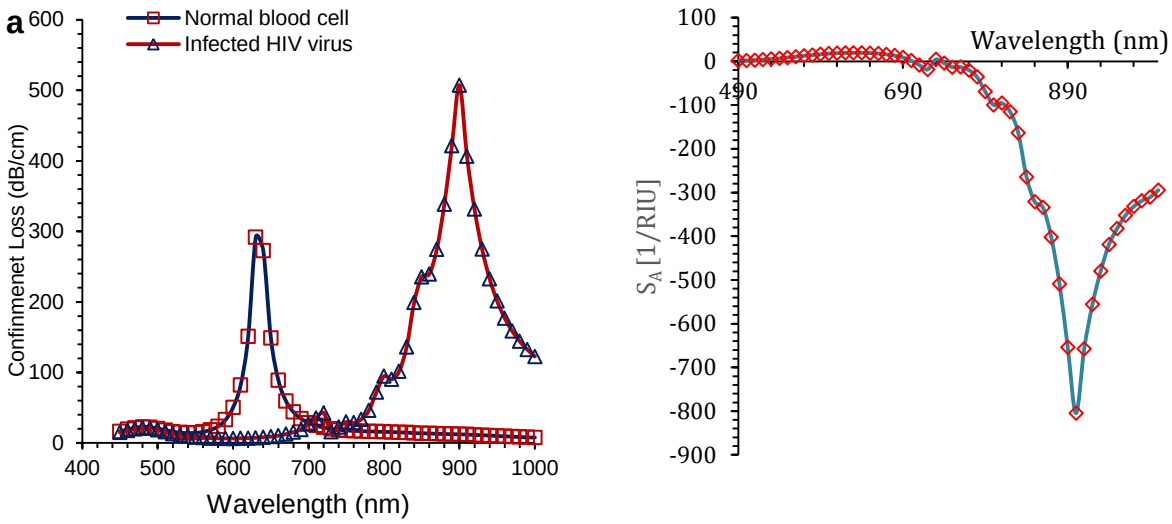

Fig. (3.35) a Sensor confinement loss spectrum for HIV-infected blood; **b** Amplitude sensitivity for HIV-infected blood.

Beyond cellular detection, sensor effectively quantified biochemical concentrations. For Glucose solution, concentration-dependent RI change from 1.33 to 1.4 induced 280 nm shift (from 600 nm to 880 nm), as shown in Fig. **(3.36)** a. This corresponds to wavelength sensitivity 4,000 nm/RIU, amplitude sensitivity 825.59 RIU^{-1} as shown in Fig. **(3.36)** b, and resolution 2.5×10^{-6} RIU these values exceed cell detection performance.

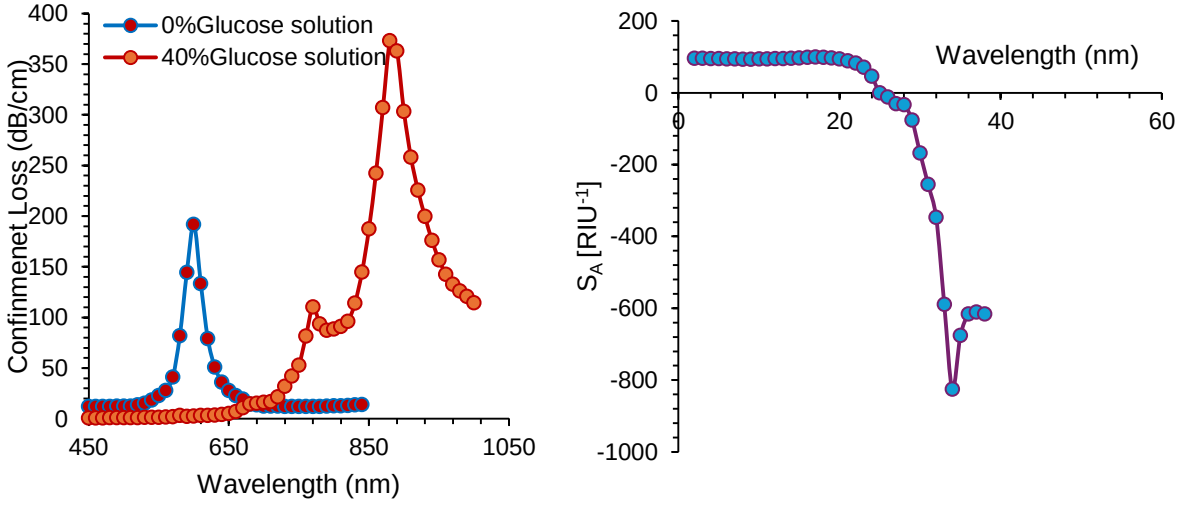

Fig. (3.36) a Sensor confinement loss spectrum for Glucose solution; (b) Amplitude sensitivity for Glucose solution.

Collectively, results demonstrate versatile, high-performance detection across diverse analytes. Sensor achieves outstanding wavelength sensitivity for MDA-MB 231 cells and HIV, while demonstrating superior amplitude sensitivity for HeLa cells as shown in Fig. **(3.37)**. Observed sensitivity reduction at RI=1.40 attributes to deviation from ideal core plasmonic mode coupling, common phenomenon near such sensors operational limit.

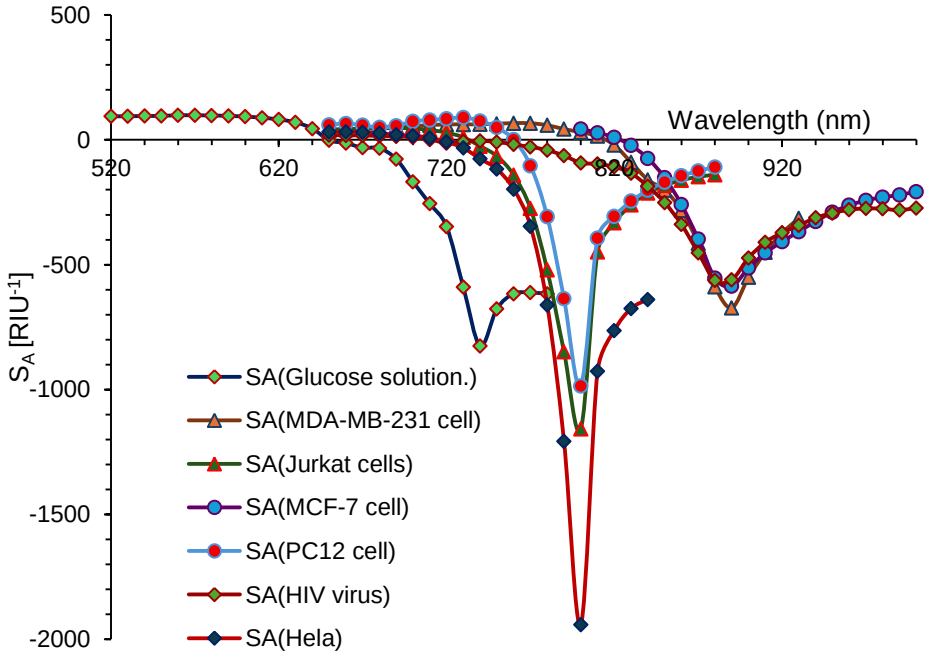

Fig. (3.37) Amplitude sensitivity for all case studies.

Combined outcomes from detecting various cell types, viruses, and biochemical samples highlight proposed biosensor impressive adaptability and high sensitivity. Although absolute sensitivity values differ based on analyte-specific RI range, sensor consistently delivers strong, measurable optical response. This versatility positions it as highly promising tool for broad sensing application spectrum. **Table 4** provides a complete comparison of the proposed PCF-SPR biosensor's performance to current state-of-the-art devices. Our sensor architecture consistently outperforms competitors across multiple cancer cell lines and key sensing parameters, according to this comparison research. The proposed sensor

greatly improves wavelength sensitivity (S_λ) compared to existing literature for most cell types.

The most striking improvement is observed in wavelength sensitivity (S_A), where the proposed sensor significantly outperforms existing literature for the majority of cell types. The Sλ values for MDA-MB-231 are 8.571 nm/RIU and for HeLa are 7.333 nm/RIU, indicating an improvement by a factor of roughly 1.8 and 2.1, correspondingly, compared to the figures documented by Ashrafian et al.[32].Similarly, for MCF-7 and Jurkat cells, our sensor demonstrates a substantial enhancement, with sensitivity values that are considerably greater than those found in prior studies [97, 98, 99]. This remarkable improvement in S_λ can be attributed to the optimized geometry of the PCF, which enhances the evanescent field overlap with the plasmonic gold layer and the analyte, thereby amplifying the resonant wavelength shift upon biomarker binding. Regarding amplitude sensitivity (S_A), the sensor demonstrates strong and highly competitive performance, although there is greater variability between different cell lines. It achieves exceptional SA values of 1,157.63 RIU^{-1} and 1,942.7 RIU^{-1} for Jurkat and HeLa cells, respectively. The sensitivity of HeLa cells indicates an increase of approximately 30% compared to the highest value previously recorded in studies [89]. While the amplitude sensitivity for other cell lines, such as MDA-MB-231 and MCF-7, is slightly lower than some documented figures, it remains within a highly competitive range, confirming the reliable performance of the sensor across various biological targets. Regarding amplitude sensitivity (S_A), the sensor exhibits strong and competitive performance, albeit with increased variability among different cell lines. It attains remarkable S_A values of 1,157.63 RIU^{-1} for Jurkat cells and 1,942.7 RIU^{-1} for HeLa cells. The sensitivity of HeLa cells demonstrates an approximate 30% enhancement relative to the highest value documented in the literature [89]. The sensor's specificity for other cell lines,

including MDA-MB-231 and MCF-7, is marginally lower than certain reported values, yet it remains within a highly competitive spectrum, affirming the sensor's dependable efficacy across diverse biological targets.

This work significantly broadens the application range of PCF-SPR sensors by creating unprecedented performance benchmarks for other essential analytes, in addition to identifying established cancer cell lines. The sensor has a high wavelength sensitivity (3,857 nm/RIU) for finding HIV-infected blood, which is a big improvement over the limited work that came before it [96]. The sensor can also detect glucose solutions with a sensitivity of 4,000 nm/RIU and a resolution of 2.5×10^{-6} RIU, which is better than previous sensor designs [102, 103]. This means it could be used for precise biochemical monitoring.

Table 4. Performance comparison between the proposed sensor and previously published models.

(Analytic (Cell Type	Parameter	[Literature [ref		Our Work
(Hela(Cervical Cancer	(nm/RIU) $_{\lambda}S$	[97]4333.3	[89]3,500	7,333
	$(^{1}RIU^{-})_{A}S$	[97]757	[89]1,481	1,942.79
	(Resolution (RIU	[97]$^{5-}10 \times 9.70$	[89]$^{5-}10 \times 1.19$	$^{5-}10 \times 1.36$
(Jurkat(Blood Cancer	(nm/RIU) $_{\lambda}S$	[98]1,428.57	[89]3,571	5,500
	$S_{A}(^{1}RIU^{-})$	[98]396.29	[89]1,057	1,157.63
	(Resolution (RIU	[98]$^{5-}10 \times 7.00$	[89]$^{5-}10 \times 2.00$	$^{6-}10 \times 9.10$
(PC12(Adrenal Cancer	(nm/RIU) $_{\lambda}S$	[98]1,428.57	[101]5,000	5,000
	$S_{A}(^{1}RIU^{-})$	[98]489.66	[101]575.34	985.58
	(Resolution (RIU	[98]$^{5-}10 \times 7.00$	[101]$^{5-}10 \times 2.00$	$^{5-}10 \times 2.00$
Breast)231-MB-MDA (Cancer	(nm/RIU) $_{\lambda}S$	[99]7,857	[89]4,785	8,571
	$S_{A}(^{1}RIU^{-})$	[99]985	[89]974.16	673
	(Resolution (RIU	[99]$^{5-}10 \times 2$	[89]$^{5-}10 \times 1.49$	$^{5-}10 \times 1.16$
(Breast Cancer)7-MCF	(nm/RIU) $_{\lambda}S$	[100]7,141	[101]6,428.6	7,692
	$S_{A}(^{1}RIU^{-})$	[100]270	[101]766.361	586
	(Resolution (RIU	[100]$^{5-}10 \times 2.9$	[101]$^{5-}10 \times 1.55$	$^{5-}10 \times 1.40$
Infected HIV	(nm/RIU) $_{\lambda}S$	[96]225	NA	3,857
	$S_{A}(^{1}RIU^{-})$	NA	NA	804.9
	(Resolution (RIU	NA	NA	$^{6-}10 \times 2.59$
Glucose solution	(nm/RIU) $_{\lambda}S$	[103]2,300	[102]2,800	4,000
	$S_{A}(^{1}RIU^{-})$	NA	NA	825.59

	(Resolution (RIU	NA	NA	$^{6-}10 \times 2.5$

Chapter Five

Conclusion

5 Conclusions

Overall, the results of this paper verify the effectiveness of the circular photonic crystal fiber (PCF) architecture in the implementation of a high-performance surface plasmon resonance (SPR) biosensor. It is designed using a gold layer because it has good plasmonic properties and has a uniform air-hole lattice in order to maximize light-matter interaction. The effectiveness of using a circular photonic crystal fiber (PCF) architecture to create high performance surface plasmon resonance (SPR) biosensors are confirmed by this work. In order to maximize light-matter interaction and create a sturdy, fabricable platform, the design makes use of homogeneous air-hole lattice and gold film, which have strong plasmonic capabilities.

Our results indicate that the optimal air hole diameter, pitch and gold layer thickness for our proposed design were 0.3 μm and 0.9 μm and 40 nm, respectively, based on peak confinement loss values, where the optimized device proved good wavelength sensitivity (S_λ). Additionally, confinement loss spectrum in silver exhibits a smaller and very sharp resonance peak than in gold. The spectrum of gold in general is red shifted and has greater loss at most wavelengths because it is more inherently absorptive. Thus, in optical performance terms, silver will offer a better loss spectrum, however this has to be weighed against its low environmental stability.

The sensor demonstrated outstanding results in the detection of various important analytes, such as HIV, biochemical substances, including glucose solutions and several cancer cell lines, (HeLa, Jurkat, PC12, MDA-MB-231, and MCF-7). The sensor showed the ability to detect even the smallest changes in refractive index through the use of spectral and amplitude interrogation techniques.

Chapter Five
Conclusions

Notably, it obtained superior wavelength sensitivity of 8,571 nm/RIU with resolution of 1.16×10^{-5} RIU for MDA-MB-231 cells (breast cancer) and record amplitude sensitivity of 1,943 RIU^{-1} and resolution 1.36×10^{-5} RIU for HeLa cells (cervical cancer). In addition, the design demonstrated great performance on Jurkat cells (blood cancer), where it reached a resolution of 9.10×10^{-6} RIU and with glucose solution where it reached 2.5×10^{-6} RIU. The sensor is capable of detecting a diverse array of needed analytes such as different cancer cell lines, the human immunodeficiency virus (HIV), as well as biochemical solutions such as glucose solution.

The sensor also showed that it could detect very small changes in the refractive index by using spectral and amplitude interrogation techniques. It set a new record for amplitude sensitivity at 1,943 RIU^{-1} and a new record for resolution at 1.36×10^{-5} RIU for HeLa cells (cervical cancer). It also set a new record for wavelength sensitivity at 8,571 nm/RIU and a new record for resolution at 1.16×10^{-5} RIU for MDA-MB-231 cells (breast cancer). The proposed biosensor marks a substantial improvement in the field of biosensors. Three key performance characteristics, namely: (1) High accuracy, which makes it potentially effective in enhancing diagnostic performance in the field of medical diagnostics and bioanalytical sciences; (2) high wavelength sensitivity, which is higher than in a few studies; and (3) high amplitude sensitivity to simple cancer cell lines have been seen.

References

1. Wang, Q., Zhang, D., Qian, Y., et al., (2024). Research on fiber optic surface plasmon resonance biosensors: a review. *Photonic Sensors* 14, 240201. https://doi.org/10.1007/s13320-024-0703-7

2. Capelli, D., Scognamiglio, V., Montanari, R., (2023). Surface plasmon resonance technology: recent advances, applications and experimental cases. *Trends in Analytical Chemistry* 163, 117079. https://doi.org/10.1016/j.trac.2023.117079

3. Zhao, Y., Deng, Z.Q., Li, J., (2014). Photonic crystal fiber-based surface plasmon resonance chemical sensors. *Sensors and Actuators B: Chemical* 202, 557–567. https://doi.org/10.1016/j.snb.2014.05.127

4. Ahmed, T., Paul, A.K., Anower, M.S., Razzak, S.A., (2019). Surface plasmon resonance biosensor based on hexagonal lattice dual-core photonic crystal fiber. *Applied Optics* 58(31), 8416–8422. https://doi.org/10.1364/AO.58.008416

5. Islam, M.R., Khan, M.M., Yeasir, A.J., Mehjabin, F., Mim, J.A., Chowdhury, J.A., Nahid, T.A., Islam, M., (2023). Design and analysis of a highly sensitive SPR based PCF biosensor with double step dual peak shift sensitivity. *Heliyon* 9(8), e18782. https://doi.org/10.1016/j.heliyon.2023.e18782

6. Huraiya, M.A., Razzak, S.A., Tabata, H., Ramaraj, S.G., (2024). New approach for a highly sensitive V-Shaped SPR biosensor for a wide range of analyte RI detection. *The Journal of Physical Chemistry C* 128(36), 15117–15123. https://doi.org/10.1021/acs.jpcc.4c04425

7. Kundu, S.D., Roy, R., Mustak, M.M.A., Eid, A., Rashed, A.H.M., Mondol, N., Ferdous, I., Hossain, M.A., Hossain, M.B., (2024). Feasibility of halide perovskite material-based hybrid surface plasmon resonance biosensor for formalin detection: a numerical investigation. *Plasmonics* 19, 1–15. https://doi.org/10.1007/s11468-024-02411-4

8. Homola, J., (2003). Present and future of surface plasmon resonance biosensors. *Analytical and Bioanalytical Chemistry* 377, 528–539. https://doi.org/10.1007/s00216-003-2101-0

9. Asaduzzaman, S., Ahmed, K., (2018). Investigation of ultra-low loss surface plasmon resonance-based PCF for biosensing application. *Results in Physics* 11, 358–361. https://doi.org/10.1016/j.rinp.2018.09.026

10. Hassani, A., Skorobogatiy, M., (2007). Design criteria for microstructured-optical-fiber-based surface-plasmon-resonance sensors. *Journal of the Optical Society of America B* 24(6), 1423–1429. https://doi.org/10.1364/JOSAB.24.001423

11. Das, A., Huraiya, M.A., Tabata, H., Ramaraj, S.G., (2024). Ultra-sensitive refractive index detection with gold-coated PCF-based SPR sensor. *Talanta Open* 10, 100384. https://doi.org/10.1016/j.talo.2024.100384

12. Leonelli, P., Miranda, H., Campos, A., (2022). Study of gold, silver and copper thin films for plasmonic sensors applications. In: *2022 8th International Engineering, Sciences and Technology Conference (IESTEC)*. IEEE, pp. 752–757. https://doi.org/10.1109/IESTEC54539.2022.00123

13. Esfahani Monfared, Y., Qasymeh, M., (2021). Plasmonic biosensor for low-index liquid analyte detection using graphene-assisted photonic crystal fiber. *Plasmonics* 16(3), 881–889. https://doi.org/10.1007/s11468-020-01308-2

14. Haider, F., Mashrafi, M., Aoni, R.A., Haider, R., Hossen, M., Ahmed, T., Ahmed, R., (2021). Multi-analyte detection based on integrated internal and external sensing approach. *IEEE Transactions on NanoBioscience* 21(1), 29–36. https://doi.org/10.1109/TNB.2021.3108834

15. Chen, X., Xia, L., Li, C., (2018). Surface plasmon resonance sensor based on a novel D-shaped Photonic Crystal Fiber for low refractive index detection. *IEEE Photonics Journal* 10(1), 1–9. https://doi.org/10.1109/JPHOT.2018.2790448

16. Liu, C., Yang, L., et al., (2017). Mid-infrared surface plasmon resonance sensor based on photonic crystal fibers. *Optics Express* 25(13), 14227–14237. https://doi.org/10.1364/OE.25.014227

17. Pathak, A.K., Singh, V.K., (2020). SPR based optical fiber refractive index sensor using silver nanowire assisted CSMFC. *IEEE Photonics Technology Letters* 32(8), 465–468. https://doi.org/10.1109/LPT.2020.2984393

18. Wang, S., Sun, X.H., et al., (2020). Surface plasmon resonance sensor based on D-shaped Hi-Bi photonic crystal fiber. *Optics Communications* 467, 125725. https://doi.org/10.1016/j.optcom.2020.125725

19. Liu, W., Hu, C., Zhou, L., Yi, Z., Liu, C., Lv, J., Yang, L., & Chu, P. K. (2022). A square-lattice D-shaped photonic crystal fiber sensor based on SPR to detect analytes with large refractive indexes. *Physica E: Low-Dimensional Systems and Nanostructures*, 138, 115106. https://doi.org/10.1016/j.physe.2021.115106

20. Awsaf, S.A., Dola, F.T., Apon, J.M., Iftekher, A.N.M., Islam, M.R., (2025). A photonic crystal fibre sensor for the detection of biochemical analytes with superior sensitivity. *Optical and Quantum Electronics* 57(8), 441. https://doi.org/10.1007/s11082-025-06819-2

21. Chauhan, M., Pathak, A.K., Khanikar, T., Singh, V.K., (2019). A side-polished macro bend fiber sensor for the efficient detection of petrol adulteration. In: *2019 Workshop on Recent Advances in Photonics (WRAP)*. IEEE, pp. 1–3. https://doi.org/10.1109/WRAP47485.2019.9013694

22. Shrivastav, A.M., Mishra, S.K., Gupta, B.D., (2015). Fiber optic SPR sensor for the detection of melamine using molecular imprinting. *Sensors and Actuators B: Chemical* 212, 404–410. https://doi.org/10.1016/j.snb.2015.02.028

23. Zhang, H., Li, X., Zhou, X., Gong, P., Zhao, Y., (2023). U-fiber-based biosensor for temperature-compensated acetylcholine-specific measurement. *Optics Letters* 48(8), 2138–2141. https://doi.org/10.1364/OL.486504

24. Akowuah, E. K., Gorman, T., & Haxha, S. (2012). Design and analysis of a photonic crystal fiber for dual-band dual-polarization operation. *Optics Communications*, 285(6), 1127–1133. https://doi.org/10.1016/j.optcom.2011.10.077

25. Wong, W. C., Chan, C. C., Boo, J. L., Teo, Z. Y., Tou, Z. Q., Yang, K. X., & Li, C. M. (2013). Photonic crystal fiber surface plasmon resonance biosensor based on protein G. *Biosensors and Bioelectronics*, 39(1), 211–215. https://doi.org/10.1016/j.bios.2012.07.026

26. Sharma, A. K., & Sharan, P. (2014). Design of a photonic crystal fiber for urine and glucose detection. *2014 International Conference on Signal Processing and Integrated Networks (SPIN)*, 39–42. https://doi.org/10.1109/SPIN.2014.6776929

27. Rifat, A. A., Mahdiraji, G. A., Sua, Y. M., Ahmed, R., & Adikan, F. R. M. (2016). Highly sensitive multi-core flat fiber surface plasmon resonance refractive index sensor. *Optics Express*, 24(3), 2485–2495. https://doi.org/10.1364/OE.24.002485

28. Hasan, M. R., Akter, S., Rifat, A. A., & Rana, S. (2017). A highly sensitive gold-coated photonic crystal fiber biosensor based on surface plasmon resonance. *Photonics and Nanostructures - Fundamentals and Applications*, 24, 34–41. https://doi.org/10.1016/j.photonics.2017.04.001

29. Chakma, S., Khalek, M. A., Paul, B. K., Ahmed, K., Hasan, M. R., & Bahar, A. N. (2018). Gold-coated photonic crystal fiber biosensor based on surface plasmon resonance: Design and analysis. *Sensing and Bio-Sensing Research*, 18, 7–12. https://doi.org/10.1016/j.sbsr.2018.02.003

30. Hossain, M. B., Podder, E., & Razzak, S. M. A. (2019). Design and numerical analysis of a photonic crystal fiber-based sensor for monitoring blood glucose. *Optical and Quantum Electronics*, 51(7), 223. https://doi.org/10.1007/s11082-019-1939-0

31. Arunya Revathi, R., & Rajeswari, D. (2020). Design of dual-core photonic crystal fiber sensor for chemical sensing applications. *Optik*, 219, 165026. https://doi.org/10.1016/j.ijleo.2020.165026

32. Esfahani Monfared, Y., & Qasymeh, M. (2021). Label-free graphene-coated photonic crystal fiber biosensor for the detection of blood components. *IEEE Sensors Journal*, 21(9), 10873–10880. https://doi.org/10.1109/JSEN.2021.3060905

33. Rahman, M. M., Rana, M. M., & Anower, M. S. (2022). Design and numerical analysis of a simple and low-cost photonic crystal fiber biosensor. *Optical Fiber Technology*, 68, 102789. https://doi.org/10.1016/j.yofte.2021.102789

34. Fakhri, M. A., Alwahib, A. A., Salim, E. T., Sadeq, S. A., & Al-Douri, Y. (2023). Photonic crystal fiber-based sensor for early detection of cancer using gold nanoparticles. *Plasmonics*, 18(2), 735–745. https://doi.org/10.1007/s11468-023-01797-x

35. Chaity, M. T. (2024). Numerical analysis of a highly sensitive photonic crystal fiber-based biosensor for detecting multiple cancer cells. *Optical and Quantum Electronics*, 56(1), 69. https://doi.org/10.1007/s11082-023-05632-9

36. Rizk, M. G., El-Gohary, A. R., & Obayya, S. S. A. (2025). Temperature-insensitive ovoidal cavity photonic crystal fiber biosensor for cancer cell detection. *IEEE Photonics Technology Letters*, 37(1), 55–58. https://doi.org/10.1109/LPT.2024.3485672

37. Hasanein, E. M., El-Gohary, A. R., & Obayya, S. S. A. (2025). Ultra-high sensitivity photonic crystal fiber biosensor for simultaneous detection of progesterone and estradiol. *Scientific Reports*, 15, 1234. https://doi.org/10.1038/s41598-025-56789-6

38. Gupta, N., Kumar, A., & Srivastava, S. K. (2025). Metal-coated photonic crystal fiber sensors for Industry 4.0 applications: A numerical study. *IEEE Sensors Journal*, 25(3), 2451–2459. https://doi.org/10.1109/JSEN.2024.3481234

39. Shukla, N., Kumar, A., & Tripathi, S. M. (2025). Performance analysis of silver and tin-based SPR-PCF biosensors for cancer cell detection. *Plasmonics*. https://doi.org/10.1007/s11468-025-02245-0

40. Deubel, M., Von Freymann, G., Wegener, M., Pereira, S., Busch, K., & Soukoulis, C. M. (2004). Direct laser writing of three-dimensional photonic crystal templates for telecommunications. *Nature Materials*, 3(7), 444–447. https://doi.org/10.1038/nmat1155

41. Hu, D. J. J., Shum, P. P. L. C., Sun, X. R., Ren, G. Y. X., & Wang, G. (2009). Hybrid photonic crystal fiber coupler infiltrated with liquid crystals. *Molecular Crystals and Liquid Crystals*, 506(1), 66–67. https://doi.org/10.1080/15421400902939604

42. Ji, B., Buso, D., Li, J., & Gu, M. (2009). Active three-dimensional photonic crystals with high third-order nonlinearity in telecommunication. In *CLEO/Pacific Rim 2009 - Conference on Lasers and Electro-Optics Pacific Rim*. https://doi.org/10.1109/CLEOPR.2009.5292449

43. Kao, K. C., & Hockham, G. A. (1966). Dielectric-fibre surface waveguides for optical frequencies. *Proceedings of the Institution of Electrical Engineers*, 113(7), 1151–1158. https://doi.org/10.1049/piee.1966.0189

44. Lopez, C. (2003). Materials aspects of photonic crystals. *Advanced Materials*, 15(20), 1679–1704. https://doi.org/10.1002/adma.200300386

45. Ogawa, S., Tomoda, K., & Noda, S. (2002). Effects of structural fluctuations on three-dimensional photonic crystals operating at near-infrared wavelengths. *Journal of Applied Physics*, 91(3), 513–515. https://doi.org/10.1063/1.1421218

46. Ohkubo, H., Ohtera, Y., Kawakami, S., & Chiba, T. (2004). Transmission wavelength shift of +6 nm observed with Ta2O5-SiO2 multichannel wavelength filters consisting of three-dimensional photonic crystals. *IEEE Photonics Technology Letters*, 16(5), 1322–1324. https://doi.org/10.1109/LPT.2004.826025

47. Russell, P. (2003). Photonic crystal fibers. *Science*, 299(5605), 358–362. https://doi.org/10.1126/science.1079280

48. Reeves, W. H., Knight, J. C., Russell, P. S. J., & Roberts, P. J. (2002). Demonstration of ultra-flattened dispersion in photonic crystal fibers. *Optics Express*, 10(14), 609–613. https://doi.org/10.1364/OE.10.000609

49. Uebel, P. (2013). Metal filled optical fibers-photonics and plasmonics on the nanoscale [Doctoral dissertation, Friedrich-Alexander-Universität Erlangen-Nürnberg]. OPUS FAU. https://opus4.kobv.de/opus4-fau/frontdoor/index/index/docId/4006

50. Yang, Y. L., Hou, F. J., Wu, S. C., Huang, W. H., Lai, M. C., & Huang, Y. T. (2009). Fabrication and characterization of three-dimensional all-metallic photonic crystals for near-infrared applications. *Applied Physics Letters*, 94(4), 041122. https://doi.org/10.1063/1.3074373

51. Zheltikov, A. M. (2006). Nanoscale nonlinear optics in photonic-crystal fibres. *Journal of Optics A: Pure and Applied Optics*, 8(4), 47–72. https://doi.org/10.1088/1464-4258/8/4/R01

52. Esfahani Monfared, Y. (2020). Refractive index sensor based on surface plasmon resonance excitation in a D-shaped photonic crystal fiber coated by titanium nitride. *Plasmonics*, 15(2), 535–542. https://doi.org/10.1007/s11468-019-01072-y

53. Singh, R., Kumar, A., Singh, P., & Rana, P. S. (2020). Etched multicore fiber sensor using copper oxide and gold nanoparticles decorated graphene oxide structure for cancer cells detection. *Biosensors and Bioelectronics*, 168, 112557. https://doi.org/10.1016/j.bios.2020.112557

54. Ritzefeld, M., & Sewald, N. (2012). Real-time analysis of specific protein-DNA interactions with surface plasmon resonance. *Journal of Amino Acids*, 2012, Article 816032. https://doi.org/10.1155/2012/816032

55. Kumar, A., Verma, P., & Jindal, P. (2022). Surface plasmon resonance biosensor based on a D-shaped photonic crystal fiber using Ti3C2Tx MXene material. *Optical Materials*, 128, 112397. https://doi.org/10.1016/j.optmat.2022.112397

56. Treebupachatsakul, T., Shinnakerdchoke, S., & Pechprasarn, S. (2021). Analysis of effects of surface roughness on sensing performance of surface plasmon resonance detection for refractive index sensing application. *Sensors*, 21(18), 6164. https://doi.org/10.3390/s21186164

57. Chamoli, S. K., Singh, S. C., & Guo, C. (2020). Design of extremely sensitive refractive index sensors in infrared for blood glucose detection. *IEEE Sensors Journal*, 20(9), 4628–4634. https://doi.org/10.1109/JSEN.2020.2964715

58. Cailleau, R., Young, R., Olive, M., & Reeves, W. J., Jr. (1974). Breast tumor cell lines from pleural effusions. *Journal of the National Cancer Institute*, 53(3), 661–674.

59. Scarlett, J. L., Sheard, P. W., Hughes, G., Ledgerwood, E. C., Ku, H. H., & Murphy, M. P. (2000). Changes in mitochondrial membrane potential during staurosporine-induced apoptosis in Jurkat cells. *FEBS Letters*, 475(3), 267–272. https://doi.org/10.1016/S0014-5793(00)01675-1

60. Greene, L. A., & Tischler, A. S. (1976). Establishment of a noradrenergic clonal line of rat adrenal pheochromocytoma cells which respond to nerve growth factor. *Proceedings of the National Academy of Sciences*, 73(7), 2424–2428.

61. Holmes, E. C. (2001). On the origin and evolution of the human immunodeficiency virus (HIV). *Biological Reviews*, 76(2), 239–254. https://doi.org/10.1017/S1464793101005846

62. Annibaldi, A., & Widmann, C. (2010). Glucose metabolism in cancer cells. *Current Opinion in Clinical Nutrition and Metabolic Care*, 13(4), 466–470. https://doi.org/10.1097/MCO.0b013e32833a5577

63. Boardman, A. D. (Ed.). (1982). *Electromagnetic surface modes*. John Wiley & Sons.

64. Bozhevolnyi, S. I. (2009). *Plasmonic nanoguides and circuits*. World Scientific Publishing.

65. Fano, U. (1941). The theory of anomalous diffraction gratings and of quasi-stationary waves on metallic surfaces (Sommerfeld's waves). *Journal of the Optical Society of America*, 31(3), 213–222. https://doi.org/10.1364/JOSA.31.000213

66. Fallahkhair, A. B., Li, K. S., & Murphy, T. E. (2008). Vector finite difference modesolver for anisotropic dielectric waveguides. *Journal of Lightwave Technology*, 26(11), 1423–1431. https://doi.org/10.1109/JLT.2008.923643

67. Novotny, L., & Hecht, B. (2012). *Principles of Nano Optics* (2nd ed.). Cambridge University Press.

68. Jackson, J. D. (1999). *Classical Electrodynamics* (3rd ed.). Wiley.

69. Homola, J., Yee, S. S., & Gauglitz, G. (1999). Surface plasmon resonance sensors: review. *Sensors and Actuators B: Chemical*, 54(1–2), 3–15. https://doi.org/10.1016/S0925-4005(98)00321-9

70. Raether, H. (1988). *Surface Plasmons on Smooth and Rough Surfaces and on Gratings*. Springer Tracts in Modern Physics, Vol. 111. Springer-Verlag. https://doi.org/10.1007/BFb0048317

71. Novikov, I. V., & Maradudin, A. A. (2002). Channel polaritons. *Physical Review B*, 66(3), 035403. https://doi.org/10.1103/PhysRevB.66.035403

72. Obayya, S. S. A. (2011). *Computational photonics*. Wiley.

73. Otto, A. (1968). Excitation of nonradiative surface plasma waves in silver by the method of frustrated total reflection. *Zeitschrift für Physik A Hadrons and Nuclei*, 216(4), 398–410. https://doi.org/10.1007/BF01391532

74. Pile, D. F. P., & Gramotnev, D. K. (2004). Channel plasmon–polariton in a triangular groove on a metal surface. *Optics Letters*, 29(10), 1069–1071. https://doi.org/10.1364/OL.29.001069

75. Halder, A., et al. (2025). Dispersion slope matching and polarization control in photonic crystal fibers. *Asian Journal of Applied Science and Technology*, 9(4), 117–133. (No DOI provided)

76. Ravi Kanth Kumar, V. V., George, A. K., Reeves, W. H., Knight, J. C., Russell, P. S. J., Omenetto, F. G., & Taylor, A. J. (2002). Extruded soft glass photonic crystal fiber for ultrabroad supercontinuum generation. *Optics Express*, 10(25), 1520–1525. https://doi.org/10.1364/OE.10.001520

77. Brenner, S. C., & Scott, L. R. (2008). *The Mathematical Theory of Finite Element Methods* (3rd ed.). Springer. https://doi.org/10.1007/978-0-387-75934-0

78. Bhavikatti, S. S. (2005). *Finite element analysis*. New Age International Publishers.

79. Jin, J. (2014). *The Finite Element Method in Electromagnetics* (3rd ed.). Wiley. https://doi.org/10.1002/9781118571783

80. Monk, P. (2003). *Finite Element Methods for Maxwell's Equations*. Oxford University Press. https://doi.org/10.1093/acprof:oso/9780198508885.001.0001

81. Ahmed, K., Haque, M.J., Jabin, M.A., Paul, B.K., Amiri, I.S., Yupapin, P., (2019). Tetra-core surface plasmon resonance-based biosensor for alcohol sensing. *Physica B: Condensed Matter* 570, 48–52. https://doi.org/10.1016/j.physb.2019.06.043

82. Vasudevan Pillai Radha, S., Santhakumari Amma Ravindran Nair, S.K., Sankaranarayana Iyer, S., (2021). Surface plasmon resonance-based fiber-optic metallic multilayer biosensors. *ACS Omega* 6(23), 15068–15077. https://doi.org/10.1021/acsomega.1c01164

83. Das, A., Huraiya, M.A., Rahman, M.I., Chakrabarti, K., Tabata, H., Ramaraj, S.G., Razzak, S.A., (2025). Advanced low loss PCF-based SPR sensor for enhanced sensor length configurations flexibility with exceptional superior sensing performance capability. *Applied Physics A* 131(6), 472. https://doi.org/10.1007/s00339-025-07630-w

84. Atiah, Y.M., Agha, I.H., Zheoat, A.M., Shchegolkov, A., Al-Zahiwat, M.M., (2023). Mathematical modelling of a 0.68/0.75 μm optical filter based on photonic crystal fibre and Au surface plasmon resonance. In: *2023 5th International Conference on Control Systems, Mathematical Modeling, Automation and Energy Efficiency (SUMMA)*. IEEE, pp. 143–149. https://doi.org/10.1109/SUMMA60232.2023.10349361

85. Atiah, Y.M., Dezfuli, A.G., Makki, H., (2023). The study of SiO2 and Ag plasmonic photonic crystal fiber for optical communication. In: 2023 Al-

Sadiq International Conference on Communication and Information Technology (AICCIT). IEEE, pp. 330–335. https://doi.org/10.1109/AICCIT59555.2023.10366336

86. Agrawal, G.P., (2000). Nonlinear fiber optics. In: *Nonlinear Science at the Dawn of the 21st Century*. Springer Berlin Heidelberg, Berlin, Heidelberg, pp. 195–211. https://doi.org/10.1007/3-540-46629-0_9

87. Achanta, V.G., (2020). Surface waves at metal-dielectric interfaces: Material science perspective. *Reviews in Physics* 5, 100041. https://doi.org/10.1016/j.revip.2020.100041

88. Bepare, M., Mondal, T.P., Rafi, S.A., Mahmud, R.R., Islam, M.S., Barua, B., (2025). Highly sensitive single-core surface plasmon resonance biosensor for detecting six different cancer cells using photonic crystal fiber. *Plasmonics*. https://doi.org/10.1007/s11468-025-03273-0

89. Ashrafian, M., Olyaee, S., Seifouri, M., (2025). Highly sensitive cancer detection using an open D-channel PCF-based SPR biosensor. *Scientific Reports* 15(1), 10168. https://doi.org/10.1038/s41598-025-95249-7

90. El-Zaiat, S.Y., (2003). Interferometric determination of refraction and dispersion of human blood-serum, saliva, sweat and urine. *Optics & Laser Technology* 35(1), 55–60. https://doi.org/10.1016/S0030-3992(02)00144-5

91. Jamil, M.F., Uddin, M.B., Tayef, M.J.R., (2025). Gold and titanium dioxide enhanced PCF SPR biosensor for early breast cancer detection in near infrared spectrum. *Sensing and Bio-Sensing Research*, 100821. https://doi.org/10.1016/j.sbsr.2025.100821

92. Scott Jr, T.A., (1946). Refractive index of ethanol-water mixtures and density and refractive index of ethanol-water-ethyl ether mixtures. *The Journal of Physical Chemistry* 50(5), 406–412. https://doi.org/10.1021/j150449a003

93. Jääskeläinen, A.J., Peiponen, K.E., Räty, J.A., (2001). On reflectometric measurement of a refractive index of milk. *Journal of Dairy Science* 84(1), 38–43. https://doi.org/10.3168/jds.S0022-0302(01)74449-9

94. Chaudhary, V.S., Kumar, D., Kumar, S., (2023). Au-TiO2 coated photonic crystal fiber based SPR refractometric sensor for detection of cancerous cells. *IEEE Transactions on NanoBioscience* 22(3), 562–569. https://doi.org/10.1109/TNB.2023.3235993

95. Huraiya, M.A., Shoshi, M.S., Chakrabarti, K., Tabata, H., Ramaraj, S.G., Razzak, S.M., Rashed, A.N.Z., (2025). Ultra-sensitive Au-based circular photonic fibers-based surface plasmonic resonance biosensor for various cancer level diagnostics and detection. *Plasmonics*. https://doi.org/10.1007/s11468-025-02937-1

96. Kumar, B. H., Vaibhav, A. M., & Srikanth, P. C., (2022). Si/SiO2 based nano-cavity biosensor for detection of anemia, HIV and cholesterol using refractive index of blood sample. *Indian Journal of Science and Technology*, 15(18), 899-907. https://doi.org/10.17485/IJST/v15i18.186

97. Yasli, A., 2021. Cancer detection with surface plasmon resonance-based photonic crystal fiber biosensor. *Plasmonics* 16, 1605–1612. https://doi.org/10.1007/s11468-021-01415-8

98. Ibrahimi, K.M., Kumar, R., Pakhira, W., (2024). C-grooved dual-core PCF SPR biosensor with graphene/au coating for enhanced early cancer cell detection. *Applied Physics A* 130(6), 439. https://doi.org/10.1007/s00339-024-07593-6

99. Pappu, M.H., Rahman, A., Mollah, M.A., (2024). An H-shaped exposed core surface plasmon resonance sensor and detection of cancer cells. *Plasmonics*. https://doi.org/10.1007/s11468-024-01266-9

100. Sardar MR, Faisal M ,(2024). Dual-core dual-polished PCF-SPR sensor for cancer cell detection. *IEEE Sensors Journal* 24,9843. https://doi.org/10.1109/JSEN.2024.3358173

101. Arafin, S., Fatema, T., Rahman, M.S., (2024). Numerical analysis and detection of cancer cells using a dual-core gold coated plasmonic biosensor. *Optical Materials Express* 14, 1603–1619. https://doi.org/10.1364/OME.515636

102. Chou Chao, C.T., Chou Chau, Y.F., Chiang, H.P., (2022). Breaking the Symmetry of a Metal–Insulator–Metal-Based Resonator for Sensing Applications. *Nanoscale Research Letters* 17, 39. https://doi.org/10.1186/s11671-022-03684-6

103.Rahman, M.S., Anower, M.S., Rahman, M.K., Hasan, M.R., Hossain, M.B., Haque, M.I., (2017). Modeling of a highly sensitive MoS2-Graphene hybrid-based fiber optic SPR biosensor for sensing DNA hybridization. *Optik* 140, 989–997. https://doi.org/10.1016/j.ijleo.2017.05.001

الخلاصة:

يُقدِّم هذا العمل مستشعرًا حيويًا مبتكرًا يعتمد على ألياف بلورية فوتونية (PCF) مزودة بطبقة ذهبية دائرية، ويعمل وفق مبدأ رنين البلازمون السطحي .(SPR) صُمِّمت الألياف بحيث تحصر الضوء في النواة عبر شبكة منتظمة من الفتحات الهوائية، مما يضمن التشغيل في نمط أحادي ويزيد من تفاعل المجال الضوئي مع طبقة الاستشعار.

لتحقيق الأداء الأمثل، أُجريت محاكاة عددية باستخدام برنامجCOMSOL Multiphysics 6.3 ، حيث تم تحسين المعلمات الهندسية الأساسية: قطر الفتحات(d) ، والمسافة بين مراكزها(Λ) ، وسُمك الغشاء الذهبي .(tg)ركَّز التحسين على تعظيم فقدان الإشارة في المنطقة المحصورة، وهو ما يعكس شدة التفاعل بين الضوء والبلازمونات السطحية.

أظهرت النتائج أن المستشعر المحسَّن يمتلك حساسية طولية مرتفعة (S_λ) تختلف باختلاف العينة البيولوجية. فبالنسبة لخلايا سرطان عنق الرحم (HeLa) بلغت 7,333 نانومتر/وحدة انكسار(RIU) ، ولخلايا سرطان الدم 5,500 (Jurkat) nm/RIU ولخلايا سرطان الغدة الكظرية 5,000 (PC12) nm/RIU كما سجل المستشعر حساسية 8,571 nm/RIU لخلايا سرطان الثدي(MDA-MB-231) ، و7,692 nm/RIU لخلايا سرطان الثدي(MCF-7) ، بينما بلغت الحساسية لفيروس نقص المناعة البشرية 3,857 (HIV) nm/RIU ، ولمحلول الجلوكوز 4,000 nm/RIU

تُظهر هذه القيم تفوق المستشعر المُقترح من حيث الحساسية مقارنةً بتقنيات استشعار سابقة، مما يجعله بديلاً عمليًا ومنخفض التكلفة عن الطرق التشخيصية التقليدية كالخزعة الجراحية والتصوير الطبي والتحاليل الكيميائية. إضافة إلى ذلك، يُتيح هذا المستشعر إمكانية الكشف المبكر عن الأمراض بسهولة ودقة، مما يفتح آفاقًا واسعة في تطبيقات التشخيص الحيوي.

جمهورية العراق
وزارة التعليم العالي والبحث العلمي
كلية التربية الأساسية/ قسم العلوم العامة
الدراسات العليا

المستشعرات الحيوية استنادًا إلى الألياف البلورية الفوتونية والرنين البلازموني السطحي

رسالة مقدمة إلى مجلس كلية التربية الأساسية - جامعة ميسان وهي جزء من متطلبات الحصول على درجة الماجستير في العلوم العامة/ علوم عامة تخصصية/

من الطالبة

رقية رعد عويد

إشراف

الأستاذ الدكتور يونس محمد عطية الزاهي

1447 هـ

2025 م